Nishan Jain
Department of Aerospace Engineering,
University of Maryland,
College Park, MD 20742
e-mail: nishan@umd.edu

Alexandra Le Moine
Department of Aerospace Engineering,
University of Maryland,
College Park, MD 20742
email: alemoine@terpmail.umd.edu

Geoffroy Chaussonnet
Institute of Thermal Turbomachinery,
Karlsruhe Institute of Technology,
Karlsruhe 76131, Germany
e-mail: geoffroy.chaussonnet@kit.edu

Alison Flatau
Department of Aerospace Engineering,
University of Maryland,
College Park, MD 20742
e-mail: aflatau@umd.edu

Luis Bravo
Vehicle Technology Directorate,
U.S. Army Research Laboratory,
Aberdeen Proving Ground, MD 21005
e-mail: luis.g.bravorobles.civ@mail.mil

Anindya Ghoshal
Vehicle Technology Directorate,
U.S. Army Research Laboratory,
Aberdeen Proving Ground, MD 21005
e-mail: anindya.ghoshal.civ@mail.mil

Michael J. Walock
Vehicle Technology Directorate,
U.S. Army Research Laboratory,
Aberdeen Proving Ground, MD 21005
e-mail: michael.j.walock.civ@mail.mil

Muthuvel Murugan
Vehicle Technology Directorate,
U.S. Army Research Laboratory,
Aberdeen Proving Ground, MD 21005
e-mail: muthuvel.murugan.civ@mail.mil

Prashant Khare
Department of Aerospace Engineering,
University of Cincinnati,
Cincinnati, OH 45221-0070
e-mail: Prashant.Khare@uc.edu

A Critical Review of Physical Models in High Temperature Multiphase Fluid Dynamics: Turbulent Transport and Particle-Wall Interactions

This review article examines the last decade of studies investigating solid, molten, and liquid particle interactions with one another and with walls in heterogeneous multiphase flows. Such flows are experienced in state-of-the-art and future-concept gas turbine engines, where particles from the environment, including volcanic ash, runway debris, dust clouds, and sand, are transported by a fluid carrier phase and undergo high-speed collisions with high-temperature engine components. Sand or volcanic ash ingestion in gas turbine engines is known to lead to power-loss and/or complete engine failure. The particle-wall interactions that occur in high-temperature sections of an engine involve physics and intrinsic conditions that are sufficiently complex that they result in highly disparate and transient outcomes. These particles, which often times are made up of glassy constituents called calcium–magnesium–alumino–silicate (CMAS), are susceptible to phase change at combustor temperatures (1650°), and can deposit on surfaces, undergo elastic and plastic deformation, rebound, and undergo breakup. Considerable research has been put into developing empirical and physics-based models and numerical strategies to address phase interactions. This article provides a detailed account of the conceptual foundation of physics-based models employed to understand the behavior of particle-wall interaction, the evolution of numerical methods utilized for modeling these interactions, and challenges associated with improving models of particle-particle and particle-wall interactions needed to better characterize multiphase flows. It also includes description of a testbed for acquiring canonical data for model validation studies.
[DOI: 10.1115/1.4051503]

1 Introduction

The objective of this review is to examine the last decade of studies investigating solid, molten, and liquid particle-wall interactions in systems with heterogeneous multiphase flows. Such flows are experienced in state-of-the-art and future concept gas turbine engines, where particles from the environment, such as volcanic ash, runway debris, dust clouds, and sand, are transported by a fluid carrier phase and undergo high-speed collisions with high-temperature engine components. Sand or volcanic ash ingestion in gas turbine engines is known to lead to power loss or complete engine failure. Guffanti et al. [1] report on over 79 incidents in which aircraft encounters with volcanic ash clouds led to severe engine damage. Similarly, there have been a number of rotorcraft incidents, including the fatal V-22 Osprey crash landing in May 2015 [2], due to engine failure attributed to excessive buildup on turbine blades that lead to degradation and spallation of materials from ingested sand/dust particles.

Manuscript received September 11, 2020; final manuscript received June 16, 2021; published online July 28, 2021. Assoc. Editor: Arezoo Ardekani.

This problem arises as particles having nominal dimensions of less than $\sim 30\ \mu$m are too small to be blocked by the inlet particle separation system, and are ingested into the engine. An inlet particle separation system is designed to impart swirl to the entering airflow and extract that part of the flow containing the centrifuged sand through a scavenge system. However, continued use has led to engine performance penalties and thus its use is generally reserved for the most severe conditions [3]. Of particular concern are ingested particles made of glassy constituents, the most common of which are calcium–magnesium–alumino–silicates (CMAS) particles. CMAS particles are susceptible to phase change at combustor temperatures [3], and can deposit on surfaces, undergo elastic and plastic deformation, rebound, and even undergo breakup with slip/shear along the surface with possible thermal and momentum dissipation. These particle-interaction processes are transient and occur over a wide range of spatio-temporal scales, thereby increasing its modeling complexity.

An enduring challenge for the aviation community is dealing with particulate matter of less than 2.5 μm in numerous regions across the globe (see Fig. 1), including desert and urban environments. Moreover, geographically dependent CMAS composition leads to variations in shape, chemistry, and melting temperate which in turn may lead to increased damage. Figure 1 shows high-intensity regions of particulate matter less than 2.5 μm in diameter (PM2.5) extending across North Africa, South West Asia, and South East Asia [4,5].

Molten CMAS can deposit on and react with the protective thermal/environmental barrier coatings (T/EBC) on the combustor liner, turbine shroud, blades, and nozzle guide vanes [6,7]. Particles that get into the bleed air intake and cooling passage can build up on surfaces in the unreacted form, where due to the combination of high-pressure flow and high-temperature wall surfaces, particles sinter, forming solid masses that clog cooling holes as shown in Fig. 4(*c*). This damage is further compounded if the subsequent blockage of cooling channels in the hot section results, which reduces bleed air mass flow while further increasing bulk material temperatures [8].

In order to avoid material damage, engine designs incorporate T/EBCs along with bleed air film cooling of super-alloy or ceramic matrix composite components [8,9]. T/EBC coatings prevent oxidation damage caused by moisture in the combusting atmosphere that is known to rapidly degrade the underlying SiC–SiC ceramic matrix composite substrate material [10]. Although T/EBCs are available that are effective to temperatures of up to roughly 1300 °C, these strategies do not yet provide robust protection against increased CMAS attack of advanced-engine hot-section components that are exposed to air flows with temperatures of 1650 °C or higher; components that, as a result, still undergo severe degradation.

To develop superior T/EBC systems that are resistant to CMAS attack at higher temperatures (>1650 °C), an integrated computational and experimental approach that provides validated models and insights into the fluid-structure interaction physics is essential. These multiphysics processes occur over a wide range of spatio-temporal scales, thereby requiring a well-defined canonical approach to provide the basis for the understanding of practical problems.

Predicting and characterizing particle-wall interaction behavior and determining its transient properties is very challenging but also important for a variety of engineering applications. A considerable amount of research has been conducted on developing empirical and physics-based models and numerical strategies to address phase interactions. This article provides a detailed account of the conceptual foundation of physics-based models employed to understand the behavior of particle-wall interaction and the evolution of state-of-the-art numerical methods utilized for modeling these interactions. This review article also addresses challenges associated with advancing the state of the art in modeling particle-wall interactions to characterize flows with entrained CMAS particles at temperatures that cause CMAS particles to become molten.

This review is structured as follows. The multiscale nature of particle-laden turbulent flows in gas turbine engines and the corresponding characteristic nondimensional groups are described in Sec. 2. Section 3 reviews the physics of particle-laden flows with a focus on numerical simulation. The outcomes of liquid droplet impact on a solid substrate and modeling strategies are discussed in Sec. 4. The modeling of particle deposition, the mechanical properties of the particle, deposition models, and available experiments for the specific case of gas turbine operating conditions are reviewed in Sec. 5. Future directions for advancing this field are presented in Sec. 6.

2 Multiscale Nature of Particle-Laden Multiphase Flow

Particle-laden heterogeneous multiphase flows are commonly observed in nature and play a vital role in basic research as well as in a broad range of engineering applications. Notable examples include dispersion of dust in the atmosphere, production of oil and gas, additive manufacturing, and the design of chemically powered devices. Suspended particles can exist in multiple states (solid/liquid/gaseous), or a complex heterophase state, and evolve in a high shear rate carrier environment exhibiting highly nonlinear behavior. Despite the significant increase in the body of research related to this topic, the understanding of the underlying physics remains incomplete and poses one of the grand challenges in multiphase flows. This is partly due to the lack of fully resolved measurements, at the scale of the dispersed phase, as well as to the inherent physical complexity of the multiphase flow. For instance, the multiphase flow within turbomachinery can contain up to billions of particles that are transported and dispersed by the highly energetic carrier phase turbulent flow field. One of the most important features in multiphase flows is the presence of a very wide spectrum of length scales and timescales, from those associated with the smallest Kolmogorov scale turbulent eddies and particle-scale motions to those of a wide range of larger turbulent flow coherent structures. Depending on the governing flow parameters, such as particle-to-fluid length-scale, time-scale ratios, and particle Reynolds number, emerging nonlocal dynamics such as self-induced vortex shedding may introduce turbulence modulation effects that can dramatically impact the character of the flow [11]. The evolution of the dispersed flow in a confined environment will naturally lead to particulate impingement and deposition which is in turn governed by many physical processes, including thermophoresis, thermal diffusion, and electrostatic charges, among others discussed in Ref. [12].

2.1 Particle-Laden Environment Within Gas Turbine Engines.

Gas-turbine engine-powered aircraft often operate in harsh environments where significant quantities of reactive sand and dust particles are present. These particles are easily ingested into the gas turbine engine during landing, takeoff, and other near-ground operations. Because of the strong ground vortex created by the engine, ingested matter can have broad size composition ranging from few microns to hundreds of microns [13]. Apart from the size, the properties of the ingested particles will also vary depending on the geographical location. Zhang et al. [14] provide a detailed description of the elemental properties of different types of sands ingested by the engine for varying geographic locations [15].

Particle ingestion can have serious effects on overall engine performance and servicing intervals. To quantify the effects of degradation and identify critical locations, it is important to understand the transport of particle-laden flow and its properties within the engine. Figure 2 shows a typical gas turbine engine and along with the key stages of operation. To minimize the damage early on, inertial particle separators are employed before the compressor stage to filter out the ingested matter. Since the separators use particle inertia to capture them, their efficacy varies with the size

of the particle. Inertial separators work well for particles greater than a certain size. Over the years, the particle separators have become increasingly efficient and this threshold of particle size being filtered effectively has changed considerably. As such, a noticeable variation in the reported threshold size is found in the literature. For example, Murugan et al. [16] stated that the separators can adequately separate particles of size above 75 μm. Dunn et al. [17] investigated volcanic ash ingestion and they found out that the particles with an average size of 38 μm were available at the early stages of the compressor. Bojdo et al. [3] reported that particles below the size of 10 μm mostly escape inertial separators. The significant variance in the reported threshold particle size is also attributed to the manufacturers having their specific metrics for determining the mean particle size. For the sake of consistency in the analysis presented in this review article, we have selected the average threshold size to be 30 μm, above which particles are captured by the inertial separator with high efficiency. While the mean size of the particles reaching the compressor stage decreases substantially due to the presence of separators, the damage from the particles to the engine remains imminent. For each engine stage, the consequent behavior of the particles and their interaction is investigated methodically by Bojdo et al. [3] through the development of reduced-order modeling.

Within the compressor stage, the trajectory of large particles is unaffected by the swirling turbulent flow owing to their high inertia. These particles impact directly on the component surfaces causing blade erosion and damage [18]. These impacts also cause a breakdown of the particles, altering the distribution of particle size. Particles larger than 10 μm are pulverized into many smaller particles. Their breakdown makes later stages of the compressor less susceptible to erosive damage. A fraction of the mass flow along with its dispersed particles is extracted at the later stages to serve as cooling flow at the turbine stage. Therefore in addition to fewer particles reaching the combustor stage, the average particle size is predominantly less than 10 μm.

Because of high operating temperatures within the combustor, the smaller particles are likely to undergo partial to complete meltdown. As these particles soften, they exhibit strong adhesion. However, they do not readily deposit on combustor walls as most particles are propelled to the later stages of the engine by the energetic turbulent flow driven by the high-pressure turbines. Only a limited subset of particles are small enough to melt but are large enough, i.e., have sufficient inertia, to not be transported by the flow. It is these particles that will be deposited, likely in the form of glazing, on combustor walls.

The particles reaching the turbine stage are substantially smaller in size compared to the primary ingested mixture but have a strong tendency to react chemically due to their melted and energetic state. The particles will follow the flow initially due to their low inertia but will tend to deposit on turbine surfaces as they encounter sudden changes in flow through the early stages of the turbine.

The core flow mixed with ingested particles goes through the compressor and is heated in the combustor as the fuel mixture is burned. The resulting hot gas mixture is then directed to the turbine stages and finally exits the exhaust nozzle. The thermal efficiency and the thrust output of the engine increase directly with increase in the flow temperature at the inlet to the turbine. This results in a critical design constraint for modern gas-turbine engines arising due to the need to avoid inlet flow temperatures exceeding the material limits of the components used in the turbine. As such, considerable research efforts have been put into the development of super alloys and thermal barrier coatings that can withstand high temperatures. Active cooling technologies that employ air bled from the compressor are also continuously being refined [19]. Figure 3 provides a historical trend of allowable flow temperature based on the materials available at the time. By considering the advancement in promising material and cooling technologies, the figure also predicts the future trend of the increase in allowable turbine inlet temperature [20].

The three main elements of a gas turbine engine, namely, the compressor, combustor, and turbine, experience different forms of damage due to ingested particles. The primary mechanism of damage in the compressor (cold) section of the engine is erosion. Ingested particles directly erode compressor vane and blade surfaces, causing a reduction in their aerodynamic performance [21,22]. In the combustor, the particles are heated significantly and, depending on their composition, they may become molten. Within the combustor section, the particulates could potentially block the fuel injection nozzles causing inefficient combustion and performance degradation. This heated semimolten particle-laden hot gas mixture then enters the turbine section where, due to the high temperature and high velocities, the primary mechanism of damage is particle deposition. This causes CMAS buildup and infiltration along the surfaces of thermal barrier coatings (TBC) columnar gaps and open vertical cracks in the TBC. Particles are deposited on the turbine blades thereby altering blade aerodynamic profiles and reducing the turbine efficiency. This deposition can occur as a thin film over the hot surfaces of the gas turbine, known as glazing, and can build up over time. An example of this

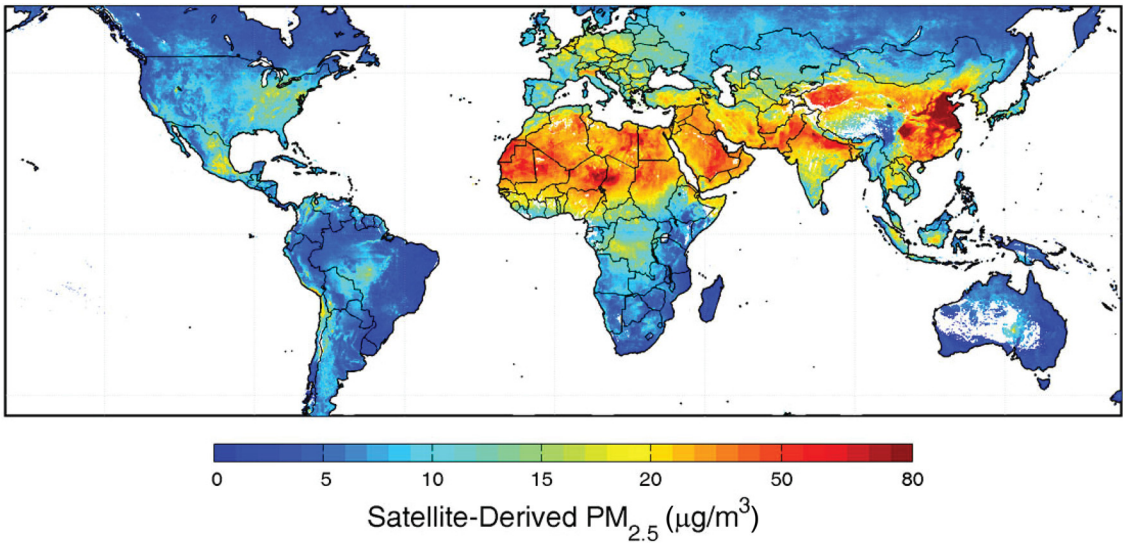

Fig. 1 Global satellite-derived PM2.5 averaged over 2008–2016 showing local intensity of particulate matter less than 2.5 μm. White space indicates water or locations containing <50 measurements. Image [copyright] Aaron van Donkelaar. Reproduced with permission from the author [4].

damage mechanism is shown in Fig. 4(*b*). Deposition of particles in the turbine restricts the flow area and increases surface roughness, both of which lead to the decreased aerodynamic performance of the turbine and result in loss of engine power [23].

The majority of reactive deposition under high temperatures is chemically comprised of CMAS [24]. The thermal barrier coating over turbine blade surfaces is very susceptible to damage from CMAS. At high temperatures, CMAS deposits melt, and then infiltrate and degrade the TBC layer through a direct chemical reaction with TBC constituents [25]. This process continues with each repeated thermal gradient cycle. Studies [26,27] have shown that these chemical interactions can lead to spallation of TBC followed by accelerated oxidation and corrosion of the underlying metallic bond coat. The thermal gradient between the coating and the blade substrate can also lead to delamination of the TBC [28]. Cooling air which is bled from the compressor also carries ingested particles to the internal cooling passages. Particles impacting cooling passage surfaces deposit as mostly unreacted CMAS where, because of the combination of high-pressure flow and the high temperatures at cooling-passage wall surfaces, deposited particles can sinter to one another and the surfaces of the cooling passages. Murugan et al. [16] used scanning acoustic microscopy for subsurface imaging of the guide vanes shown in Fig. 4(*c*). They determined that in addition to the buildup of CMAS on vane surfaces and visible clogging of cooling holes, "the subsurface air channel was also significantly clogged by sand." This reduces the cooling air mass flow, leading to further increases in surface temperatures which further increases the rate of particle deposition and sintering and the blockage of flow [29]. Within the internal passages of turbine blades, particles can also deposit on the ribs constructed for improving heat transfer [30]. In addition to reducing the cooling channel cross-sectional area, the low thermal conductivity of these internal deposits can isolate the hot blade surface by acting as a thermal barrier between the blade and the cooling flow. This further reduces heat transfer, compounding the reduction in air flow, and leading to increased blade temperatures which can contribute directly to the structural failure of the blade.

2.2 Dimensionless Parameters. The process of particle-wall interaction is dynamic and nonlinear. There are several forces spanned across disparate scales that are involved during this process, including elastic-plastic stress, electrostatic forces, capillary forces, and van der Waals adhesion forces. The outcome of such interactions will depend on a multitude of variables associated with the properties of the surface, the particles, and the continuum phase. Dimensionless parameters can help in reducing the dimensionality of such a system by developing fundamental relations between system variables and identifying key behavioral regimes based on the operating conditions. A large number of dimensionless groups can be found in the literature that represent the multiphase flow characteristics through some form of correlation or predicted behavior. The dimensionless groups that are most relevant to the multiphase particle-wall interaction problem are discussed (in alphabetical order) in this section. Note that the subscripts p, d, and g refer to particle, droplet, and gas, respectively. In this section, a particle can be either liquid or solid while a droplet is exclusively a liquid particle.

2.2.1 Coefficient of Restitution. The key parameter that governs the outcome of collision of a particle with either another particle or a surface is the coefficient of restitution. Mathematically, this coefficient defines the ratio of postcollision to precollision relative velocity. The coefficient of restitution takes into account the effect of energy losses during a collision. For gas–solid or "dry" collisions, the effects of interstitial fluid are negligible and the energy dissipation of inelastic collisions is characterized solely by the coefficient of restitution. If the collision is perfectly head-on, the normal dry coefficient of restitution is used

$$e_{n,dry} = \frac{u_{\text{out},n}}{u_{\text{in},n}} \tag{1}$$

where $u_{\text{out},n}$ and $u_{\text{in},n}$ are the normal velocities between the two colliding bodies during rebound and incidence, respectively. For oblique collisions, the incident angles pre and postcollision must be considered and are commonly referred to as effective angles of incidence and rebound

$$\psi_{\text{in}} = \frac{u_{\text{in},t}}{u_{\text{in},n}} \tag{2}$$

$$\psi_{\text{out}} = \frac{u_{\text{out},t}}{u_{\text{in},n}} \tag{3}$$

where the subscript t indicates the tangential component of relative velocity. Another common term that is used to address non-normal collisions is the kinematic coefficient of restitution, which is the ratio of the magnitudes of the rebound and incident velocities.

2.2.2 Drag Coefficient. The drag coefficient of a particle is defined as the ratio of the drag force exerted on the particle by the dynamic pressure over the particle cross-sectional area

$$C_D = \frac{8F_d}{\pi\rho_g u_g^2 d_p^2} \tag{4}$$

The drag coefficient is useful to estimate the drag force from the gas flow characteristics. It strongly depends on the particle Reynolds number (Eq. (12)). For $\text{Re}_p \leq 1000$, the drag coefficient can be estimated using the Schiller–Naumann correlation [31]

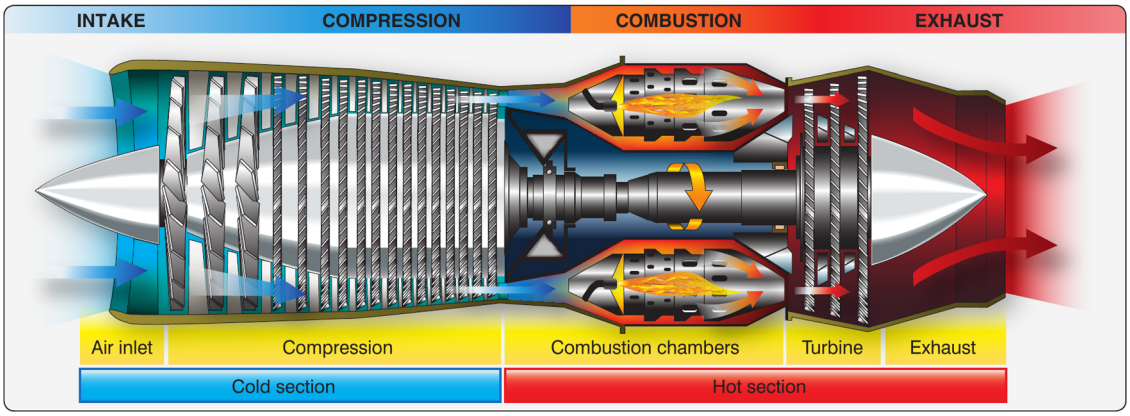

Fig. 2 Representative gas turbine engine [15]

$$C_D = \frac{24}{\mathrm{Re}_p}\left(1 + 0.15\mathrm{Re}_p^{0.687}\right) \tag{5}$$

For $\mathrm{Re}_p > 1000$, the drag coefficient of a spherical particle is approximately equal to 0.44. In the Stokes regime (i.e., $\mathrm{Re}_p < 1$), the drag coefficient is $24/\mathrm{Re}_p$.

2.2.3 Jakob Number. The Jakob number compares the change of sensible energy to the latent heat of vaporization. It is given by

$$\mathrm{Ja} = \frac{c_p(T_w - T_{\mathrm{sat}})}{L_{vap}} \tag{6}$$

where the term c_p is the mass heat capacity, the difference $T_w - T_{\mathrm{sat}}$ is the temperature change due to superheating of the wall and L_{vap} is the latent heat of vaporization of the liquid. In the context of film boiling, the Jakob number represents the amount of energy available to be transferred from the wall to the liquid relative to the amount of energy necessary to vaporize the liquid. Lower Jakob numbers represent a smooth film boiling, where the departure of the vapor bubbles is controlled by surface tension. Higher Jakob numbers depict a strong vaporization process at the wall, also referred to as flash evaporation, where the bubble departure is controlled by inertia.

2.2.4 Laplace Number. The Laplace number is used in characterizing free surface fluid dynamics and is defined as the ratio of surface tension to momentum transport. It is expressed as

$$\mathrm{La} = \frac{\sigma\rho L}{\mu^2} = \frac{\mathrm{Re}^2}{\mathrm{We}} \tag{7}$$

Note that the Laplace number is the inverse square of the Ohnesorge number (Eq. (11))

$$\mathrm{La} = \frac{1}{\mathrm{Oh}^2} \tag{8}$$

Laplace number can also be thought of as a Reynolds number for self-similar liquid behaviors in the absence of external forcing by using the capillary velocity as the velocity scale as suggested by McKinley and Renardy [32]

$$\begin{aligned} V_{\mathrm{cap}} &\sim L/t_{\mathrm{visc}} \\ t_{\mathrm{visc}} &\sim \mu L/\sigma \\ \mathrm{La} = \mathrm{Oh}^{-2} &= \frac{\rho(\sigma/\mu)L}{\mu} = \frac{\rho\sigma L}{\mu^2} \end{aligned} \tag{9}$$

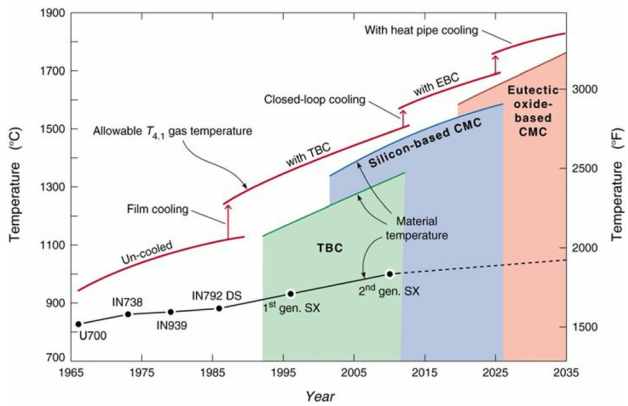

Fig. 3 Past and future trend of allowable gas temperature at the gas turbine inlet attributed to alloy development, and to advances in cooling technologies and thermal barrier coatings. Image [copyright] Haydn N. G. Wadley. Reproduced with permission from the author [20].

Since Laplace number is generally defined for free slip flows, the appropriate length scale, L to define it must relate to the curvature of the interface; droplet size, capillary length, and radius of curvature are the most commonly used length scales to define La [33].

2.2.5 Nusselt Number. The Nusselt number is used to quantify the heat convection over a surface with respect to its internal diffusive conduction

$$\mathrm{Nu} = \frac{hL}{k_g} \tag{10}$$

where h, L, and k are the convective heat transfer coefficient, a characteristic length and the thermal conductivity, respectively. Contrary to other numbers, its primary use is not to characterize the threshold between different regimes, but to estimate the heat

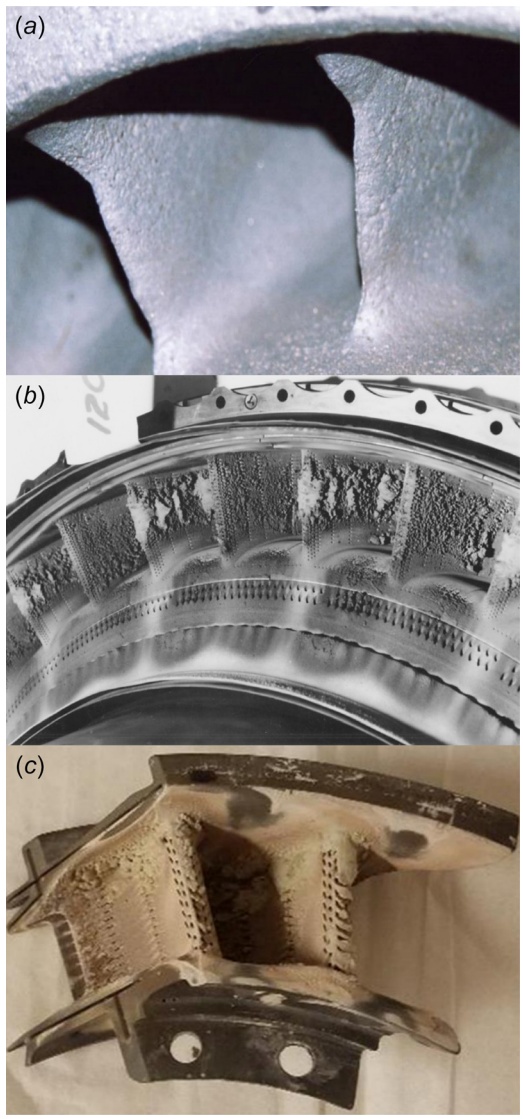

Fig. 4 Degradation mechanisms within gas turbine engine: (*a*) erosion [23]. Reproduced figure from *47th Turbomachinery & 34th Pump Symposia*, Linden, D., 2018. Copyright 2018, with permission from Turbomachinery Laboratory, Texas A&M Engineering Experiment Station, (*b*) deposition. Image [copyright] 2005 by the authors. Reproduced with permission from the first author [13], (*c*) blockage of cooling holes on leading edge of guide vanes [16].

flux transferred by natural or forced convection. The convective flux depends on many operating parameters of the surrounding fluids whereas heat conduction relies solely on the thermal properties of the considered object.

2.2.6 Ohnesorge Number. The Ohnesorge number incorporates the competition between the droplet inertia, viscosity, and surface tension. It can be used to distinguish between conditions that lead to different modes of liquid jet breakup and droplet formation as well as to characterize the driving forces for initial droplet spread upon impact with a solid substrate. The Ohnesorge number can be expressed as

$$\mathrm{Oh} = \frac{\mu_l}{\sqrt{\rho_d D_p \sigma}} = \frac{\sqrt{\mathrm{We}}}{\mathrm{Re}} \tag{11}$$

Note that as no velocity appears in its expression, the Ohnesorge number only depends on the mechanical properties of the liquid composing the droplet and on its size. The Ohnesorge number can also be regarded as the ratio of (i) the visco-capillarity time scale for the thinning of a ligament $\mu L/\sigma$ dominated by viscosity and (ii) the Rayleigh breakup time scale for an inviscid jet $\sqrt{\rho L^3/\sigma}$.

2.2.7 Particle Reynolds Number. The Reynolds number is used in predicting if a flow field is laminar or turbulent. Ranges of Reynolds numbers at which flow transitions from laminar to turbulent have been determined empirically for a wide variety of interactions, including internal flows, external flows, flows with an injected jet, flows with entrained particles, etc. The magnitude of a Reynolds number can be found by taking the ratio of the fluid inertial and viscous forces. For particle-laden fluid flows in which the fluid is a gas and the particles are either solids or liquid droplets, inertial effects are dominated by particle properties [11]. This leads to the Reynolds number, or what is sometimes described as a particle Reynolds number, that is defined as

$$\mathrm{Re} = \frac{\rho_g U_{gp} D_p}{\mu_g} \tag{12}$$

where ρ_g, U_{gp}, and D_p are the gas density, relative velocity between the gas and particle phases, and the particle diameter, respectively, and the term μ_g is the gas viscosity.

2.2.8 Particle Volume Fraction. For dispersed multiphase flows, the particle volume fraction describes the portion of a given multiphase fluid volume which is occupied by particles or droplets

$$\Phi_p = \frac{N_p V_p}{V} \tag{13}$$

where N_p is the number of particles or droplets, V_p is the volume of a single particle, and V is the volume occupied by particles and fluid.

2.2.9 Prandtl Number. The Prandtl number is used to characterize the relative contributions of convection and conduction in the heat transfer processes that produce temperature gradients in a fluid when the fluid moves past a surface at a different temperature. The Prandtl number is defined using the ratio of the momentum diffusion rate to the thermal diffusion rate and is expressed as

$$\mathrm{Pr} = \frac{\mu c_p}{k} \tag{14}$$

where μ is the dynamic viscosity, c_p is specific heat and k is the thermal conductivity. Although the Prandtl number does not contain a length scale and is dependent only on fluid properties (i.e., not flow field properties), the Prandtl number governs the thickness ratio of the thermal (conductive) boundary layer and the momentum (convective) boundary layer. In fluids with Pr values much greater than 1, heat transfer to the fluid is dominated by momentum-driven convective heat diffusion. In fluids with Pr values of 1, convective and conductive heat diffusion rates are similar. In fluids with Pr values of much less than 1, conductive heat transfer dominates. The Pr is used in characterizing heat transfer in laminar flows. A related term that is used for turbulent flows is the effective Prandlt number, which is the sum of the Prandlt number and the turbulent Prandlt number. The turbulent Prandtl number depends on flow field properties (rather than just on fluid properties) and is given by the ratio of eddy viscosity and eddy heat diffusivity.

2.2.10 Stokes Number. The Stokes number is used to characterize the behavior of particle responses to the carrier-phase gas and is defined as the ratio of the dispersed-phase inertia to the carrier-phase inertia

$$\mathrm{St} = \frac{\tau_p}{\tau_g} \tag{15}$$

where τ_p is the particle response time and τ_g is the characteristic time scale of the gas phase. For particle-laden flows where the particle-to-fluid density ratio ρ_p/ρ_g is high, the particle response time becomes

$$\tau_p = \frac{\rho_p D_p^2}{18\mu_g} \tag{16}$$

In general, the carrier-phase response time is defined as a characteristic length l_0 divided by a characteristic velocity u_0

$$\tau_g = \frac{l_0}{u_0} \tag{17}$$

When considering particle motion through a turbulent flow, the response time is typically defined as the integral time scale of turbulence

$$\tau_g \approx \frac{k}{\varepsilon} \tag{18}$$

where k is the turbulent kinetic energy and ε is the dissipation rate of turbulent kinetic energy. Stokes numbers based on macroscopic time scale (Eq. (17)) and on turbulent time scale (Eq. (18)) are noted St_m and St_t, respectively.

2.2.11 Weber Number. The Weber number is used to characterize the stability of droplets moving through a gas or liquid. Inertia forces due to droplet motion promote droplet deformation, which is opposed by surface tension forces. The Weber number is the ratio of the destabilizing effect of the droplet inertia (resp. the aerodynamics stress) to the stabilizing effect of the droplet surface tension. It is expressed as

$$\mathrm{We}_p = \frac{\rho_d U_d^2 D_d}{\sigma} \quad \text{resp.} \quad \mathrm{We}_g = \frac{\rho_g \mathrm{U}_{gd}^2 \mathrm{D}_d}{\sigma} \tag{19}$$

where σ is the surface tension coefficient. A Weber number lower than 12 indicates a stable droplet that will not (further) break up [34]. Depending on the type of application, We_p or We_g are preferred. Typically, We_p is used for droplet/wall impacts and We_g for atomization.

2.2.12 Nominal Values in the Different Aeroengine Components. The order of magnitude of the air properties in the different sections of a gas turbine engine are given in Table 1. They were estimated as follows. As particle ingestion occurs at low altitude, we assume typical inlet conditions at 1 atmosphere and 20 °C. In the compressor, we consider a polytropic compression of index 1.4 and pressure ratio 30. We neglect pressure loss from the

compressor outlet to the turbine inlet. The mean temperature after the flame and upstream dilution is estimated to be 2000 K [35,36] and turbine inlet temperature is assumed to be 1800 K (Fig. 3). The velocity in the different components is taken from [37]. Concerning the particulate, the density and the specific heat are rather constant all along the stages. When the particulates are cold (up to the combustor inlet) it can be considered as a solid and hence its viscosity and surface tension are not applicable (N/A). After combustion, CMAS starts to melt and hence these quantities can be estimated. The mechanical properties are summarized in Table 2, based on data found in Refs. [38,39]. We consider here particulates from 3 to 30 μm diameter and we estimate their velocity to be 80% of the surrounding gas. Studies have shown that commercial aircrafts flying through volcanic ash clouds may be exposed to particle concentrations up to 2 g/m^3 [1]. In addition, a study which characterized brownout conditions for various helicopters showed particle concentrations at the rotor tip to be as high as 3.5 g/m^3 [40]. This range of particle concentrations corresponds to a particle volume fraction ranging from e-7 to e-6. Based on these considerations, the nondimensional numbers are summarized in Table 3.

3 Solid Particle-Laden Fluid Flow

3.1 Flow Characterization. Dispersed multiphase flows are ubiquitous in both nature and engineering with common examples including atmospheric dispersal of pollutants, liquid sprays in engines, and sedimentation of sand particles in river beds. Universally, these particle-laden fluid flows contain finite particles which are distributed within a continuous fluid carrier phase. The particles, classically referred to as the dispersed phase, can be gaseous bubbles, liquid droplets, or solid particles. There are five classifications of particle-laden fluid flows based on their carrier-dispersed phase composition: gas–solid, liquid–solid, gas-droplet, liquid-droplet, and liquid–gas [41]. For the application of heterogeneous multiphase flows in gas turbine engines, this paper will focus on solid and liquid dispersed phases. Since the underlying physics and mechanisms of particle-wall interactions are fundamentally different for solid and liquid particles, this section will focus on gas–solid and liquid–solid flows while Sec. 4 will focus on gas-droplet and liquid-droplet flows.

A classification system suggested by Elghobashi [42] presents three coupling strategies for particle-laden flows which offer varying degrees of mathematical fidelity. These coupling regimes are based on interaction mechanics and turbulence modulation. The dispersed-phase volume fraction Φ_p is used to delimit the fidelity requirements for mathematical modeling. For particle-laden flows with very low volume fractions (i.e., $\Phi_p \leq 10^{-6}$), the one-way coupling regime indicates that interparticle spacing is very large and particle concentration is very low such that turbulence in the carrier phase has dominating effects on the dynamics of the dispersed phase. In the one-way coupling regime, momentum transfer is only considered from the carrier phase to the dispersed phase. For particle volume fractions between the range of 10^{-6} to 10^{-3}, the particle concentration becomes large enough to lead to modifications in the carrier-phase turbulence. In this two-way coupling regime, turbulence can either be dissipated or enhanced as a function of the particle diameter, requiring direct feedback of momentum transfer between the carrier and dispersed phases. Both the one-way and two-way coupling regimes are classified as dilute suspensions where particle dynamics are mainly governed by surface and body forces acting on them through the carrier phase. As the particle volume fraction becomes even larger (i.e., $\Phi_p > 10^{-3}$), particle concentration becomes significantly larger and interparticle spacing becomes significantly smaller [41], leading to the dense suspension classification which necessitates four-way coupling. In the four-way coupling regime, fluid-particle momentum transfer, as well as particle–particle interactions, must be considered.

Section 2 and Table 3 illustrate typical particle concentrations found in the surrounding external flow of aircraft in critical particle-laden environments. However, there is no experimental data to indicate the particle concentrations present inside of the gas turbine. At best, estimates based on the external particle-laden flow can be used to further classify particle-laden gas turbine flows. This range of particle concentrations corresponds to a particle volume fraction ranging from e-7 to e-6. Based on the previously outlined classification, this places the particle-laden flow in gas turbine engines on the boundary of the very dilute to moderately dilute regimes. A thorough review of particle transport and deposition for very dilute mixtures with an emphasis on the one-way coupling regime can be found in the work by Guha [12]. The current review paper focuses on the two-way coupling regime for moderately dilute suspensions. In addition, the particles Stokes number range shows that particles are of the order of or larger than the scales of dissipative carrier-phase eddies. In the range of particle volume fractions of interest, as described by Balachandar and Eaton [11], Lagrangian point-particle and fully resolved approaches are most appropriate. For further details on different computational approaches to model particle-laden flows based on relative particle sizes and/or Stokes number and appropriate coupling strategies, the readers are encouraged to refer to previous review papers on the topic [11,43,44].

3.2 Particle Transport

3.2.1 Description of Particle Motion. Obtaining a complete description of a particle-laden flow field requires the instantaneous states of the dispersed and carrier phases to be known. For a system containing a total of N_p particles, the position $\mathbf{x}_i$ and velocity $\mathbf{v}_i$ must be characterized for all particles from $i = \{1, \ldots, N_p\}$. The position of particle i is characterized by the kinematic equation

$$\frac{d\mathbf{x}_i(t)}{dt} = \mathbf{v}_i \tag{20}$$

and the velocity of particle i is characterized by

$$m_i \frac{d\mathbf{v}_i(t)}{dt} = \mathbf{F}_b + \mathbf{F}_s + \sum \mathbf{F}_{\text{int}} \tag{21}$$

where m_i is the mass of the *ith* particle and the right-hand side is the sum of the body forces $\mathbf{F}_b$, surface forces $\mathbf{F}_s$, and interaction forces $\mathbf{F}_{\text{int}}$ acting on the particle. Equations 20 and 21 are then coupled to the Navier–Stokes equations in order to fully characterize the particle-laden flow field. Note that while both body and surface forces are considered in the two-way and four-way coupling, the interaction forces are only considered in four-way

Table 1 Typical values of flow parameters at different location of the gas turbine [35–37]

	Pressure (atm)	Temperature (K)	Density (kg/m^3)	Viscosity (Pa s)	Thermal conductivity (W/(m K))	Heat capacity (J/(kg K)	Length scale (m)	Velocity (m/s)
Intake	1	300	1.2	1.8×10^{-5}	0.025	1007	1	180
Combustor inlet	30	800	14	3.62×10^{-5}	0.058	1098	0.01	60
Upstream dilution	30	2000	5.3	6.20×10^{-5}	0.11	1251	0.01	150
Turbine inlet	30	1800	5.9	5.83×10^{-5}	0.099	1237	0.01	500

Table 2 Mechanical properties of CMAS material at $T = 1523$ K [38,39]

Density (kg/m^3)	Heat capacity (J/(kg K))	Viscosity (Pa s)	Surf. tens. (N/m)	Diameter (μ m)
2700	800	5	0.35	3–30

Table 3 Typical values nondimensional parameters at different location of the gas turbine. Ranges correspond to particulates between 3 and 30 μm

	$\mathbf{Re}_g$	$\mathbf{Re}_p$	$\mathbf{We}_d$	**Oh**	St_m	**Pr**
	$\times 1000$			$\times 0.001$		
Intake	12000	7.02–70.2	N/A	N/A	0.0132–1.32	0.707
Combustor inlet	225	13.5–135	N/A	N/A	0.224–22.4	0.690
Upstream dilution	130	7.69–76.9	333–3330	8.32–26.3	0.326–32.6	0.728
Turbine inlet	500	30.2–302	3700–37000	7.42–23.5	1.16–116	0.728

coupling regimes. In addition, forces that would be introduced due to rotation of translating particles (e.g., Magnus effect-induced transverse forces) have been shown to significantly affect heat, mass, and momentum transfer in internal flows with a low Reynolds number and high particle rotation rates. Kajisjima et al. [45] observed that in regions of cooling channels with low velocity, for particle Reynolds numbers of 300–400, particle clustering was impacted (both promoted and diminished) by Magnus force effects. As the current review largely focuses on engine regions with lower particle Reynolds numbers (Table 3) Magnus forces due to particle rotation are mentioned as a factor that may merit further consideration, but that will not be discussed further in this work.

Particle-laden turbulent flows can exhibit various phenomena such as turbulence modulation, preferential concentration, and turbophoresis. Gore and Crowe [46] presented a summary of various experimental results of dilute particle-laden free shear flows which demonstrated a noticeable modification in turbulence intensity as a function of particle diameter. They found that particles larger than the integral length scale cause an increase in turbulence intensity while smaller particles cause a decrease. Kulick et al. [47] found that in dilute channel flows, particles attenuated turbulence when Stokes number, particle mass loading, and distance from the wall increased. Squires and Eaton [48] found that lighter particles are more susceptible to preferential concentration in areas of high strain rate and low vorticity. They also showed that heavier particles are more uniformly dispersed in turbulence. Turbophoresis is another phenomena which causes a nonuniform distribution of particles in the near-wall region [49]. Turbophoresis is driven by a differential in turbulent dispersion rates between different flow regimes. Marchioli et al. [50,51] found that strongly coherent sweeps drive particles toward the wall while strongly coherent ejections drive particles toward the outer flow. These studies also found that deposition of heavy particles is strongly influenced by the effects of turbophoresis.

3.2.2 Experimental Studies of Particle Transport in Engine-Like Conditions. Table 1 indicates that the carrier-phase flow within the turbine is turbulent given the high Reynolds number. In addition, the particle volume fraction range shows that the particle transport of CMAS through the turbine is somewhere on the boundary of dilute to moderately dilute. Balachandar and Eaton [11] recap experimental studies concerning fluid-particle interactions in turbulent channels but state that there is still a need to develop experimental techniques that are capable of fully resolving the flow surrounding the particle phase. Fong et al. [52] provide a comparative table of gas–solid experiments over a range of Reynolds number, Stokes number, and particle volume fractions. However, they note that there still exists a gap in experimental data for particle-laden flows that sit on the boundary between dilute and moderately dilute suspensions. In their research, they experimentally observe the velocity and spatial distributions of monodispersed glass particles in a vertical turbulent channel. Their work considers volume fractions and Stokes numbers that are expected to occur within the turbine of an aeroengine. However, given the extreme conditions within the turbine, it remains very difficult to experimentally observe particle transport behavior in engine-like conditions. As such, the remainder of this section will focus on computational approaches that are being used to help study the transport properties of particle-laden turbulent flows.

3.2.3 Particle-Resolved Methods. Direct numerical simulation (DNS) is a first-principle approach used to establish a complete description of the carrier-phase flow dynamics at all scales without the need for a closure model [53]. In particle-resolved direct numerical simulation (PR-DNS), particles of finite size are coupled to the carrier-phase flow field through the enforcement of the no-slip, no-penetration condition at the boundary of each particle. The particle interface is discretized such that the fluid dynamic forces acting on the boundary of each particle are computed directly using the flow field solution. Particle positions and velocities are then explicitly determined based on the surface forces and interaction forces acting on the particle [54].

In a review on turbulent dispersed multiphase flow, Balachandar and Eaton [11] recommended that future research should seek to advance PR-DNS capabilities as a means of studying particle-laden flows for particles larger than the Kolmogorov length scale. The primary advantage of PR-DNS is its capability to fully resolve the flow field surrounding the dispersed phase, exposing the underlying physics of particle-laden flows. In addition, PR-DNS can be used to develop closure models for lower fidelity simulations [54]. There have been several notable works which offer a wide-variety of PR-DNS methods for particle-laden flows. These methods utilize a structured Eulerian grid for the carrier phase while implementing various techniques to resolve the dispersed phase.

The grid overset method attaches a body-fitted grid to the dispersed phase particles and overlays this onto the carrier phase structured grid, coupling these independent grids through interpolation. The advantage of this method comes from the carrier phase structured grid which is capable of capturing the full range of turbulent scales while the body-fitted grid is capable of fully resolving the effects of the no-slip condition on each particle. Early work by Bagchi and Balachandar [55] tested the validity of using a body-fitted grid for a single particle in decaying isotropic turbulence. The earliest implementation of an overset grid for particle-laden flows was by Burton and Eaton [56] when they studied a single, fixed particle in decaying isotropic turbulence. Vreman [57] extended their study by using the overset grid method for multiple stationary particles in stationary homogeneous isotropic turbulence. Recently, Koblitz et al. [58] applied an overset grid to a small number of moving particles in a quiescent flow to determine the viability of this method for studying particle-laden flows.

Despite being able to produce highly resolved flow around each particle, the overset method suffers from major computational disadvantages, namely, the expense of numerical interpolation and the regeneration of the moving body-fitted mesh.

Fixed-grid methods use a stationary Eulerian grid with Lagrangian points added to the surface of each particle. The no-slip condition is enforced on these surface points through an additional source term in the Navier–Stokes equations. The primary fixed-grid methods used in PR-DNS are fictitious domain methods and Lattice Boltzmann methods. Glowinski et al. [59] developed a fixed-grid fictitious domain method which used Lagrange multipliers to introduce a pseudo-body force inside the particles in order to enforce rigid body motion. Various works expand on this method [60–62], with recent work by Yu et al. [63] implementing this method in parallel to study the effects of particle inertia in a turbulent channel flow. Other fictitious domain methods include those developed by Kajishima [45] and Takiguchi [64] which set the velocity in the particle interior to the rigid particle velocity and used volume averaging near the boundary to study particle-laden homogeneous turbulent flow in vertical channels. For more detail on the various fictitious domain implementations, see Haeri and Shrimpton [65].

A popular subset of the fictitious domain methods is the immersed boundary method (IBM). Unlike the aforementioned fictitious domain methods, IBM only considers the forces on the surface of the particle, as opposed to the interior. In IBM, a body forcing term is added to the Navier–Stokes equations at the Lagrangian boundary points in order to enforce the no-slip condition. Uhlmann [66] used IBM to study preferential concentration and particle-induced flow structures in a vertical plane channel with thousands of solid particles at high Stokes numbers. Lucci et al. [67] expanded on this method to study the effects of solid particles on turbulence modulation in decaying isotropic turbulence. Picano et al. [68] used a four-way coupled IBM to study neutrally buoyant spheres in solid–liquid dense suspensions. Mehrabadi et al. [69] quantified gas-phase velocity fluctuations due to mean slip velocity in dense gas–solid flows. Recent works have focused on improving the computational efficiency of IBM solvers [70,71], with an article by Kajishima [72] detailing the specific developments for IBM methods in particle-laden flows. It should be noted that IBM is known to produce erroneous surface stresses when using imposed boundary conditions to determine surface forces [73].

Another popular technique for PR-DNS is the Lattice-Boltzmann method (LBM). This approach resolves the transport equation of the presence probability density function of gas particles, the so-called Boltzmann equation. The collision term between the gas particles is modeled. The state variables such a density, pressure, and temperature are reconstructed from the higher moments of the distributions of particle number and velocity. This method has the advantage of being computationally inexpensive and appropriate for parallelization, hence allowing massively parallel simulations [74] and finer spatial resolutions. LBM has been used to study the transport, collisions, and agglomeration of dense particle suspension [75] as well as particle aggregation of solid–liquid suspensions in homogeneous isotropic turbulence [76]. Hölzer et al. [77] used LBM to quantify forces and moments on particles with spherical and nonspherical shapes while allowing for particle rotation and linear fluid shear. Recent studies [78–80] have applied LBM to the simulation of particle-laden, wall-bounded turbulent flow. In most of these studies, LBM uses the "bounce-back" rule to establish the surface boundary condition. In order to properly resolve the no-slip boundary condition, the "bounce-back" rule requires a large number of lattice grids for each particle. To circumvent this issue, some studies [81,82] have combined LBM with IBM.

3.2.4 Lagrangian Methods. While the particle-resolved methods are able to capture highly detailed flow around each particle, these approaches are limited by computational expense and thus only applicable for a relatively small number of particles. For the simulation of millions of particles, the Euler–Lagrange approach is often employed. In this method, the carrier-phase is represented in an Eulerian reference frame while the dispersed phase is represented in a Lagrangian reference frame. At the core of the Lagrangian method is the point-particle assumption, which presumes that the dispersed-phase particles are smaller than the Kolomogorov length scale. Consequently, this allows them to be modeled as dimensionless point sources. In this representation, the boundary condition around each particle is not imposed and instead a model is required to represent the interphase transfer. The typical solution methodology for the Eulerian- Lagrangian solvers with four-way coupling can be decomposed into four major steps. The first step is to solve the unladen carrier-phase flow field with the Eulerian framework. The second step is to solve the particle motion with the Lagrangian framework by using the solution from the first step to determine the relevant forces acting on each particle. The third step is to recompute the carrier-phase flow field with updated source terms from the dispersed phase solution. The final step is to update the dispersed phase solution to include interparticle collisions.

For spherical particles that are smaller than the Kolomogorov length scale, Maxey-Riley [83] and Gatignol [84] derived an expression for the particle equation of motion which includes a description of all of the relevant forces acting on the particle. These forces include the buoyancy force, the force caused by the undisturbed velocity field, the added mass force, the drag force, Basset history force, and Faxén corrections. Additional studies have led to the modification of this equation for applicability at higher Reynolds numbers [85,86] and compressible flow regimes [87]. It has been shown that for small and heavy particles (i.e., $\rho_p \gg \rho_f$), the Basset force, added mass force, and undisturbed velocity field force is negligible in comparison to the drag force and buoyancy force [88]. One of the key challenges in using the Euler–Lagrange method for two-way and four-way coupled systems comes from the dependency of the drag force on the undisturbed or unladen carrier-phase flow field. The computation of the Stokes drag on a particle depends on the particle velocity along with the undisturbed carrier-phase velocity at the position of the particle. However, the presence of the particle inherently adds a disturbance to the undisturbed carrier-phase velocity field, consequently contaminating the flow field. Recent studies have proposed various methods to estimate the undisturbed carrier-phase velocity field [89–91].

In regards to the accuracy of the Euler–Lagrange methods, it is important to note that there are various levels of modeling fidelity in terms of the carrier-phase flow field solution. As mentioned in the previous section, DNS is capable of resolving all of the scales of carrier-phase fluid motion. Thus, the highest-fidelity Euler–Lagrange method is known as point-particle direct numerical simulation (PP-DNS). Unlike PR-DNS, the interphase transfer between the dispersed and carrier phase must be modeled instead of explicitly resolved. A review by Mehrabadi et al. [92] compares the efficacy of PP-DNS models to PR-DNS.

When a filtering function is applied to the Navier–Stokes equations, the smallest scales of motion in the fluid phase are modeled while the larger scales are directly resolved. This method is commonly referred to as a point-particle large eddy simulation (PP-LES). Aside from requiring a model to close the subgrid stress tensor in the Navier–Stokes equation, PP-LES has additional terms which require subgrid models in the particle equation. Some studies have suggested that the subgrid scales in the fluid velocity do not significantly impact the motion of the particles, thus allowing the subgrid model in the particle equation of motion to be neglected [93,94]. However, Kuerten and Vreman [95] show that for larger particle relaxation times, the subgrid models cannot be neglected due to their significant impact on turbophoresis. Kuerten [96] provides a thorough review of the various subgrid models for PP-LES along with a review on PP-DNS methods.

The simplest of all the Euler–Lagrange methods is point-particle Reynolds-averaged Navier–Stokes (PP-RANS). In PP-RANS, a statistical description of the carrier-phase flow is used and as such, significant computational savings are earned. While

requiring significantly less computational efforts than PP-LES or PP-DNS, PP-RANS requires additional models to include the effects of turbulence. Stoichastic dispersion models are required to determine the effects of turbulence on the particles motion.

The treatment of collision modeling is an additional method used to categorize Euler–Lagrange methods. For moderately dilute and dense suspensions, the two Euler–Lagrange methods are the discrete particle model (DPM) and the discrete element method (DEM). DPM makes use of the hard-sphere collision model whereas DEM makes use of the soft-sphere model. Both hard-sphere and soft-sphere models will be discussed in detail in Sec. 3.3.

3.2.5 Eulerian Methods. While there have been some studies which have used the Lagrangian point-particle approach to simulate particles that are larger than the Kolomogorov length scale, there still remains a question of its validity given the mathematical formulation of the point-particle approach [97]. In addition, while Euler–Lagrange simulations can give a detailed history of particle temperature and mass change, these methods become computationally intractable for systems which have to track a very large number of particles. As such, the only other method aside from particle resolved methods which can simulate particles that are larger than the Kolomogorov length scale and also have a relatively low computational cost are Euler-Euler methods. There are two distinct Euler-Euler methods for particle-laden flows: the one-fluid (equilibrium) method and the two-fluid model. In both of these Euler-Euler approaches, particles are no longer represented individually but as a continuous fluid media. The Euler-Euler models are developed from a kinetic theory of gasses approach in which the molecules are handled statistically. This leads to a system of particle differential equations which represent the gas as a continuum media. The downside to using an Euler-Euler approach is that it results in additional modeling requirements due to closure problems as a result of the statistical problem formulation.

In the one-fluid approach, particles are assumed to be sufficiently small that their motion is dictated by the surrounding carrier-phase fluid. The density of the fluid in this approach depends on the mass-fraction of the dispersed phase and the velocity is expressed as a function of the Stokes number and local carrier-phase velocity. This method requires only the momentum and energy equations of the carrier-phase to be solved along with the equation for particle concentration [11]. While this approach benefits from its computational simplicity, it is limited to suspensions with very low Stokes numbers [98–100].

For larger Stokes number flows, the two-fluid approach is more appropriate. In this approach, the dispersed phase is represented by particle concentration and velocity such that momentum and energy equations are solved for both the carrier phase and the dispersed phase. To couple the phases, source and sink terms are used to account for momentum and energy transfer. The two-fluid model approach is often employed to simulate fluidized beds [101–103] and riser columns [104,105]. Other studies, such as the one performed by Moreau et al. [106], developed an Euler-Euler LES approach to simulate dilute suspensions in homogeneous isotropic turbulence. Masi et al. [107] used an Euler-Euler DNS approach to examine particle-laden turbulent flows in very dilute suspensions. Kartushinsky et al. [108] applied a RANS-based Eulerian method to study finite-sized neutrally buoyant solid particles in pipe flow. In a study by Chen and Wang [109], the efficacy of the two-fluid method for impinging gas–solid jets was examined in comparison to Euler–Lagrange approaches. They directly compared the two-fluid method to both DPM and DEM, concluding that two-fluid model failed to predict the particle trajectory crossing effect in dilute systems.

3.3 Particle Collisions

3.3.1 Description of Particle Collision and Particle-Wall Interactions. In moderately dilute suspensions, particle–particle and particle-wall collisions play an important role in the dynamic behavior of the flow. It is, therefore, necessary to understand both the primary transport mechanisms and collision mechanics that occur in particle-laden flows. For very small particles (i.e., $d_p < 1\mu m$), particle collisions occur primarily due to random Brownian motion. For particles with a small Stokes number, collisions can occur due to particles following streamlines at different positions in the flow field. In laminar flows, particles with different settling velocities can lead to collisions. In turbulent flows, particle inertia can lead to particles deviating from streamlines, preferentially concentrating, and colliding. For large particles with large Stokes numbers in turbulent flows, particle collisions occur as particles are displaced by the various turbulent eddies. While Meyer and Deglon [110] provide a comprehensive list of the various collision mechanisms and corresponding models, the focus of collision modes in this paper is on accelerative mechanisms found in turbulent flows.

In this regime, early theoretical work by Davis et al. [111] indicates that the Stokes number is a key parameter governing particle collisions. When oblique particle-wall collisions occur, Maw et al. [112] showed that particles can either fully stick to the surface, partially stick and slide over the surface, or completely slide over the surface. As such, dry collisions require the coefficient of restitution as the primary input parameter to predict the outcomes of particle–particle and particle-wall interactions. Additional work by Yamamoto et al. [113] found that interparticle collisions encourage transverse mixing which in turn leads to a flattening in the particle velocity and particle concentration profiles. They also found that interparticle collisions play a significant role in the near-wall region, specifically in the dispersion of particles in the transverse direction.

For liquid–solid or "wet" collisions, the effects of interstitial fluid between colliding objects become significant and an effective coefficient of restitution must be used to account for viscous dissipation and the kinetic energy that is required to displace the fluid between the colliding surfaces. Barnocky and David [114] studied the rebound of particles colliding with a wall overlaid with a viscous fluid while Gondret et al. [115] examined particle-wall collisions of fully immersed walls. In these works, the coefficient of restitution was presented as a function of Stokes number. It was shown that for low Stokes number, particle energy during collision is dissipated into the surrounding fluid, and no rebound is observed. However, for larger Stokes numbers the coefficient of restitution becomes strongly dependent on the particle Stokes number. Additional studies by Joseph et al. [116,117] examined the approach and rebound of heavy particle-wall collisions in viscous fluids and found the same Stokes number dependency of coefficient of restitution. Yang and Hunt [118] performed experimental studies of fully immersed particle–particle collisions and found similar correlations to particle-wall collisions. Lubrication effects caused by the interstitial fluids are difficult to numerically resolve due to excessive grid refinement requirements, however, Glowinski et al. [59] were able to directly capture the motion of the interstitial fluid. Nevertheless, lubrication models are often used to quantify the short-term hydrodynamics in wet collisions [81,119,120].

3.3.2 Collision Physics of Molten Sand Particles. Droplet collision of liquids such as water and hydrocarbons relevant to propulsion applications has been extensively studied in the past and the detailed collision dynamics, atomization, and breakup regimes are fairly well established [121–124]. However, not much was known about the collision physics of molten sand particles until the recent studies on equal and unequal binary collision of CMAS droplets conducted by Ganti et al. [125,126]. The primary difference between CMAS droplets and other fluids that have been investigated in the past is the extremely high surface tension, density, and viscosity of molten sand particles, and even though the effect of viscosity on droplet collision has been studied in the past [127,128], CMAS viscosity and surface tension is at least two

orders of magnitude higher than any liquid studied in the literature.

Ganti et al. [125] used a volume-of-fluid-based direct numerical simulation approach to investigate how molten sand particles interact at operating conditions representative of contemporary gas turbine combustion chambers, for head-on, off-center, and grazing configurations. For equal droplets, it was found that for head-on and off-center collisions, due to the high Laplace number, the droplets coalesce into a pear-shape in the former and a stretched rotating structure with lobes at the end in the latter. Separation was observed for grazing binary collisions. The droplet collision physics was quantified using the evolution of the kinetic, dissipation, and surface energies associated with the CMAS droplets.

In a follow-up study, Ganti et al. [126] found that when two unequal CMAS droplets collide head-on, the smaller one is partially consumed by the larger droplet forming a mushroom shape. To identify the effect of viscosity, a fictitious fluid with all properties identical to CMAS except viscosity, reduced by a tenth, was also studied. It was found that head-on collision of unequal droplets of this fictitious fluid resulted in the formation of a thin liquid sheet that sheds ligaments and droplets in concentric circles around a central core. For off-center collision, it was found that both CMAS and the fictitious fluid result in the formation of an unsymmetrical dumbbell shape. While for CMAS droplets, this shape remains intact, for the other fluid, due to its lower viscosity, the dumbbell stretches and breaks up forming ligaments and satellite droplets.

3.3.3 Collision Modeling. There have been many four-way coupling studies which analyze interparticle collisions. Nasr et al. [129] examined turbulent channel flow with four-way coupling and found that when particle–particle collisions along with two-way coupling effects were included, particle deposition velocity increased substantially. Kempe and Fröhlich [119] used IBM to develop models for normal and oblique collisions which stretch the collision process in time as a means of promoting large-scale simulations of highly loaded suspensions. Haddadi et al. [130] used LBM to study the dilute suspension flow over obstacles and study the complex collisional interactions. Brändle et al. [120] developed a numerical model to study short-range hydrodynamic interactions of head-on particle–particle and particle-wall collisions in viscous fluids. This model accounted for lubrication effects between precollisional gaps and was validated over a wide range of Stokes numbers. Troiano et al. [131] experimentally simulated particle-wall interactions in dense entrained-flow slagging coal gasifiers. They examined the influence of particle stickiness, impact velocity and angle, and wall-surface properties and structure on coefficients of restitution by characterizing the impact-deposition-rebound dynamical patterns of particles colliding with a planar surface. Johnson et al. [132] use DPM-LES to explore near-wall modeling of turbophoresis in wall-bounded turbulence. Afkhami et al. [133] used DEM-LES with four-way coupling to study the effect of particle surface energy and fluid turbulence on particle agglomeration for turbulent flow in a channel.

There are several methodologies behind modeling interparticle collisions. One classification of particle collision modeling uses either stochastic or deterministic outcomes. In stochastic collisions, probability density functions are used to determine collision outcomes without using the particles true position or velocity [134]. Stochastic collisions benefit from computational efficiency due to the fact that individual particle–particle collision pairs need not be searched for at every time-step. However, the stochastic collision method requires the particle and fluid velocity fluctuations to be assumed and consequently may introduce a loss in the resolution of other significant physics, such as preferential concentration. A more common approach to collision modeling is to use deterministic methods. As the name suggests, deterministic methods use the true particle position and velocity to determine the collision outcomes. There are two methodologies for deterministic collision modeling: the hard-sphere approach and the soft-sphere approach.

3.3.4 Hard Sphere Model. The main difference between the hard-sphere model and the soft-sphere model is in the treatment of the particle deformation and friction. In the hard-sphere collision model, interactions between particles are event-driven such that collisions are processed in the time sequence in which they occur. Since the collisions are considered binary, they occur over a very short period of time and are described purely by impulse equations. For the hard-sphere approach, only the normal coefficient of restitution and the friction coefficient is required to compute the outcome of each collision. One of the most frequently used hard-sphere models for analyzing particle-laden flows was developed by Hoomans et al. [135]. Chen et al. [136] used the hard-sphere model to study droplet-droplet collision and deposition in turbulent channel flow. Li et al. [137] extended this work by applying the hard-sphere model for particle–particle collisions in turbulent vertical channel flows. Nasr et al. [129] used the hard-sphere model implemented by Li et al. to study the effects of various particle relaxation times and mass loadings on particle deposition. Fede and Simonin [138] used the hard-sphere model with one-way coupling to study the effects that subgrid fluid turbulence has on the motion of colliding particles in homogeneous isotropic turbulence, specifically regarding preferential concentration. Mallouppas and van Wachem [139] compared the hard-sphere and soft-sphere collisions models for moderately dilute suspensions in turbulent channel flows. They found that while both soft-sphere and hard-sphere models yielded similar fluid velocity statistics, the hard-sphere modeling assumptions breakdown as the suspension becomes more dense with particles.

3.3.5 Soft Sphere Model. The soft-sphere collision model was first introduced by Cundall and Strack [140]. In the soft-sphere approach, the collisions are fully resolved such that the model computes the actual deformation of the particles and the corresponding contact forces. Soft-sphere models use fixed time steps and are considered time-driven. When particle collisions occur, the normal forces acting on the particles are computed using a mass-spring-dashpot system in which the spring stiffness and dashpot coefficients are a function of the particles elastic properties. Many recent studies favor the soft-sphere modeling approach for moderately dilute and dense suspensions. Capecelatro and Desjardins [97] applied the soft-sphere model of Cundall and Strack to a DEM-LES framework to study dense fluidized beds. While their model was able to simulate particle–particle collisions, they noted that additional improvements needed to be made for particle-wall interactions. Luo et al. used PR-DNS [141] to determine the drag force in particles in fluidized beds. Luo et al. [142] also used PP-DNS to study the effects of preferential concentration on particle-wall interactions. Costa et al. [143] developed an IBM with the soft-sphere model in order to simulate moderately dense suspensions with finite-size particles. Their four-way coupling method was able to accurately capture the normal coefficient of restitution as a function of impact Stokes number for head-on particle–particle and particle-wall collisions. Deen et al. [144] provide a detailed review on various hard-sphere and soft-sphere methods and implementations for fluidized beds.

4 Droplet/Wall Impact

In this section, we review the literature on the outcome of the impact of a liquid droplet on a solid substrate. This configuration is referred to as droplet/wall interaction in the following. This section is motivated by the fact that above a given temperature, molten sand particles have the mechanical properties of a very viscous liquid [145]. We use the comprehensive reviews from [146–149] as a starting point. First, we describe the phenomenology based on experimental evidence. Then, the different numerical strategies to describe drop/wall interaction are reviewed.

4.1 Phenomenology. One consideration for modeling droplet/wall interaction is the implication of three different phases: a liquid droplet impinges a solid substrate immersed into a gaseous environment (Fig. 5). One of the greatest challenges is to correctly predict the physics at the circumferential locations where the three phases are in contact, the contact line. At all locations along the contact line, the static state of the three-phase system is described by the Young equation

$$\gamma_{SL} + \gamma_{LG}\cos(\theta_C) = \gamma_{SG} \tag{22}$$

where γ_{SL}, γ_{LG}, and γ_{SG} are the solid/liquid, liquid/gas, and solid/gas interfacial energies, respectively. The contact angle θ_C is the angle between the tangent of the liquid/gas interface on the contact line and the solid (see Fig. 5). It depends on the interfacial energies and the geometrical state of the surface, which include sensitivity to the surface roughness. The liquid/gas interfacial energy γ_{LG} is characterized by the surface tension of the phase pair, which is usually easy to determine experimentally. The solid/liquid interfacial energy γ_{SL} depends on each surface energy and their interaction. With large surface energy (metal, glass) the liquid usually wets the solid and has a contact angle lower than 90 deg. Such surfaces are called hydrophilic surfaces. On the other hand, on solids of low surface energy (polycarbonates, polymers), the liquid tends to minimize its contact surface and leads to a contact angle larger than 90 deg. These are called hydrophobic surfaces. As the surface energy of a dry gas is usually negligible compared to the surface energy of a solid, the solid/gas interfacial energy γ_{SG} is assumed to be equal to the solid surface energy [150]. For dynamic systems, i.e., when the liquid is in motion, it is necessary to take into account the usual terms of the Navier–Stokes equations, such as pressure, inertia, and viscosity, to accurately predict the motion of the contact line. Moreover, when the solid is heated, the liquid can vaporize, which adds another degree-of-freedom. Also, in the case of continuous droplet impingement, for example, when a spray impinges a surface, a thin layer of liquid can already be present at the moment of the impact.

Hence, we separate the outcomes of a single droplet impact on a wall into three main categories. First, if the temperature of the wall is lower than the boiling temperature T_b of the liquid and if there is no liquid on the solid prior to the impact, we define this as an impact on a cold dry wall. Second, for a wall temperature lower than T_b and in the presence of a layer of liquid on the wall prior to the impact, we define this as an impact on a cold wet wall. Third, for a wall temperature larger than T_b, we define this as an impact on a hot wall. In order to illustrate all the subphenomena for these three impact regimes, we detail their typical sequence and describe each of the steps in the following.

4.1.1 Impact of a Single Droplet on a Cold Dry Wall. We consider here droplets of large Stokes number, i.e., with a velocity significantly different from the velocity of the surrounding gas. The relative velocity leads to the deformation of the droplet prior to the impact. The deformation depends mainly on the density and the viscosity of the liquid and gas, and the surface tension of the droplet. The shape of the droplet has a significant influence on the impact [154]. When the distance between the droplet and the wall tends to zero, a lubrication flow is established. This leads to a strong increase of the pressure (lubrication pressure) which deforms the droplet before it effectively touches the wall. An air pocket can be entrapped in this zone, leading to a bubble. This effect was originally observed by Refs. [155] and [156] on a solid surface and a liquid pool, respectively, and later extensively reviewed by Ref. [148]. When the velocity of the droplet is sufficiently low ($We < 4$) the droplet can even rebound on an air layer without effectively touching the substrate [157], even on hydrophilic surfaces [158].

Depending on the impact energy, several different scenarios are possible. These are illustrated in Fig. 6. For sessile droplets, i.e., droplets gently deposited on the surface (Fig. 6(*a*)), the droplet sticks to the surface with a contact angle θ_C lower (resp. larger) than 90 deg on hydrophilic (resp. Hydrophobic) surfaces. For low impact energy (Fig. 6(*b*)), as the droplet moves toward the wall, it constantly deforms and starts to spread on the substrate. Because this early phase of the impact is only determined by the kinematic conditions of the impact (droplet velocity and diameter) and is not affected by the mechanical properties of the liquid, it is called the *kinematic phase* [159]. During this phase, the spreading surface is roughly equal to the area of a slice of the droplet in a horizontal plane at the contact surface while the droplet is predominately moving in a direction normal to the impacted surface, i.e., before the droplet starts to spread radially.

Then comes the spreading phase, in which the liquid further spreads away from the impact zone, but now in the form of a thin film, called the lamella. The outermost part of the lamella is thicker than the rest of the thin film and constitutes the lamella rim. The dynamics of the lamella and the rim where originally investigated by Yarin and Weiss [160] and later by Roisman et al. [161]. Spreading is controlled by the mechanical properties of the liquid, the impact energy, and the wetting properties of the substrate such as the interfacial energy and the surface roughness. Within the spreading phase, there are different types of evolution.

First, we consider a rim free of instabilities for moderate impact energy and a relatively smooth surface (Fig. 6(*c*)). When the impact energy is dissipated, the rim can (i) further spread on the surface due to capillarity effects for hydrophilic surface, or (ii) shrink and reduce the spread surface, in what is called the receding phase. Extreme cases of the receding phase have been observed, in which the lamella retracts and reforms a spherical droplet and can even produce a partial or total rebound from hydrophobic surfaces [159,162]. Note also that during the receding phase, the liquid can fragment in what is called receding breakup.

With an additional increase in the impact energy, the surface of the rim can destabilize into digitations (fingering effect, Figs. 6(*c*), 6(*d*)) [163]. The formation of fingers further dissipates the impact energy. In turn, fingers can destabilize and produce droplets that stick to the surface. The fingering effect is typically the precursor of splashing.

For still larger impact energy, splashing occurs, which corresponds to the fragmentation of the incident droplet and the partial remission of secondary droplets, with a partial liquid deposition. Note that for an engineering-oriented model, splashing re-injects liquid into the cavity where the droplet comes from.

Splashing can be broken into several classes. First, the prompt splash is a disintegration within the first instants after impact (Fig. 6(*d*)). This regime is promoted by surface roughness over two different scales: small roughness amplitudes enhance lamella destabilization while large amplitudes drive the disintegration mechanism [163].

Finally, for much larger energies (Fig. 6(*e*)), the lamella detaches from the substrate and destabilizes in the ambient gas, leading to a so-called crown, which disintegrates into the fingers. It is called the corona splash, and it is also promoted by a hydrophilic surface. In this regime, the viscosity has a major influence on the outcome [164], as it avoids the detachment of lamella from

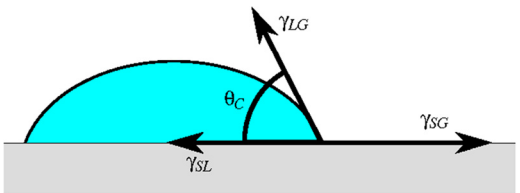

Fig. 5 Illustration of the contact angle θ_C and the interfacial forces at the contact line of a static droplet

the substrate. A decrease in the ambient pressure tends to suppress the formation of the crown [165].

4.1.2 Impact of a Single Droplet on a Cold Wet Wall. When a liquid film already covers the substrate prior to the impact, it adds another degree-of-freedom to the problem, and additional phenomena need to be considered. The characteristic parameter is the film thickness, usually given in a nondimensional form, as $\delta = h_f/D$. The ratio of film thickness to the roughness amplitude also influences the outcome [166]. For $\delta > 4$, the effect of the wall is not visible and the film is referred to as a deep pool [167]. By increasing the impact of energy, the succession of regimes is as follows [168]. At low impact energy, the droplet rebounds from the film. When the energy increases, the droplet is deposited and coalesces with the film. An upward jet can be observed for a sufficiently deep pool. For larger energy, a crater is formed on the surface of the liquid, which can lead to a dry patch for hydrophobic surfaces. The most visible effect is the onset of a crown of liquid with a vertical upward velocity, also known as a jetting flow, or symmetric uprising sheet. This crown then destabilizes in an azimuthal instability and fragments into secondary droplets. This type of splash on a dry surface is called a corona splash (Fig. 7). At an equal level of energy, a central uprising jet can be also observed.

4.1.3 Impact of a Single Droplet on a Hot Wall. When the solid substrate is heated, the temperature of the wall T_w adds another degree-of-freedom. Below the saturation temperature T_{sat}, no significant change of regime compared to the impact on a cold wall is observed, except the modifications of the liquid properties due to the change of temperature. Above T_{sat}, the wall is usually considered to be dry, as the liquid remaining from a previous impact is expected to have completely vaporized. When the temperature is between T_{sat} and the critical heat flux (CHF) temperature T_{CHF}, vaporization influences the outcome. In case of low impact energy, vaporization favors the droplet rebound. During the spreading phase, the liquid film enters a nucleate boiling regime. This leads to a mixed regime where the film breaks up due to the dry patches and due to a possible receding phase. For a high-impact energy, the droplet splashes in this regime are similar to those of the impact on a cold wall. At T_{CHF}, the heat flux from the substrate to the film is maximum. For a temperature between T_{CHF} and the Leidenfrost temperature T_L, the boiling regime evolves to a transition boiling. For $T \geq T_L$, the evaporation is so strong that it generates a cushion of vapor which insulates the liquid from the substrate. This is called the Leidenfrost regime. In this regime, the droplet rebounds and stabilizes onto the vapor cushion (Leidenfrost droplets) for low impact energy. For moderate impact energy, the droplet rebounds and boils at the same time, leading to the regime of explosive detachment and reflection rebound. For larger energy, the explosive rebound occurs with tiny secondary droplets that are ejected upward [169]. For even larger impact energy, the droplet splashes. At these high temperatures, radiative heat transfer should be considered [147].

The duration for complete evaporation of a drop (the evaporation time) is representative of the strength of the heat transfer process. It is a nonmonotonic function of the wall temperature (Fig. 8) where the local minimum and local maximum depict the CHF and the Leidenfrost point, respectively. T_{CHF} is reported to be insensitive to impact conditions whereas T_L varies with the impacting droplet diameter and velocity (magnitude and impact angle) and surface roughness. The droplet diameter is reported to have negligible effects on T_L [170] while some other authors [171] observe an increase of T_L with drop size. Depending on its magnitude, the impact velocity decreases [172] or increases [173] T_L.

4.1.4 Non-Newtonian Effects. When the impinging liquid has Non-Newtonian rheological properties, most of the studies in the literature focus on the spreading phase [174–176] or on antirebound properties [177,178] for impacts on a dry cold wall. Indeed, the addition of a polymer to a Newtonian liquid can drastically reduce the occurrence of rebound on a hydrophobic surface and modify the dynamics of the contact line [175], which is a competition between surface tension and normal stress inside the liquid. Also, droplets of shear-thinning liquids have been studied [176] and shown to exhibit different receding motions than droplets of a Newtonian liquid.

4.1.5 Impact of a Real Spray, Droplet/Droplet Interaction. When a real spray impacts a wall, the mechanisms involved are a combination of isolated droplet/wall and droplet/droplet interactions. One difficulty when describing spray/wall interaction is that no superposition principle can be applied to the spray droplets. Nonlinearities brought to the spray/wall impact by drop/drop interaction prior to the impact [179], during the impact (lamellas interaction leading to uprising jets, asymmetric corona splash [161]), and after the impact (secondary droplets coalescence) increase the complexity of the process.

Additional droplet-droplet parameters are derived to characterize the spray regime. These are the length between two droplets at their impact location l_{spacing} and the normalizing time scale between two consecutive droplets τ_{ci}. A phase parameter $\phi = 2\pi\tau_{ci}$ determines if two consecutive droplets impact the wall at the same time ($\phi = 0\,\text{deg}$) [180] or one after each other ($\phi = 180\,\text{deg}$) [160]. For $l_{\text{spacing}} > 0$, two spreading lamella may interact, even though it was observed that for $l_{\text{spacing}} < 2D_0$ the crown formation was inhibited. For $l_{\text{spacing}} < D_0$, the two droplets would coalesce [181]. Interested readers are referred to [182].

Macroscopic models are used to recover the global spray/wall interaction. The main values of interest are the deposited mass, secondary drop size distribution, and the extracted heat from the

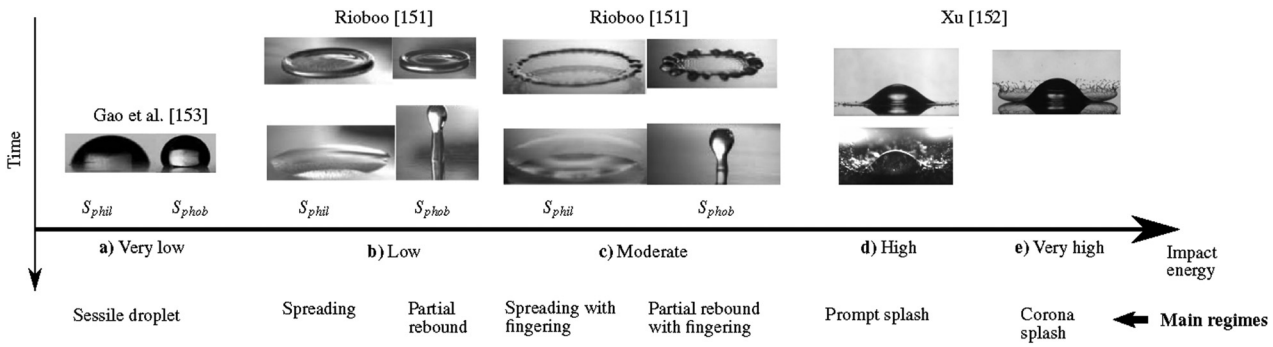

Fig. 6 Overview of the different outcomes of droplet impacting a cold dry wall, depending on the impact energy, from [151–153]. Reprinted figures from Xu, L., *Physical Review E*, 75(5) p. 056316, 2007. Copyright 2007 by the American Physical Society, and from *International Communications in Heat and Mass Transfer*, 88, Gao M., Kong P., Zhang L.-X and Liu J.-N., pp. 262–268 Copyright 2007, with permission from Elsevier. S_{phil} and S_{phob} refer to a hydrophilic and hydrophobic surface, respectively.

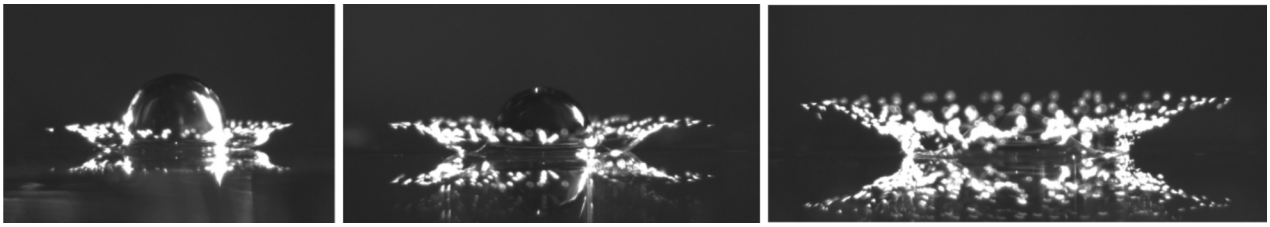

Fig. 7 Early phase of the corona breakup, from [151]

surface in the case of hot wall impacts. Correlations on these are given in the next sections.

4.1.6 Impact Regimes of CMAS Particulates in Engine-Like Conditions. Due to the extreme conditions of pressure, temperature, and space constraints, it is extremely difficult to obtain experimental visualizations of CMAS particulate impacts in engine-like conditions. Prior to the combustion chamber, particulates are too cold to behave like liquid so that droplet-like impact regimes of CMAS can be considered only for molten sand in the combustion chamber and in the turbine. According to Table 3, for particulates between 3 and 30 μm, the Weber number is between 300 and 3000 and 3000 and 30000 in the combustor and turbine, respectively, which corresponds to very high impact energy and should lead to corona splash, as depicted in Fig. 6.

However, recent numerical simulations [183] showed that a molten sand particle smoothly deforms during impact, barely spread and does not splash at all, which corresponds to Fig. 6(*a*). The reason for this discrepancy is the extremely high viscosity of molten sand ($\sim$5Pas) which leads to a very large Ohnesorge number (Oh $\sim$ 30) compared to the usual experimental conditions with water or oil droplet impact (Oh $\sim$ 0.1).

The physics of a droplet impact characterized by very large Weber and Ohnesorge numbers is that inertia overpowers surface tension (large We) and that viscosity overpowers inertia and surface tension. Since these conditions are very rarely met, the literature is rather scarce on this topic, and to the authors' knowledge, no experimental observations of impacts for droplets with high Weber and high Ohnesorge number have been published. Concerning heat transfers, since the boiling point of sand (2500 K) is far above the typical wall temperature of combustor tiles and turbine blades, the impact regime can be always considered as on a dry cold wall.

4.2 Direct Numerical Simulation of Droplet/Wall Interaction. The main objective of the DNS of droplet/wall interactions is to obtain detailed insights into the physics of droplet impact. Thus, DNS is regarded as a numerical experiment. In this case, the computational domain is limited to the close vicinity of the impact. The dynamics of the liquid phase are captured by the high-resolution solution of the Navier–Stokes equations and the kinematics of the interface are described by interface capturing methods.

One of the greatest challenges in such direct numerical simulations is to predict correctly the moving contact line [184], which upon the assumption of nonslip condition at the wall leads to a divergence of the stress, and needs to be relaxed by a slip velocity [185]. Moreover, the effect of the surface tension between the liquid, the gas, and the substrate must be accounted for. These aspects are governed by the balance of forces at the contact line. This requires that either the advancing/receding contact angles or the interfacial energies of each pair of phases are known. The determination of both of these is experimentally cumbersome. The surface roughness, which is of very small amplitude, is also computationally expensive to resolve as it is necessary to decrease the space resolution.

The two most popular approaches are the volume of fluid (VOF) and the Level-Set (LS) methods. In the VOF approach, the Navier–Stokes equations are solved for a single-phase whose mechanical properties are a blend of the two phases based on the volume fraction α_V of the liquid. The volume fraction is then computed by a transport equation of α_V. This approach has shown good qualitative agreement with experiments for the spreading regime [186,187]. The VOF method can capture air entrapment [188] and the dynamic contact angle [189,190], and can be applied to liquid films [191] or deeper pool [192] impingements. Also, the force generated on the wall by droplet impact has been studied [193], as has heat transfer, vaporization, and boiling [194]. The main advantage of this method are that it inherently conserves mass, whereas its main drawback is that the interface is not explicitly computed. This is particularly detrimental for physics related to the interface, which is the case for the surface tension effects. Therefore the interface must be reconstructed based on the distribution of α_V, which leads to additional computation costs [195].

In the LS approach, the interface is explicitly resolved by a transport equation of a signed-distance function ϕ to the interface, which allows for accurate capture of interfacial effects. This approach was originally developed by Sethian [196] and adapted to ensure mass conservation with a moving contact line by Spelt [197]. The LS has been used to investigate the impact of a liquid droplet on a solid cold wall [198–201] and a liquid film [202]. Additionally, heat transfer was predicted [203–208] in which boiling and/or vaporization were taken into account.

The VOF and LS methods can be coupled to profit from the advantages of both methods, with what is referred to as CLSVOF [209]. This has successfully been applied to impacts on solid walls [199] and on liquid film [210], with heat transfer [211–213].

In the last two decades, three new approaches have been adapted to multiphase flows and successfully applied to droplet/wall impact. First, is the Lattice-Boltzmann Method (LBM, described in Sec. 3.2.3), in which the multiphase flows are taken into account by several strategies [214–216]. As with the aforementioned approaches, LBM originally shows numerical

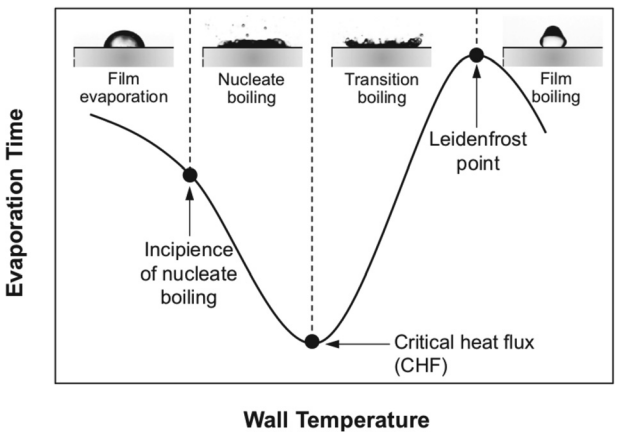

Fig. 8 Evaporation time versus the wall temperature, from [149]. Reprinted from *International Journal of Heat and Mass Transfer*, 106, Liang G., Mudawar I., pp. 103–126 Copyright 2007, with permission from Elsevier.

instabilities in case of large density or viscosity ratios [217], but a new approach has shown promising results for a density ratio of up to 1000 [218]. Note that according to Tables 1 and 2, a density ratio of 1000 is sufficient to simulate CMAS particulates in all the components of the gas turbine, except for the first stages of the compressor where the gas density is too low. As it is a diffuse interface approach, this method is not subject to a singularity due to the moving contact line. Impacts on a drywall [219–224] as well as on a liquid film [225] have been investigated. Heat transfer as droplets impacts a solid surface has also been studied [226].

The second approach, the smoothed particle hydrodynamics (SPH) method, is a meshless approach where the discretizing elements (referred to as particles) are points moving at the fluid velocity [227]. Each element carries its physical quantities (mass, volume, energy). In this case, the motion of the particles is determined by solving the Navier–Stokes equations for each particle in its Lagrangian frame of reference. In order to simulate multiphase flows, each particle is given a specific type of fluid (e.g., liquid or gas) and the corresponding mechanical properties. These properties are maintained throughout the simulation. The particles rearrange themselves according to the physics resolved by the Navier–Stokes equations. The interface is implicitly determined as the frontier between ensembles of particles of a different types. The most popular approach for including surface tension is an adaptation of the Continuum Surface Force model [228] in the SPH formulation [229]. The advantage of the SPH method is that no meshing step is required, and it can simulate large interface deformations without a priori knowledge of the deformations. Also, when the influence of the carrier gas is negligible, only the liquid and walls need to be simulated to study droplet/wall impacts. One of the limitations of this method is that the interparticle distance must be kept constant in order to achieve a high computing performance. This is equivalent to performing a simulation with a homogeneous mesh.

It is possible to implement this approach and allow for varying particle distances, but this leads to a more complicated implementation of the method [230]. Moreover, as a Lagrangian method, it is subject to specific types of instabilities (tensile and pairing instabilities) which require stabilization terms that can alter the physics. Because it does not require any mesh, this method is convenient for resolving the surface roughness. To this aim, the spreading of a sessile droplet was investigated by Li et al. [231] and by Shigorina and Tartakovsky [232] on porous and rough surfaces, respectively. Concerning liquid film impingement, Xu et al. [233] studied the interaction of two droplets in parallel and in series, and the effect of the film thickness has been investigated by Ma et al. [234] and by Yang et al. [235]. The shape and outcomes of the impinging droplet were investigated by Yang and Kong [236] and Ray et al. [237]. Yang et al. [238] studied the influence of the wall temperature where the liquid vaporization was taken into account. The SPH method has also been employed to study viscoelastic effects, examining two-dimensional droplets impacting an inclined plate [239], and symmetric droplet impacts in three-dimensional [240]. Recently, the high-velocity impact of molten sand particulates having spherical and cubic shapes was investigated with the SPH method [183].

Finally, the third approach is the phase-field approach, which belongs to the interface-capturing family of VOF and LS methods, where the indicator of the phase interface ϕ (as in the LS method) is computed by a transport equation incorporating physical effects at the thin interface [241]. In this approach, the indicator ϕ is attributed physical properties, such as those derived from gradient flows of the Ginzburg-Landau-Wilson free energy functional, which offer interesting properties for two-phase flow modeling. Ding et al. [242] proposed an approach to use the phase-field method in two-phase flow of large density and viscosity ratio, illustrated by the simulation of rising bubbles and Rayleigh-Taylor instability. Mirjalili et al. [243] showed that VOF outperforms phase field methods at the same resolution, but for the same computational cost, and both methods have comparable accuracy. Very recently Mirjalili and Mani [244] proposed a consistent and energy-conserving momentum transport and a promising free-energy surface tension force scheme. The three-dimensional impact of a liquid droplet on a solid surface was simulated with the phase-field method by Zhang et al. [245], and additional solidification during the impact was taken into account by Shen et al. [246].

4.3 Lower-Order Models. The objectives of using lower-order models are to model the outcome of droplet/wall interactions without a strong focus on the phenomenon itself, but rather to facilitate having the outcome of the phenomenon embedded into a larger simulation involving a cascade of physical phenomena including droplet/wall interactions. A typical example is the case of a spray flame in a combustion chamber or a piston engine, which requires that a large spectrum of physics, such as atomization, turbulence, phase change, thermal transfers, chemistry, and combustion, be taken into account. In this case, the liquid droplets of the fuel spray may impact the piston as well as the walls of the cylinder and may create a liquid film. Due to the different length scales, which range from a few micrometers (smallest droplets) to dozens of centimeters (diameter of the cylinder for a regular car engine), the DNS of this configuration is prohibitive for current-day supercomputer capabilities. Hence, the droplet/wall interaction must be modeled.

4.3.1 State of the Art. The typical approach is an Euler/Lagrangian simulation where the carrier phase and the droplets are represented by an Eulerian field and Lagrangian particles, respectively. When a particle impacts the wall, the outcome is given based on ad hoc models or correlations presented later. Depending on the conditions of the impacting droplet (kinetic energy, viscosity) and on the local surface state (temperature, presence of liquid film, roughness), the ad hoc model will predict different outcomes. These are mainly rebound (only the particle velocity is modified), splashing (new particles are created), and spreading. In the later case, a thin liquid film is formed and needs to be modeled. Very often, the film is thin enough that its attributes can be averaged over its height, leading to a two-dimensional model. It can be described by either Lagrangian or Eulerian approaches. In the former, the film is described by film particles that carry the conservative quantities, while in the latter, additional local wall variables are used to store the characteristic quantities of the film. In both cases, a specific wall film solver is required. Such models are typically used in internal combustion engines where the spray is treated as Lagrangian particles and the film is either Eulerian [247–249] or Lagrangian [179,250–253]. Depending on their level of sophistication, these models account for phenomena related to mass conservation (boiling, droplet impact, film striping), momentum conservation (inertia, transfer with gas, and impacting droplets), and energy conservation (heat transfer, boiling). Wall film and splashing low order models have also been applied to gas turbine configurations [254]. From a numerical point of view, it is important to take into account that in a Lagrangian framework, one parcel (i.e., a numerical particle) is representative of a large number N_p of physical droplets sharing the same properties. This is done to limit computational overhead, which would be prohibitive if all droplets were represented individually. On the other hand, if N_p is too large, then the simulation would be made of very few parcels, and the dispersion of the spray properties (mainly size and velocity) would be under-resolved. Hence, N_p must be chosen to reach a tradeoff between computational cost and statistical resolution of the spray and its outcome after impingement. Note that due to the discrete nature of the wall splashing, an approach based on an Euler description of the liquid phase is tedious. Nevertheless, such attempts are found in the context of wing impingement by subcooled droplets [255–257]. Note that in principle, the same approach could be used to investigate impacts of subcooled droplets on rotating fan blades.

4.3.2 Regime Maps. In order to rationalize the outcome of droplet/wall interactions, regime maps are drawn based on the impact energy, the wall temperature, and the film thickness, with threshold values used to set the limit between different outcomes. The most complete regime map, shown in Fig. 9, is from work by Ma et al. [253]. The different regimes described in Sec. 4.1 are represented. The main parameters are the impact energy (y-axis) and the wall temperature (x-axis). (In this figure the Leidenfrost temperature T_L is given as T_{leid} and nondimensional wall film depth δ is given as H^*). On the right part of the regime map, where the regimes related to wet surfaces are depicted, the film thickness is used instead of the surface temperature for the x-axis. The threshold criteria between regimes are expressed in terms of correlations depending on droplet properties and the state of the surface. There is strong consensus for some of the thresholds, while both the values and expressions of others remain the subject of much debate. Here, we review the most used/agreed-upon thresholds.

In the dry case, at $T_w < T_{\text{sat}}$, the limit between stick and spread is usually found around We = 5 [248,253]. From an engineering perspective, the separation between spread and splash (K_1) is the most important and consequently, it was thoroughly investigated. Its main correlations are given in Table 4, where R^* refers to the nondimensional roughness (R_a/D_p). As mentioned, there are several different expressions of this threshold.

The threshold K_2 is found when the value of the Ohnesorge number is constant and equal to 0.00446 [253] whereas other authors stated it depends on the ambient pressure and surface roughness [152]. This question is thoroughly treated in Ref. [148]. For impacts of hot surfaces ($T_w > T_{\text{sat}}$), the map from [253] (Fig. 9) assumed a threshold between spread and splash as independent of temperature. However, a more sophisticated threshold depending on temperature is proposed by Staat et al. [260], as depicted in Fig. 10. It can be approximated as

$$K_1 = We = f_1(T_w) \quad \text{for} \quad T_w < T_{\text{leid}} \tag{23a}$$

$$K_3 = We = f_2(T_w) \quad \text{for} \quad T_w > T_{leid} \tag{23b}$$

where f_1 and f_2 are arbitrary functions. Note that the value of $K_3(T_w > T_L)$ still varies significantly depending on authors, as illustrated in Table 5.

On a wet wall, the nondimensional liquid film thickness $\delta = hf/D$ is substituted for the surface temperature as a driving parameter. The rebound/deposition threshold was investigated by Pan et al. [264] and is summarized in Table 6.

There is a continuous transition between the regimes of deposition and corona splash, where more and more droplets are ejected when the Weber number increases. Hence, the threshold K_5 shows large variability in terms of values and expressions (Table 7), which can be explained by the dependence of K_5 on the film thickness [262]. Some authors [253] also define a threshold (K_4=1400) to mark the beginning of the smooth transition.

4.3.3 Correlations based on Spreading. The maximum spread quantifies the contact surface between the substrate and the impacting liquid. When a chemical reaction between the two phases is expected, the spread is of primary importance because it determines the progress of the chemical reaction occurring between the impacting matter and the substrate. It has been investigated in the literature experimentally and theoretically, based on energy or momentum conservation. An extensive list is provided in Ref. [149]. The main correlations are given in Table 8 for a cold dry wall where the maximum spread $\beta_{\max}$ is expressed in the nondimensional form normalized by the impacting droplet diameter. Note that some correlations provide an implicit definitions of $\beta_{\max}$.

4.3.4 Correlations based on Rebound and Splashing. During the rebound, only the velocity is modified. The simplest approach assumes an elastic rebound which consists of changing the sign of the wall-normal component and conserving the tangential component. Some authors take the dissipation of the kinetic energy into account by introducing a restitution factor which depends on the Weber number [261]. The outcome of splashing is more complex. It is described by the number, the velocity, and the size of the ejected droplets. An extensive list of correlations from [161,179,248,249,272–275] is provided in the review by Moreira et al.

Hence, the focus given here is on the input and output parameters. These models are usually built on fundamental conservation laws. Mass is conserved, momentum is dissipated due to viscous effects, and energy is modified to take into account the change of surface energy during breakup or heat transfer. Most of these models predict the outcome in terms of attributes following density of probabilities with coefficients that depend on the impact conditions. In this case, it is possible to obtain an acceptable statistical representation of the splashing, providing a small parcel number N_p. All of these models take as input the properties of the impacting droplet, plus (i) the surface roughness [274] in case of dry impact, and (ii) the film thickness [273,274] in case of wet the surface. The velocity of secondary droplets is determined from hybrid models based on momentum conservation and empirical constants related to the restitution coefficient. The typical geometrical basis used to express the outcome velocity consists of the wall-normal, the tangential, and the transverse component [252]. Some authors also use random sample attributes drawn from within a cone [248] or within an empirical reflection angle [249]. The diameter of secondary droplets is expressed with a probability density function whose mean diameter and dispersion factor are computed based on empirical or semi-empirical correlations. The number of droplets is usually chosen after the other quantities so that the mass is conserved during the impact.

4.3.5 Correlations Based on Mass Deposited After Splashing. As an extensive list of correlations of mass deposited after splashing can be found in Ref. [147], we focus here on the type of input parameters. First, the correlations depend on the impacting energy [275]. Then, depending on whether the substrate is dry [258] or wet [179,249,273,274,276,277], the roughness or the film thickness are taken into account, respectively. In case of hot surfaces, the temperature can be taken into account [276].

4.3.6 Correlations Based on Heat Transfer. From a macroscopic point of view, energy conservation leads to the global heating of re-emitted droplets, based on knowing the heat is extracted from the surface and the evaporation rate. In order to quantify the heat extracted from the wall and transferred to the secondary

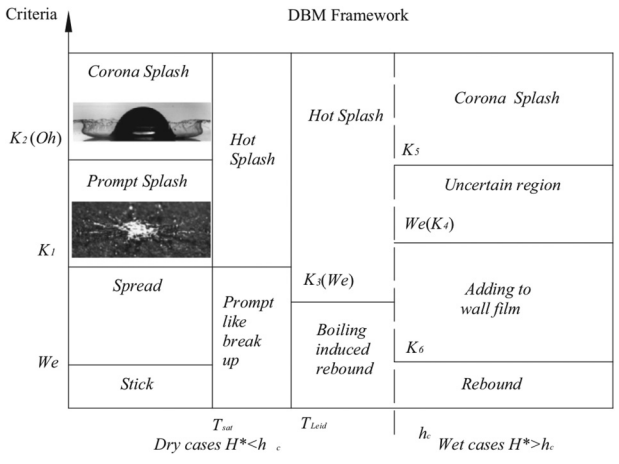

Fig. 9 Regime map for droplet-based wall impingement models from Ref. [253]. Reprinted from *International Journal of Heat and Mass Transfer*, 112, Ma T., Feng L., Wang H., Liu H. and Yao M., pp. 401–412 Copyright 2017, with permission from Elsevier.

Table 4 Criterion for splashing on a dry surface

Expression	Threshold	References
$K_1 = \mathrm{We}^{5/8}\,\mathrm{Oh}^{-1/4}$	57.7	[258]
$K_1 = \mathrm{We}\,\mathrm{Oh}^{-2/5}$	$649 + 3.76/R^{*0.63}$	[168]
$K_1 = \mathrm{We}\,\mathrm{Oh}^{-2/5}$	3000	[259]
$K_1 = \mathrm{We}^{5/4}\,\mathrm{Oh}^{-1/2}$	$1500 + 650/R^{*0.42}$	[179]
$K_1 = \mathrm{OhRe}$	17	[234]

Table 5 Criterion for splashing on a dry hot surface

$K_3 = \mathrm{We}$	References
$K_3 = 30$	[261]
$K_3 \approx 23$–40	[262]
$K_3 \approx 14$	[263]
$K_3 < 10$	[169]

droplets, a correlation for the Nusselt number is given. The generic form of the Nusselt correlation found in Ref. [147] is

$$\mathrm{Nu} = a\,\mathrm{Pr}^b\,\mathrm{Re}^c\,\mathrm{We}^d\,\mathrm{Ja}^e \tag{24}$$

where Pr and Ja are the Prandtl and Jakob numbers. Table 9 summarizes the constants derived from various experiments. Note that these correlations were derived in the case of a complete spray impacting a wall, not in a single droplet/wall interaction.

5 Particle Deposition at Gas Turbine Operating Conditions

Ingestion of sand and dust particles by gas turbine engines and particle deposition in the hot sections of the engine is a critical issue [282–284]. At high operating temperatures, inertial impaction of ingested particulates leads to melting of the particles with their deposition on blade surfaces as well as blade surface erosion and corrosion. Large amounts of melted deposits lead not only to structural blade damage [16,285] (Fig. 4(*a*)) but also to degradation of the flow path (Fig. 4(*b*)) and aerodynamic performance and to blockage of the turbine blade cooling holes [13] (Fig. 4(*c*)). As a result, aircraft engines operating in dusty environments may be vulnerable to significant loss of operability.

Table 6 Criterion for rebound/deposition on wet surface, derived from [264]

δ	$K_6 = \mathrm{We}$
< 0.5	$15\delta - 3$
0.5–0.8	15
0.8–1.2	$15\delta - 3$
> 1.2	15

Table 7 Criterion for splashing on a wet surface

δ	K_5	References
–	$2100 + 5880\,\delta^{1.44}$	[168]
–	$K_1 \cdot [1 + 0.1\sqrt{\mathrm{Re}} \cdot \min(\delta, 0.5)]$	[179]
<0.1	450	[262]
$0.1<\delta<1$	$1043.8 + 232.6\delta^{-1}$	
$\delta > 1$	$1043.8 + 232.6\delta^{-1}$ $-1094.4\delta^{-2} + 1576.6\delta^{-3}$	

Table 8 Correlations on maximum spread from the literature

Expression	References
$(3\beta_{\max}^2/\mathrm{We}) + (\beta_{\max}/1.2941)^5/\mathrm{Re} = 1$	[265][a]
$\mathrm{We}/2 = 1.5\beta_{\max}^2[1 + 3\mathrm{We}/\mathrm{Re}(\beta_{\max}^2 \ln\beta_{\max} - (\beta_{\max}^2 - 1)/2)$ $(\mu_d/\mu_w)^{0.14}] - 6$	[266][a]
$\beta_{\max} = \sqrt{(\mathrm{We} + 12)/(3(1 - \cos\theta_a) + 4(\mathrm{We}/\sqrt{\mathrm{Re}}))}$	[267][a]
$(We + 12)\beta_{\max} = 8 + \beta_{\max}^3[4\mathrm{We}/\sqrt{Re} + 3(1 - \cos\theta_d)]$	[268][b]
$\beta_{\max} = (0.87\mathrm{Re}^{0.2} - 0.4\mathrm{Re}^{0.4}/\sqrt{\mathrm{We}})$	[269][c]
$\beta_{\max} = 0.61(\mathrm{Re}^2\mathrm{Oh})^{0.166}$	[270][c]
$\beta_{\max} = 1.27(\mathrm{Re}^2\mathrm{Oh})^{0.122}(\sigma_{\mathrm{iso}}/\sigma_x\,\mu_{\mathrm{iso}}/\mu_x)^{0.11}$	[271][c]

Superscripts[a,b] and [c] correspond to a correlation based on energy balance, momentum balance, and regression, respectively.

5.1 Deposition Models. The interaction of particles with surfaces is accompanied by a range of physical processes that determine the outcome of the interaction. As a particle hits the surface, it can experience electrostatic and fluid dynamic forces. The outcome may be rebound, deposition, or partial adhesion of the particle, and typically involves elastic and/or plastic particle deformations. In addition, if the particle is molten or semimolten, viscous deformation will also occur. One needs to account for viscous and thermal boundary layer effects near the surface to properly determine particle properties right before particle-surface collisions occur. The coefficient of restitution (Eq. (1)) is a suitable parameter to quantify the energy exchange between a particle and the surface. A number of empirical and physics-based models can be found in the literature that can be used to augment this coefficient for study the problem of particle-surface interaction occurring under many different conditions. Recently, in Ref. [286] the authors showed the effect of varying Stokes number on the impact of millions of CMAS particulates on turbine blade at transonic conditions. Physics-based models rely on material properties and have relatively broad applicability to different problem types. However, most of these models require underlying geometrical assumptions to simplify computations. Empirical models on the other hand provide a direct formulation for rebound/deposition characteristics and are easier to integrate with any stochastic approach. The accuracy of an empirical model, however, is limited to the configuration/data it is derived from. The early models developed by Hamed et al. [287,288] are the classic example of

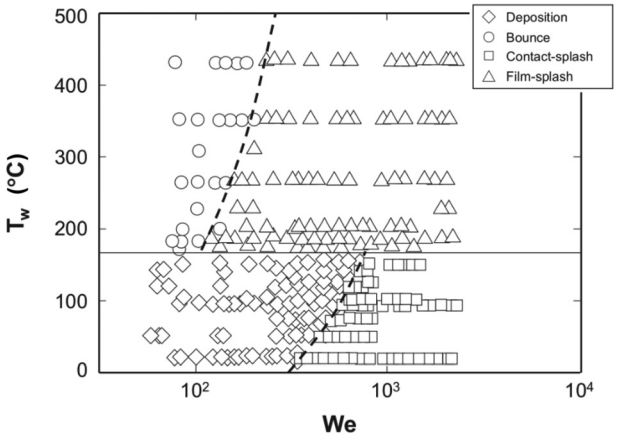

Fig. 10 Detail regime map of droplet of ethanol impacting a hot dry surface, adapted from [149]. Reprinted from *International Journal of Heat and Mass Transfer*, 106, Liang G., Mudawar I., pp. 103–126 Copyright 2007, with permission from Elsevier.

empirical models designed for specific turbomachinery applications. Some of the pertinent models are discussed next, with the goal of focusing on understanding particle deposition behavior under hot temperature conditions like those in high-pressure gas turbine engines.

5.1.1 Critical Velocity Model. The critical velocity model was developed by Brach and Dunn [289]. It defines a critical impact velocity below which the kinetic energy of the incoming particle is too low to overcome the adhesion bond resulting in a particle sticking to a surface with no restitution. The critical velocity criteria perform reasonably well at low-velocity impacts where adhesion forces dominate energy exchange mechanisms. The criteria however do not predict accurate particle behavior for high-velocity impacts [290]. Brach and Dunn [289] computed the critical velocity using the relation

$$V_c = \left(\frac{2E_{\text{eff}}}{\phi}\right)^{\frac{10}{7}} \tag{25}$$

where E_{eff} is the combined elastic modulus derived from the elastic properties of both particle and the surface. ϕ is the diameter of the particle under the assumption that the particles are spherical in shape. Critical velocity models suitable for high-temperature deposition in gas turbine engines are also available in the literature [291,292].

5.1.2 High-Temperature Critical Viscosity Model. A probabilistic critical viscosity model developed by Sreedharan and Tafti [293] can be used to identify stochastic deposition criteria for particles in high-temperature conditions. The model defines a threshold temperature and any interacting particle with a temperature above the threshold temperature will stick to the surface. When the temperature of the particle is below the threshold temperature, the stick probability is given by

$$P_{\text{stick}} = \frac{\mu_{\text{threshold}}}{\mu_T} \tag{26}$$

where $\mu_{\text{threshold}}$ is the viscosity of the particle at the threshold temperature and μ_T is the viscosity of the particle at the given temperature. The stick probability is governed entirely by the temperature-dependent behavior of the particle viscosity. For CMAS-constituted particles, there are a number of empirical composition-based formulas available in the literature [294–296] that provide a good estimate of viscosity as a function of temperature. Similar studies for feldspar melts [297] and coal ash [298] can also be found in the literature. Most of these studies have found the following relationship between temperature and viscosity

$$\log\left(\frac{\mu_T}{T}\right) = A + \frac{B}{T} \tag{27}$$

where A and B are empirical constants that are dependent on particle composition. This model is limited in its application because it does not account for key parameters such as particle impact velocity, size, and shape while determining the criteria for sticking. Also the model does not provide any information on particle rebound and deformation properties. Singh and Tafti [299] developed a variant of this model which accounts for additional physics by including the coefficient of restitution in the calculation of sticking probability. This contribution to sticking probability is given by

$$P_c = e^{-6.5c} \tag{28}$$

where they define c as the total coefficient of restitution determined using a separate physics-based model.

5.1.3 Elastic Plastic Deformation Model. This model was proposed by Singh and Tafti [300] and it can be used to compute the coefficient of restitution by using particle material properties and a combined elastic modulus. The model assumes that the particle is spherical in shape and is pressed into a flat plate. The first step of the model is to determine the distance w into the plate that the sphere must be pressed to exceed the particle elastic deformation limit and cause the onset of plastic deformation [301]

$$w = \left(\frac{\pi C\sigma}{2E_{\text{eff}}}\right)^2 r_p \tag{29}$$

$$C = 1.295e^{0.736\nu_p} \tag{30}$$

where w is the particle deflection at the onset of plastic deformation, σ is the particle elastic yield strength and r_p is the radius of the particle. An energy balance is then used to obtain maximum deflection during deformation. The two deflection parameters and a separate formulation for adhesion are then used to compute the coefficient of restitution. The main challenge lies in the determination of model parameters for application to gas turbine engines considering the complexities due to the size and chemical composition of particulate matter in the hot gas mixture. The particles are also not necessarily spherical in shape [302]. Under this model, the criteria for sticking is determined stochastically in a manner similar to the critical velocity model with some degree of randomization. To predict whether the particle will stick or not, the sticking probability is defined such that it increases exponentially with a decrease in coefficient of restitution value. The sticking probability becomes unity when the coefficient of restitution becomes zero. A revised version of this model can be found in Ref. [303]. More recently, Bons et al. [304] developed a variant of this model with the assumption that particles are cylindrical in shape that takes into account angular and fluid shear effects.

5.1.4 Rebounding-Sticking Model. This composite model is extended from the stochastic empirical model by Hamed et al. [287,288] to include additional physics pertaining to high-temperature deposition. The model accounts for particle temperature, size, and the impact angle to determine the behavior of particles upon impact. This model first determines sticking probability by constructing detailed polynomial functions based on particle size, temperature, and normal and tangential velocity. The constants in the polynomial functions are determined through separate numerical simulations. More details about the sticking probability calculations can be found in Barker et al. [305]. Once it is determined that the particle will rebound, the model determines the rebounding characteristics using a separate set of formulations.

Table 9 Nusselt number correlation coefficients

a	b	c	d	e	References
2	0	0	0	0	[278]
3.32	0.33	0	0	0	[278]
4.7	0.32	0.61	0	0	[279]
0.34	−0.33	−0.53	0.94	0	[280]
$3.4\ 10^{-5}$	0	1.51	0	0.254	[281]

5.2 Particle and Surface Characterization. To determine the properties of ingested sand at engine operating conditions and predict particulate behavior on interaction within hot sections of the engine, it is important to understand the sand composition. The ingested particulate matter is comprised of metal oxides and mineral compounds. Depending on the operating environment, the following key dust types have been identified in the literature and their composition determined: volcanic ash [306,307], coal ash

[302], and Arizona road dust [308]. A comprehensive technical report on characterization of CMAS airborne particulates [309] provides extensive experimental data on particle composition, size, and morphology. This report includes a chapter on X-ray diffraction (XRD) analysis for determining particle hardness and melting point to aid in evaluating erosive potential and deposition potential. Typically, Arizona road dust and a synthetic sand equivalent AFRL02 are used in experiments to simulate the behavior of natural sand. The temperature can reach up to 1650 °C in the engine combustor and up to 1450 °C in the initial high-pressure turbine stage creating a strongly energetic and reactive hot gas mixture. At these temperatures, the ingested particulates melt and form CMAS compounds that deposit on the hot components [27,310]. The reactive CMAS mixture is highly detrimental to the blade components. TBCs are applied to blades to protect them in the hot gas path. These coatings are designed to have high in-plane compliance to reduce thermal stresses and low thermal conductivity to reduce heat transfer to the blades. Considerable research has been put into the development of TBC materials and their composition is known. TBCs developed from Yttria stabilized zirconia [26,311,312] are state-of-the-art and best known for their thermal properties. Nonetheless, molten CMAS can penetrate into the cooler region of the coating and crystallize to alter the desirable properties of the coating. The composition of CMAS is well understood [313] and thereby multiple synthetic compositions are available [26] for use in experiments with desired crystallization properties.

5.2.1 Temperature-Dependent Properties. The accuracy of physics-based models depends strongly on the accuracy of properties used in the models for the surface and the particles interacting with it. The surface properties used are for the thermal barrier coatings used to protect the blade material. Considerable research has gone into the development of these thermal barrier coatings and their mechanical properties are well known under a wide range of operating temperatures. However, the determination of the mechanical properties of ingested particle mixtures is nontrivial. To reproduce the austere environmental conditions for the engines under laboratory settings, synthetic dust equivalents are used. The components that make up synthetic sand are derived from equivalent dust/sand samples and are mainly comprised of metal oxides and other mineral compounds [314–317]. The bulk properties of the synthetic sand can be obtained through a suitably weighted summation of the individual constituent properties. This is an apt approach at low temperatures when the components exist in a solid-state with defined mechanical properties. At high temperature, the components start to form molten CMAS and interact with turbine coating surface. Availability of the mechanical properties of these metal oxides in the temperature range of interest is limited. The properties of selected components such as quartz can be found in Ref. [318,319]. They recorded the variation in density, Poisson ratio, and elastic modulus in the temperature range of 20 °C to 1050 °C. Similarly, properties of Halite (sodium chloride or rock salt) are available from selected studies [320–322].

5.3 Available Experimental Data. Different aspects of the problem of sand ingestion have been investigated through experimental studies with many complemented by parallel numerical investigation. For example, Singh et al. [323] conducted experiments to investigate the impingement behavior of sand-laden flow through a two-pass cooling duct with ribs present. In their experiment, they used a particle composition equivalent to Arizona road dust and fed the entrained flow to the duct to obtain the impingement pattern on surfaces covered with an adhesive used to provide a perfectly inelastic surface. The authors then conducted a numerical simulation on the same duct domain for a comparative evaluation. They utilized wall-modeled large eddy simulation for the fluid field and Lagrangian tracking for the suspended particles with one-way coupling between the phases. Good agreement between experimental and numerical impingement patterns was obtained which helped them understand the particle flow paths accurately and identify higher impingement-prone surfaces within the duct. The survey conducted by Singh et al. [323] outlines a number of experimental studies capable of characterizing the problem of sand ingestion and potentially aiding in developing physics-based deposition/erosion models to predict behavior and losses pertaining to particle-wall interaction. The review conducted by Hamed et al. [13] is another thorough compilation of the studies covering important aspects of particle-induced erosion and deposition. Their review cites studies that have attempted to determine the pattern of erosion, identify components most susceptible to erosion, and investigate multiple factors affecting both the rate and extent of erosion. A detailed list of erosion studies utilizing different blade/coating materials and various impact parameters is also included. Their review includes numerical studies that have simulated particle trajectories to predict deposition characteristics based on empirical correlations and stochastic data. The development process of particle delivery models and deposition models has been summarized alongside a discussion of particle delivery and deposition rates. The authors also provided vital insights on engine performance deterioration associated with deposition and erosion backed by relevant studies. Citations from both these sources are significant to the scope of the current work and are discussed from here on.

Tabakoff et al. [18] computed trajectories of particles through the compressor and the inlet separator region of the helicopter engine. For their calculation, they utilized governing equations of the particle motion in the rotating frame coupled with empirical correlations to determine restitution characteristics. In their analysis, they identified the frequency and distribution of particle impact on the blade surfaces of stator and rotor at different stages of the compressor. Their analysis crucially helped in locating the zones within the compressor that are most prone to erosion. Richardson et al. [324] investigated the key damage mechanisms associated with the high-pressure compressor and established an analytical model to predict performance losses associated with component wear. Among damage mechanisms, they quantified the performance reduction as the blade tip is abraded with time. They also evaluated the impact of surface smoothness degradation in their study.

Matching actual gas turbine operating conditions in experimental settings is expensive with limited functionality of measurement capabilities. Some experimental investigations of particle deposition can be found at relatively moderate temperature conditions and atmospheric pressure conditions. Lundgreen et al. [325] performed deposition tests at a gas temperature of 1350 °C and a combustor pressure of 135.1 kPa. Investigation of particle deposition over cooled surfaces was also performed by Layrock and Fletcher [326], and Crosby et al. [327] at the flow temperature of approximately 1400 °C and 1200 °C, respectively. Reagle et al. [328] collected high-velocity impact data for particle sizes of $20 - 40\ \mu m$ at various impingement angles and went up to 800 °C. More recently, Bons et al. [329] carried out detailed experiments to establish rebound characteristics of quartz particles over an aluminum surface for a range of impact velocity and angles. A similar study was carried out by Whitaker and Bons [330] to obtain the restitution properties of coal ash and to evaluate the performance of relevant particle impact models using the experimental data. The study done by Sacco et al. [331] investigated the effect of extreme pressure on the extent of deposition. They went up to 14.6 atmospheric pressures and found that elevated pressure leads to a decrease in a deposition. The blockage of cooling holes has also been investigated at the low temperatures of the order of 1000 °C when some of the constituents of the sand start to melt and are susceptible to sticking.

Kim et al. [332] studied the deposition behavior of volcanic materials ingested in the gas turbine engine and examined how the deposition is affected by the melting characteristics of the ingested particles. They determined that the deposition rate at the vane surface increases as it starts to accumulate the material. They

also observed that the deposition rate increases at elevated inlet temperature conditions due to particles undergoing partial melting. Vane surface temperature was also found to play a crucial role in governing the deposition behavior. Dunn et al. [22] arrived at a similar conclusion when they tested series of aircraft engines under conditions resembling operation within dust-laden clouds. The particulate mixtures used in the testing were comprised of soil types mixed with volcanic ash at different proportions. They identified a threshold turbine inlet temperature of 2000 °F (1093 °C) beyond which the response of the engine became significantly adverse to the dust ingestion and the deposition of material in the high-pressure turbine vanes resulted in a rapid surge in burner pressure. After the tests, the researchers noticed considerable deposition on the leading edge of the high-pressure turbine vanes at the pressure side. Severe degradation in the form of overheating of the vanes was also observed due to the blockage of cooling holes.

Research conducted by Walsh et al. [283] focused primarily on flow blockages occurring in the blade and combustor liner due to the deposition of ingested sand particles. They compared the blockage behavior at ambient and elevated temperatures in their study and established a relationship between blockage extent and the operating temperature. Compared to ambient temperatures, the researchers observed significant blockage in film-cooling holes. They attributed the blockage to the increased stickiness of the sand due to the partial meltdown. They also found that by varying the pattern of the film cooling holes with respect to the impingement holes, the impact of the deposition can be mitigated to a certain extent. Schneider et al. [333] conducted experimental investigations with accompanying numerical simulations of the flow path of ingested particles in the internal cooling air system. In their test rig, they found extensive deposits of particles in the cooling holes located in the outer cavity surrounding the rotor despite substantial centrifugal forces. The strong adhesion forces were attributed to the van der Waals forces that relate directly with the centrifugal forces. They used Lagrangian particle tracking for numerically simulating the solid particles with one-way coupling between the continuum and dispersed phases. For smaller particles that will follow the trajectory of the fluid flow, they were able to identify stagnation points that agreed with particle deposits observed in the experiment.

5.4 Universal Model: Key Challenges. Ingestion of particulate matter into gas turbine engines is an inevitable process that is highly detrimental to engine performance and service life. These detrimental effects will continue to grow, as the operation of engines at higher temperatures is needed to extract greater thermal efficiency from the engine. A substantial number of experimental studies have been conducted to date in order to understand the particle deposition behavior as a function of one or more system parameters related to the particle, the surface, and the confining environment. These studies have helped greatly in understanding how specific parameters affect the deposition/restitution behavior of the particle. These studies have also led to the development of relevant empirical models that have provided promising predictions for the specific cases they are conditioned for. However, empirical models require condition-relevant experimental investigations, and replicating particle-wall interactions at the extreme operating conditions of turbomachinery in laboratory settings comes with a considerable cost. The measurement techniques available under such conditions are also expensive and limited.

Physics-based models that can be integrated with available computational fluid dynamics techniques present an affordable alternative to experimental studies. A validated physics model can provide detailed descriptions of the particle deposition behavior including deformation, temporal, and sticking properties. This information can guide the development of better material coatings and aid in the prediction of component life expectancy and performance gradients due to deposition with much better accuracy than is currently possible. By augmenting physics-based models with modern uncertainty quantification tools, relevant particle properties responsible for deposition and susceptible regions in the components can also be identified and used to accelerate the component design cycle. However, it is not trivial to develop physics-based models for particle-surface interaction problems that involve coupling between multiple physical processes. The problem becomes more complicated at high-temperature conditions where the material properties of the particle are not well established and the particle size is several orders of magnitude smaller than the environment with which they interact. Moreover, depending on the composition, the particulate matter can undergo a phase transition to a molten/semimolten state. When in a semimolten state, particles may exhibit viscous behaviors with non-Newtonian properties post-crystallization [334]. To determine properties right before the collision, the model itself needs to be multiregime by accommodating separate formulations for modeling phase change. The data pertaining to the properties of particles at such high temperatures is very scarce. Typically, physics-based models are limited to standard particle properties without much scope for variation in their temperature-dependent properties or phase. An integrated effort to refine existing physics-based models from data obtained through limited but specialized experimental investigations of particle impact and properties at extreme conditions seem to be the most feasible path forward toward obtaining a universal predictive framework for particle-laden flows within turbomachinery.

6 Perspectives and Outlook

In light of the advances presented in this review, there still exists ample opportunities for predictive modeling of multiphase fluid dynamics. Research directions where multiphase fluid modeling can exert an important impact are as follows:

6.1 Model Development for Particle–Particle and Particle-Wall Interactions Using Machine Learning Techniques. Significant progress has been made in the past decade on the development of machine-learned (ML) models for the prediction of gaseous and multiphase fluid dynamic flows, a detailed review of which can be found in the recent review paper by Brunton et al. [335]. The goal of such developments can be classified into two categories: (1) surrogate models to facilitate parametric sweeps during design space exploration or to inform real-time decision making; and (2) closure models for key physical phenomena that can be integrated in computational codes to improve solution accuracy and/or accelerate the computations.

Multiple research groups have developed surrogate models using different machine learning techniques. These include Bayesian-based algorithms, such as Gaussian processes [336,337], auto-encoders [338], and kriging [339], and data-driven and physics-informed artificial neural networks (often discussed using either ANN for artificial neural networks and/or PINN for physics-informed artifical neural networks) [340–344].

Some of the recent work on closure models includes machine learning-based subgrid models for chemical kinetics closure in simulations of turbulent reacting flows [345–347], and Reynolds stress closure in nonreacting flows [348–354].

While a number of ML-based surrogates and closure models for single-phase gaseous flows have been developed in the recent past, apart from a few recent research efforts [336,337,355], the literature is lean with respect to ML models for multiphase flows. Currently, existing particle-wall interaction models [251,356,357] fail to accurately predict the physical processes because they are not universal. Most of them are based on empirical evidence and likely cover only a particular regime. As detailed in a recent review paper by Moreira et al. [147], because of the extremely complex and diverse nature of particle-wall physics that is likely governed by different parameters in different regimes and periods during an injection cycle, it may not even be possible to develop generalized models for this phenomena using traditional methods.

There have been a few research efforts in the past that have attempted to develop generalized models spanning multiple regimes for droplet breakup phenomena using ad hoc statistical analyses [358,359], but the integration of state of the art machine learning techniques with high-fidelity experimental and computational data is still in its infancy.

This presents a unique opportunity for the development of physics-informed and data-driven ML algorithms for liquid/gas/solid flows. Specifically, machine-learning-based generalized closure models to predict particle–particle and particle-wall interactions using data-driven or physics-informed techniques should be developed such that they can be incorporated in multiphase computational frameworks to accurately model the phenomenon and significantly accelerate the flow solutions. The absence of such models is one of the critical bottlenecks preventing the understanding of turbulent multiphase fluid dynamics in a full-scale engine configurations, both because of a lack of model accuracy and a lack of computational efficiency. In a gas-turbine engine, in addition to the liquid ligaments and droplets created during fuel atomization, there might also exist hundreds of thousands of solid sand particles that are ingested, especially in desert environments. This is an example of the type of simulation problems that will benefit greatly from advances in ML approaches.

6.2 Novel Analysis of Turbulence Dynamics Using Non-Local Methods. Turbulence dynamics are governed by the solution of the Navier Stokes Equations, and generally exhibit large statistical deviations from Gaussian behavior. This is especially the case at scales where small-scale structures in the form of self-organized, intense vortex filaments develop [360]. It is generally accepted that energy cascades from large eddies to successively smaller eddies until length scales are such that energy is dissipated by kinetic energy turning into heat. Normal scaling behavior associated with the Kolmogorov 1941 (K41) classical theory of turbulence [361] is based on Kolmogorov's hypothesis that, unlike large-scale turbulent motions, small-scale or local turbulent motions are statistically isotropic. The connection between turbulent structures of different time and length scales and the cascade of energy transfer in turbulent flows has been widely reported in textbooks such as [361]. Although this theory underpins many widely adopted turbulence model closures (e.g., eddy viscosity) [362], it still lacks a complete description of the interaction physics. Recent findings suggest that non-Gaussian behaviors at the smaller scales are the result of nonlocal interactions between energy-containing structures. In Refs. [361] and [360], researchers reported on the significant role nonlocal interactions have in generating intense vortices leading to intermittency, as well as the role of local interactions in dissipating energy via turbulent viscosity. By using numerical simulations, they also determined that nonlocal interactions dominate local effects by several orders of magnitude. In Ref. [363], they reported that spatially filtering of the Navier Stokes equations, as is often done for large eddy simulations, enhances the existing nonlocality emerging in the corresponding subgrid-scale fluid motions. These findings further highlight the need for the development of new nonlocal closure models that obey the non-Gaussian statistics of turbulent flows.

Remarkable progress has been made recently in the area of nonlocal modeling of turbulent flows. The models have been enabled by recent breakthroughs in mathematical methods based on fractional-order calculus theory and its applications [364–366]. The main advantage of fractional models compared to their classical counterparts is known to be their ability to incorporate the inherent nonlocalities and non-Gaussian statistics of multiscale problems in the integro-differential operators. A prime example of this is the pioneering work by Chen [367] that formulated the use of a fractional Laplacian model to represent the Reynolds stresses in wall-bounded flows with a fixed fractional order. Although it was restrictive, it inspired a wide array of new methods including novel formulations that allowed the fractional order of the model to vary with distance from the wall [368], as well as integrating the use of fractional operators with deep neural networks to obtain universal scaling laws for the total shear stress using variable order fractional derivatives [364]. More recently, a nonlocal subgrid-scale model was introduced for large eddy simulation, based on the compact expressivity of fractional derivative operators in the eddy viscosity closure [366]. Based on fixed variable order, a priori testing with DNS demonstrated that nonlocal models provide a more realistic prediction of turbulence statistics compared to the classical local eddy viscosity models. These works demonstrate the importance of fractional order methods for nonlocal modeling of Reynolds stress, subfilter stress, and resolved-scale fluid dynamics. Hence, this emerging field provides an interesting capability and the potential for a new class of large eddy simulation analysis tools.

Continued development of nonlocal models extended to complex multiphase high-temperature flows will be important to reliably predict the multiscale nature of its interactions and evolution.

6.3 Introduction of Uncertainty Quantification Methods Into the Modeling Framework. Uncertainty quantification (UQ) and uncertainty-based sensitivity analysis (SA) are growing areas of research in computational engineering and of increasing importance in analysis of multiphase flows. The inherent complexity of multiphase fluid systems, such as those reviewed in this article, implies the predictions depend on several input and phenomenological parameters such as the Stokes, Weber, and Reynolds numbers, particle shape, material properties, and surface morphology (smooth, rough, curved surface), to name a few. Moreover, most of the models present a strongly coupled nonlinear relationship between input and response variables often defined through constitutive relationships [369]. To increase the reliability of simulation results, strategies that account for the influence of the variability associated with input parameters being used to characterize the multiscale and multiphase fluid system are highly desirable. Uncertainty quantification analysis provides an effective tool for tracing the effects of uncertainty associated with different parameters used in a model as well as with the model itself. Such uncertainties are often classified into two categories, aleatory or epistemic.

(1) Aleatory uncertainty is due to randomness related to a physical process. This type of uncertainty is considered reducible, provided that an adequate statistical description is available. Probability theory is used for modeling this type of uncertainty, and there are well-established sampling or stochastic expansion methods for the UQ and SA of response quantities involving aleatory uncertainties [370].
(2) Epistemic uncertainty is due to a lack of information or understanding of the process being modeled [371]. Theoretically, this type of uncertainty might also be considered to be reducible, provided that new information, such as what a domain expert might provide, can be used to supplement or in some way improve the fidelity of the model itself [372]. In the absence of new knowledge, however, this type of uncertainty is irreducible, and the use of probability distributions to characterize what is unknown is significantly more challenging, often involving probability strategies that bound what is not known.

Here, we draw heavily on observations from a recent (2020) case study by Enderle et al. [373], which provides a thoughtful assessment of the state of the art and challenges associated with the applications of UQ and SA in the simulation of a turbulent combusting spray. Enderle et al. note that the computational costs of high fidelity spray simulations become "prohibitive for large scale simulation" when standard approaches for capturing the effects of variability are employed, even if relevant probability density distributions are well known. Their approach uses sensitivity analysis to reduce the stochastic dimensions of the problem to be simulated, and then they employ surrogate models or stochastic expansions in lieu of high fidelity simulation models. They

identify the most influential parameters for their study a priori using a Morris One At a Time sensitivity analysis, and a posteriori, using Sobol' indices. They use the class of stochastic expansion methods known as the polynomial chaos expansion approach [374] to develop their surrogate model and the Latin Hypercube Sampling [375] approach to bound model input uncertainties. Both of these methods are drawing increased attention for their use in UQ [376,377].

Although there are several uncertainty quantification analysis studies pertaining to computational fluid dynamics available in the literature [378,379], the cited work by Enderle et al. [373] is the first we are aware of that incorporates multiphase combustion regimes and represents an important first step toward directly focusing on establishing uncertainties comprehensively in a multiscale/multiphase/multiphysics framework. The authors believe that incorporating UQ–SA-based approaches is critical for the development of a predictive multiscale, multiphase modeling framework.

6.4 Hot Particulate Ingestion Rig (HPIR) for Community-Wide Multiphase Flow Canonical Studies. Sand laden particulate flow and molten sand deposition onto target specimens can be simulated using the Army Research Laboratory's Hot Particulate Ingestion Rig (HPIR) experimental facility, that is shown in Fig. 11. The HPIR is a canonical laboratory-scale combustor system that is capable of operating with gas temperatures up to 1650 °C, gas velocities up to a Mach number of 0.8, and mass flow rates up to 0.34 kg/s. In addition, various sands/dust/ash particle concentrations can be directly fed (up to 200 g/min) into the combustor to realistically simulate sand transport and CMAS formation. Once the particle clusters exit the combustor they travel further downstream, impact and deposit on a material substrate (often a thermal barrier coating). During operation, particle image velocimetry or laser doppler velocimetry (LDV) can be used to track particle trajectory in the hot gas flow field as well as the rebound velocities. Thermal Barrier Coatings can be exposed to a high velocity (Mach 0.3), high temperature (1400 °C) gas flow that is laden with synthetic sand (fed at 1 g/min) simulating gas turbine engine-like operating condition. Each sample can be exposed to cyclic hot/cold conditions with sand ingestion. In addition to this "dry" test, a high humidity test using a water fogger can be conducted to simulate a water vapor attack.

Infrared (IR) cameras, pyrometers, and thermocouples are available to monitor the thermal profile across the coated substrate both on the front and back side of the specimens. Microstructural characterization and mechanical properties of the coatings are evaluated before and after CMAS exposure. Also, accumulated sand weight, deposition thickness, weight/volumetric analysis, micro-indentation, nano-indentation (hardness, elastic modulus), X-ray diffraction, thermal gravimetric analysis, and scanning electron microscopy can be conducted. This facility can be used to correlate the developed multiphysics model at all levels to be able to assess the CMAS resistance of newly developed coatings. Further information about this facility is found in Ref. [380].

Fig. 11 Schematic of Army Research Laboratory's Hot Particulate Ingestion Rig (HPIR) [380]

7 Conclusion

Significant success has been achieved in multiphase flow modeling in terms of capturing its turbulent transport and splashing/breakup due to particle-wall interactions. Modeling approaches today are able to describe strongly coupled interactions between turbulence and discrete particulates at a wide range of regimes. The number of seminal publications and validated models is a strong indicator of its success having a wide range of applicability. Indeed, these models have played a strong role in enabling discoveries and new technologies. However, the literature also reveals a significant amount of empiricism in the models that often leads to a calibration process when conducting validation studies. Uncertainties in model physical properties, boundary conditions, turbulence, and particle-wall interaction modeling have been shown to require additional recalibration. Models tend to be developed with numerical constants that allow control of a specific process (such as deposition or rebound) that has been vetted based on experimental relationships. Multiphase fluid dynamic models, such as the ones reviewed in this article, remain largely based on simplified modeling assumptions hence lack a complete description. Because of this, ample opportunities exist for making significant contributions to the development and validation of predictive models that are based on first principles and benefit from the use of uncertainty quantification methods. Equally exciting are the opportunities for use of these next generation of models in conducting reliable, high-fidelity integrated computer simulations of heterogeneous multiphase flows in engineering systems, and specifically for the design of new T/EBC systems that resist CMAS attack at even higher temperatures than encountered in today's gas turbine engines.

Nomenclature

Non-Dimensional Numbers

Ja = Jakob number
La = Laplace number
Nu = Nusselt number
Oh = Ohnesorge number
Pr = Prandtl number
Re = Reynolds number
St = Stokes number
We = Weber number

Subscripts

d = droplet
f = film
G = gas
L = leidenfrost
P = particle
sat = saturation
w = wall

Acronyms

CoR = coefficient of restitution
CHF = critical heat flux
DNS = direct numerical simulation
LBM = lattice Boltzmann method
LS = level set
SPH = smoothed particle hydrodynamics
T/EBC = thermal and environmental barrier coating
TBC = thermal barrier coating
VOF = volume of fluid

Latin Letters

c_p = heat capacity
D = diameter
F = force

H = thickness
K = generic threshold
K = thermal conductivity
L = latent heat
m = mass
N_p = Parcel number
R_a = mean wall roughness amplitude
T = temperature
U = velocity (Eulerian)
V = velocity (Lagrangian)

Greek Symbols

αV = liquid volume fraction
β_{max} = non-dimensional maximum spread
δ = non-dimensional lengthVolume
μ = dynamic viscosity
Φ_p = particle volume fraction
Ψ = angle
ρ = density
σ = surface tension
τ = characteristic time
θ_a, θ_r = advancing, receding contact angle
θ_C = static contact angle

Funding Data

- Army Research Office (Grant No. W911NF1910225; Funder ID: 10.13039/100000183) .
- Helmholtz-Gemeinschaft (Grant No. 34.14.02; Funder ID: 10.13039/501100001656).
- National Science Foundation (Grant No. 2018617; Funder ID: 10.13039/100000001).
- U.S. Army Research Laboratory (Grant Nos. ARLAP44862H70 and W911QX-16-D-0014; Funder ID: 10.13039/100006754).
- Vertical Lift Research Center of Excellence (Grant No. W911W61120012; Funder ID: 10.13039/100006769).

References

[1] Guffanti, M., Casadevall, T. J., and Budding, K., 2010, "Encounters of Aircraft With Volcanic Ash Clouds; a Compilation of Known Incidents, 1953-2009," Tech. rep., U.S. Geological Survey Data Series 545, ver. 1.0.

[2] Seck, H. H., 2016, "Billows of Dust, a Sudden 'Pop' and an Osprey Falls From the Sky," accessed May 24, 2021, https://www.military.com/daily-news/2016/01/29/billows-of-dust-a-sudden-pop-and-an-osprey-falls-from-the-sky.html

[3] Bojdo, N., and Filippone, A., 2019, "A Simple Model to Assess the Role of Dust Composition and Size on Deposition in Rotorcraft Engines," Aerospace, **6**(4), p. 44.

[4] van Donkelaar, A., Martin, R., Brauer, M., Kahn, R., Levy, R., Verduzco, C., and Villeneuve, P., 2010, "Global Estimates of Ambient Fine Particulate Matter Concentrations From Satellite-Based Aerosol Optical Depth: Development and Application," Environ. Health Perspectives, **118**(6), pp. 847–855.

[5] Hammer, M. S., van Donkelaar, A., Li, C., Lyapustin, A., Sayer, A. M., Hsu, N. C., Levy, R. C., Garay, M. J., Kalashnikova, O. V., Kahn, R. A., Brauer, M., Apte, J. S., Henze, D. K., Zhang, L., Zhang, Q., Ford, B., Pierce, J. R., and Martin, R. V., 2020, "Global Estimates and Long-Term Trends of Fine Particulate Matter Concentrations (1998–2018)," Environ. Sci. Technol., **54**(13), pp. 7879–7890.

[6] Walock, M., Barnett, B., Ghoshal, A., Murugan, M., Swab, J., Hopkins, M., Gazonas, G., Rowe, C., and Kerner, K., 2017, "Micro-Scale Sand Particles Within the Hot Section of a Gas Turbine Engine," Mechanical Properties and Performance of Engineering Ceramics and Composites XI, J. Salem, D. Singh, M. Fukushima, and A. Gyekenyesi, eds., John Wiley & Sons, Hoboken, NJ, Vol. 37, pp. 159–170.

[7] Neito, A., Walock, M., Ghoshal, A., Zhu, D., Gamble, W., Barnett, B., Murugan, M., Pepi, M., Rowe, C., and Pegg, R., 2018, "Layered, Composite, and Doped Thermal Barrier Coatings Exposed to Sand Laden Flows Within a Gas Turbine Engine: Microstructural Evolution, Mechanical Properties, and CMAS Deposition," Surf. Coat. Technol., **349**, pp. 1107–1116.

[8] Ghoshal, A., Murugan, M., Walock, M. J., Nieto, A., Barnett, B. D., Pepi, M. S., Swab, J. J., Zhu, D., Kerner, K. A., Rowe, C. R., Shiao, C.-Y. (M.)., Hopkins, D. A., and Gazonas, G. A., 2018, "Molten Particulate Impact on Tailored Thermal Barrier Coatings for Gas Turbine Engine," J. Eng. Gas Turbines Power, **140**(2), p. 022601.

[9] Murugan, M., Ghoshal, A., Walock, M., Barnett, B., Pepi, M., and Kerner, K., 2017, "Sand Particle Induced Deterioration of Thermal Barrier Coatings on Gas Turbine Blades," Adv. Aircr. Spacecr. Sci., **4**(1), pp. 37–52.

[10] Fehrenbacher, L., Kroliczek, D., Kutsch, J., Vesnovsky, I., Fehrenbacher, E., Ghoshal, A., Walock, M., and Nieto, A., 2019, "Advanced Environmental Barrier Coatings for SiC CMCs," Adv. Ceram. Environ., Funct., Struct., Energy Appl. II, **26**, pp. 83–93.

[11] Balachandar, S., and Eaton, J. K., 2010, "Turbulent Dispersed Multiphase Flow," Annu. Rev. Fluid Mech., **42**(1), pp. 111–133.

[12] Guha, A., 2008, "Transport and Deposition of Particles in Turbulent and Laminar Flow," Annu. Rev. Fluid Mech., **40**(1), pp. 311–341.

[13] Hamed, A., Tabakoff, W. C., and Wenglarz, R., 2006, "Erosion and Deposition in Turbomachinery," J. Propuls. Power, **22**(2), pp. 350–360.

[14] Zhang, F., Liu, Z., Liu, Z., and Diao, W., 2020, "Experimental Study of Sand Particle Deposition on a Film-Cooled Turbine Blade at Different Gas Temperatures and Angles of Attack," Energies, **13**(4), p. 811.

[15] Federal Aviation Administration, 2016, *Airplane Flying Handbook (FAA-H-8083-3B)*, Skyhorse Publishing Inc, New York.

[16] Murugan, M., Ghoshal, A., Walock, M., Nieto, A., Bravo, L., Barnett, B., Pepi, M., Swab, J., Pegg, R. T., Rowe, C., Zhu, D., and Kerner, K., 2017, "Microstructure Based Material-Sand Particulate Interactions and Assessment of Coatings for High Temperature Turbine Blades," ASME Paper No. GT2017-64051.

[17] Dunn, M. G., Padova, C., and Adams, R., 1987, "Operation of Gas Turbine Engines in Dust-Laden Environments," ASME. J. Turbomach. **134**(5), p. 051001.

[18] Tabakoff, W., 1987, "Compressor Erosion and Performance Deterioration," ASME J. Fluids Eng., **109**(3), pp. 297–306.

[19] Chang, W.-R., and Ling, F. F., 1992, "Normal Impact Model of Rough Surfaces," ASME J. Tribol., **114**(3), pp. 439–447.

[20] Wadley, H. N. G., 2013, "High Temperature Coatings," accessed May 26, 2021, https://www2.virginia.edu/ms/research/wadley/high-temp.html

[21] Dahneke, B., 1975, "Further Measurements of the Bouncing of Small Latex Spheres," J. Colloid Interface Sci., **51**(1), pp. 58–65.

[22] Dunn, M. G., Baran, A. J., and Miatech, J., 1996, "Operation of Gas Turbine Engines in Volcanic Ash Clouds," ASME J. Eng. Gas Turbines Power, **118**(4), pp. 724–731.

[23] Linden, D., 2018, "Know Your Turbomachinery's Operating Environment!," Houston, TX, accessed May 26, 2021, https://oaktrust.library.tamu.edu/bitstream/handle/1969.1/175022/10_Linden.pdf?sequence=1&isAllowed=y

[24] Borom, M. P., Johnson, C. A., and Peluso, L. A., 1996, "Role of Environment Deposits and Operating Surface Temperature in Spallation of Air Plasma Sprayed Thermal Barrier Coatings," Surf. Coat. Technol., **86–87**, pp. 116–126.

[25] Jackson, R. W., Zaleski, E. M., Poerschke, D. L., Hazel, B. T., Begley, M. R., and Levi, C. G., 2015, "Interaction of Molten Silicates With Thermal Barrier Coatings Under Temperature Gradients," Acta Mater., **89**, pp. 396–407.

[26] Krämer, S., Yang, J., Levi, C. G., and Johnson, C. A., 2006, "Thermochemical Interaction of Thermal Barrier Coatings With Molten CaO–MgO–Al_2O_3–SiO_2 (CMAS) Deposits," J Am. Ceram. Soc., **89**(10), pp. 3167–3175.

[27] Mercer, C., Faulhaber, S., Evans, A. G., and Darolia, R., 2005, "A Delamination Mechanism for Thermal Barrier Coatings Subject to Calcium–Magnesium–Alumino-Silicate (CMAS) Infiltration," Acta Mater., **53**(4), pp. 1029–1039.

[28] Evans, A., Mumm, D., Hutchinson, J., Meier, G., and Pettit, F., 2001, "Mechanisms Controlling the Durability of Thermal Barrier Coatings," Prog. Mater. Sci., **46**(5), pp. 505–553.

[29] Kharaz, A. H., Gorham, D. A., and Salman, A. D., 1999, "Accurate Measurement of Particle Impact Parameters," Meas. Sci. Technol., **10**(1), pp. 31–35.

[30] Kim, J., Dunn, M. G., Baran, A. J., Wade, D. P., and Tremba, E. L., 1993, "Deposition of Volcanic Materials in the Hot Sections of Two Gas Turbine Engines," ASME Paper No. 92-GT-219.

[31] Schiller, L., and Naumann, Z., 1933, "Über Die Grundlegende Berechnung Bei Der Schwerkraftaufbereitung," Z. Des Vereins Deutscher Ingenieure, **77**, pp. 318–320.

[32] McKinley, G. H., and Renardy, M., 2011, "Wolfgang Von Ohnesorge," Phys. Fluids, **23**(12), p. 127101.

[33] Ruzicka, M., 2008, "On Dimensionless Numbers," Chem. Eng. Res. Des., **86**(8), pp. 835–868.

[34] Wierzba, A., 1990, "Deformation and Breakup of Liquid Drops in at Nearly Critical Weber Numbers," Exp. Fluids, **9**(1–2), pp. 59–64.

[35] Hannebique, G., Sierra, P., Riber, E., and Cuenot, B., 2013, "Large Eddy Simulation of Reactive Two-Phase Flow in an Aeronautical Multipoint Burner," Flow, Turbulence Combustion, **90**(2), pp. 449–469.

[36] Jones, W., Marquis, A., and Vogiatzaki, K., 2014, "Large-Eddy Simulation of Spray Combustion in a Gas Turbine Combustor," Combust. Flame, **161**(1), pp. 222–239.

[37] Mattingly, J. D., 1996, *Elements of Gas Turbine Propulsion*, **1**, McGraw-Hill, New York.

[38] Jain, N., Bravo, L., Bose, S., Kim, D., Murugan, M., Ghoshal, A., and Flatau, A., 2018, "Turbulent Multiphase Flow and Particle Deposition of Sand Ingestion for High-Temperature Turbine Blades," Studying Turbulence Usinng Numerical Simulation Dabases - XVII, Proceedings of the 2018 Center for Turbulence Research Summer Program, Stanford University Press, Palo Alto, CA.

[39] Li, B., Chen, Z., Zheng, H., Li, G., Li, H., and Peng, P., 2019, "Wetting Mechanism of CMAS Melt on Ysz Surface at High Temperature: First-Principles Calculation," Appl. Surf. Sci., **483**, pp. 811–818.

[40] Cowherd, C., 2007, "Sandblaster 2 Support of See-Through Technologies for Particulate Brownout," Tech. Rep. 110565.1.005, Midwest Research Institute, Kansas City, MO, accessed May 26, 2021, https://apps.dtic.mil/sti/pdfs/ADA504965.pdf
[41] Sommerfeld, M., 2017, "Numerical Methods for Dispersed Multiphase Flows," Particles in Flows, Advances in Mathematical Fluid Mechanics, T. Bodnár, G. Galdi, and Š. Nečasová, Birkhäuser, Cham, pp. 255–326, Vol. 6.
[42] Elghobashi, S., 1994, "On Predicting Particle-Laden Turbulent Flows," Appl. Sci. Res., **52**(4), pp. 309–329.
[43] Prosperetti, A., and Tryggvason, G., 2009, *Computational Methods for Multiphase Flow*, Cambridge University Press, Cambridge, UK.
[44] Loth, E., 2000, "Numerical Approaches for Motion of Dispersed Particles, Droplets and Bubbles," Prog. Energy Combustion Sci., **26**(3), pp. 161–223.
[45] Kajishima, T., 2004, "Influence of Particle Rotation on the Interaction Between Particle Clusters and Particle-Induced Turbulence," Int. J. Heat Fluid Flow, **25**(5), pp. 721–728.
[46] Gore, R. A., and Crowe, C. T., 1989, "Effect of Particle Size on Modulating Turbulent Intensity," Int. J. Multiphase Flow, **15**(2), pp. 279–285.
[47] Kulick, J. D., Fessler, J. R., and Eaton, J. K., 1994, "Particle Response and Turbulence Modification in Fully Developed Channel Flow," J. Fluid Mech., **277**, pp. 109–134.
[48] Squires, K. D., and Eaton, J. K., 1990, "Particle Response and Turbulence Modification in Isotropic Turbulence," Phys. Fluids A, **2**(7), pp. 1191–1203.
[49] Reeks, M. W., 1983, "The Transport of Discrete Particles in Inhomogeneous Turbulence," J. Aerosol Sci., **14**(6), pp. 729–739.
[50] Marchioli, C., and Soldati, A., 2002, "Mechanisms for Particle Transfer and Segregation in a Turbulent Boundary Layer," J. Fluid Mech., **468**, pp. 283–315.
[51] Marchioli, C., Giusti, A., Salvetti, M. V., and Soldati, A., 2003, "Direct Numerical Simulation of Particle Wall Transfer and Deposition in Upward Turbulent Pipe Flow," Int. J. Multiphase Flow, **29**(6), pp. 1017–1038.
[52] Fong, K., Amili, O., and Coletti, F., 2019, "Velocity and Spatial Distribution of Inertial Particles in a Turbulent Channel Flow," J. Fluid Mech., **872**, pp. 367–406.
[53] Moin, P., and Mahesh, K., 1998, "Direct Numerical Simulation: A Tool in Turbulence Research," Annu. Rev. Fluid Mech., **30**(1), pp. 539–578.
[54] Tenneti, S., and Subramaniam, S., 2014, "Particle-Resolved Direct Numerical Simulation for Gas-Solid Flow Model Development," Annu. Rev. Fluid Mech., **46**(1), pp. 199–230.
[55] Bagchi, P., and Balachandar, S., 2003, "Effect of Turbulence on the Drag and Lift of a Particle," Phys. Fluids, **15**(11), pp. 3496–3513.
[56] Burton, T. M., and Eaton, J. K., 2005, "Fully Resolved Simulations of Particle-Turbulence Interaction," J. Fluid Mech., **545**(1), pp. 67–111.
[57] Vreman, A. W., 2016, "Particle-Resolved Direct Numerical Simulation of Homogeneous Isotropic Turbulence Modified by Small Fixed Spheres," J. Fluid Mech., **796**, pp. 40–85.
[58] Koblitz, A. R., Lovett, S., Nikiforakis, N., and Henshaw, W. D., 2017, "Direct Numerical Simulation of Particulate Flows With an Overset Grid Method," J. Comput. Phys., **343**, pp. 414–431.
[59] Glowinski, R., Pan, T. W., Hesla, T. I., Joseph, D. D., and Périaux, J., 2001, "A Fictitious Domain Approach to the Direct Numerical Simulation of Incompressible Viscous Flow Past Moving Rigid Bodies: Application to Particulate Flow," J. Comput. Phys., **169**(2), pp. 363–426.
[60] Patankar, N. A., Singh, P., Joseph, D. D., Glowinski, R., and Pan, T. W., 2000, "A New Formulation of the Distributed Lagrange Multiplier/Fictitious Domain Method for Particulate Flows," Int. J. Multiphase Flow, **26**(9), pp. 1509–1524.
[61] Shao, X., Wu, T., and Yu, Z., 2012, "Fully Resolved Numerical Simulation of Particle-Laden Turbulent Flow in a Horizontal Channel at a Low Reynolds Number," J. Fluid Mech., **693**, pp. 319–344.
[62] Diaz-Goano, C., Minev, P. D., and Nandakumar, K., 2003, "A Fictitious Domain/Finite Element Method for Particulate Flows," J. Comput. Phys., **192**(1), pp. 105–123.
[63] Yu, Z., Lin, Z., Shao, X., and Wang, L. P., 2016, "A Parallel Fictitious Domain Method for the Interface-Resolved Simulation of Particle-Laden Flows and Its Application to the Turbulent Channel Flow," Eng. Appl. Comput. Fluid Mech., **10**(1), pp. 160–170.
[64] Kajishima, T., and Takiguchi, S., 2002, "Interaction Between Particle Clusters and Particle-Induced Turbulence," Int. J. Heat Fluid Flow, **23**(5), pp. 639–646.
[65] Haeri, S., and Shrimpton, J. S., 2012, "On the Application of Immersed Boundary, Fictitious Domain and Body-Conformal Mesh Methods to Many Particle Multiphase Flows," Int. J. Multiphase Flow, **40**, pp. 38–55.
[66] Uhlmann, M., 2008, "Interface-Resolved Direct Numerical Simulation of Vertical Particulate Channel Flow in the Turbulent Regime," Phys. Fluids, **20**(5), p. 053305.
[67] Lucci, F., Ferrante, A., and Elghobashi, S., 2010, "Modulation of Isotropic Turbulence by Particles of Taylor Length-Scale Size," J. Fluid Mech., **650**, pp. 5–55.
[68] Picano, F., Breugem, W. P., and Brandt, L., 2015, "Turbulent Channel Flow of Dense Suspensions of Neutrally Buoyant Spheres," J. Fluid Mech., **764**, pp. 463–487.
[69] Mehrabadi, M., Tenneti, S., Garg, R., and Subramaniam, S., 2015, "Pseudo-Turbulent Gas-Phase Velocity Fluctuations in Homogeneous Gas-Solid Flow: Fixed Particle Assemblies and Freely Evolving Suspensions," J. Fluid Mech., **770**, pp. 210–246.
[70] Tschisgale, S., Kempe, T., and Fröhlich, J., 2017, "A Non-Iterative Immersed Boundary Method for Spherical Particles of Arbitrary Density Ratio," J. Comput. Phys., **339**, pp. 432–452.
[71] Azis, M. H. A., Evrard, F., and van Wachem, B., 2019, "An Immersed Boundary Method for Flows With Dense Particle Suspensions," Acta Mech., **230**(2), pp. 485–515.
[72] Kajishima, T., 2019, "Immersed Boundary/Solid Method for the Numerical Simulation of Particle-Laden Flows," Fluid Dyn. Res., **51**(5), p. 051401.
[73] Goza, A., Liska, S., Morley, B., and Colonius, T., 2016, "Accurate Computation of Surface Stresses and Forces With Immersed Boundary Methods," Phys. Comput. Fluids, **321**, pp. 860–873.
[74] Geneva, N., Peng, C., Li, X., and Wang, L. P., 2017, "A Scalable Interface-Resolved Simulation of Particle-Laden Flow Using the Lattice Boltzmann Method," Parallel Comput., **67**, pp. 20–37.
[75] Ernst, M., Dietzel, M., and Sommerfeld, M., 2013, "A Lattice Boltzmann Method for Simulating Transport and Agglomeration of Resolved Particles," Acta Mech., **224**(10), pp. 2425–2449.
[76] Derksen, J. J., 2012, "Direct Numerical Simulations of Aggregation of Monosized Spherical Particles in Homogeneous Isotropic Turbulence," AICHE J., **58**(8), pp. 2589–2600.
[77] Hölzer, A., and Sommerfeld, M., 2009, "Lattice Boltzmann Simulations to Determine Drag, Lift and Torque Acting on Non-Spherical Particles," Comput. Fluids, **38**(3), pp. 572–589.
[78] Gupta, A., Clercx, H., and Toschi, F., 2018, "Simulation of Finite-Size Particles in Turbulent Flows Using the Lattice Boltzmann Method," Commun. Comput. Phys., **23**(3), pp. 665–684.
[79] Wang, L. P., Peng, C., Guo, Z., and Yu, Z., 2016, "Lattice Boltzmann Simulation of Particle-Laden Turbulent Channel Flow," Comput. Fluids, **124**, pp. 226–236.
[80] Peng, C., and Wang, L. P., 2019, "Direct Numerical Simulations of Turbulent Pipe Flow Laden With Finite-Size Neutrally Buoyant Particles at Low Flow Reynolds Number," Acta Mech., **230**(2), pp. 517–539.
[81] Ten Cate, A., Derksen, J. J., Portela, L. M., and Van den Akker, H. E., 2004, "Fully Resolved Simulations of Colliding Monodisperse Spheres in Forced Isotropic Turbulence," J. Fluid Mech., **519**, pp. 233–271.
[82] Feng, Z. G., and Michaelides, E. E., 2004, "The Immersed Boundary-Lattice Boltzmann Method for Solving Fluid-Particles Interaction Problems," J. Comput. Phys., **195**(2), pp. 602–628.
[83] Maxey, M. R., and Riley, J. J., 1983, "Equation of Motion for a Small Rigid Sphere in a Nonuniform Flow," Phys. Fluids, **26**(4), pp. 883–889.
[84] Gatignol, R., 1983, "The Faxén Formulae for aRigid Particle in an Unsteady Non-Uniform Stokes Flow," J. De Mec. Theorique, et Appliquee, **2**, pp. 143–160.
[85] Crowe, C., Schwarzkopf, J., Sommerfeld, M., and Tsuji, Y., 2011, *Multiphase Flows With Droplets and Particles*, CRC Press, Boca Raton, FL.
[86] Lovalenti, P. M., and Brady, J. F., 1993, "The Hydrodynamic Force on a Rigid Particle Undergoing Arbitrary Time-Dependent Motion at Small Reynolds Number," J. Fluid Mech., **256**(29), pp. 561–605.
[87] Parmar, M., Haselbacher, A., and Balachandar, S., 2012, "Equation of Motion for a Sphere in Non-Uniform Compressible Flows," J. Fluid Mech., **699**, pp. 352–375.
[88] Armenio, V., and Fiorotto, V., 2001, "The Importance of the Forces Acting on Particles in Turbulent Flows," Phys. Fluids, **13**(8), pp. 2437–2440.
[89] Horwitz, J. A., and Mani, A., 2016, "Accurate Calculation of Stokes Drag for Point-Particle Tracking in Two-Way Coupled Flows," J. Comput. Phys., **318**, pp. 85–109.
[90] Gualtieri, P., Picano, F., Sardina, G., and Casciola, C. M., 2015, "Exact Regularized Point Particle Method for Multiphase Flows in the Two-Way Coupling Regime," J. Fluid Mech., **773**, pp. 520–561.
[91] Ireland, P. J., and Desjardins, O., 2017, "Improving Particle Drag Predictions in Euler-Lagrange Simulations With Two-Way Coupling," J. Comput. Phys., **338**, pp. 405–430.
[92] Mehrabadi, M., Horwitz, J. A., Subramaniam, S., and Mani, A., 2018, "A Direct Comparison of Particle-Resolved and Point-Particle Methods in Decaying Turbulence," J. Fluid Mech., **850**, pp. 336–369.
[93] Wang, Q., and Squires, K. D., 1996, "Large Eddy Simulation of Particle Deposition in a Vertical Turbulent Channel Flow," Int. J. Multiphase Flow, **22**(4), pp. 667–683.
[94] Uijttewaal, W. S., and Oliemans, R. V., 1996, "Particle Dispersion and Deposition in Direct Numerical and Large Eddy Simulations of Vertical Pipe Flows," Phys. Fluids, **8**(10), pp. 2590–2604.
[95] Kuerten, J. G., and Vreman, A. W., 2005, "Can Turbophoresis Be Predicted by Large-Eddy Simulation?," Phys. Fluids, **17**(1), pp. 011701–4.
[96] Kuerten, J. G., 2016, "Point-Particle DNS and LES of Particle-Laden Turbulent Flow - A State-of-the-Art Review," Flow Turbul. Combust., **97**(3), pp. 689–713.
[97] Capecelatro, J., and Desjardins, O., 2013, "An Euler-Lagrange Strategy for Simulating Particle-Laden Flows," J. Comput. Phys., **238**, pp. 1–31.
[98] Shotorban, B., and Balachandar, S., 2006, "Particle Concentration in Homogeneous Shear Turbulence Simulated Via Lagrangian and Equilibrium Eulerian Approaches," Phys. Fluids, **18**(6), p. 065105.
[99] Shotorban, B., and Balachandar, S., 2007, "A Eulerian Model for Large-Eddy Simulation of Concentration of Particles With Small Stokes Numbers," Phys. Fluids, **19**(11), p. 118107.
[100] Shotorban, B., and Balachandar, S., 2009, "Two-Fluid Approach for Direct Numerical Simulation of Particle-Laden Turbulent Flows at Small Stokes Numbers," Phys. Rev. E - Stat., Nonlinear, Soft Matter Phys., **79**(5), pp. 1–8.
[101] Lindborg, H., Lysberg, M., and Jakobsen, H. A., 2007, "Practical Validation of the Two-Fluid Model Applied to Dense Gas-Solid Flows in Fluidized Beds," Chem. Eng. Sci., **62**(21), pp. 5854–5869.

[102] Ozel, A., Fede, P., and Simonin, O., 2013, "Development of Filtered Euler-Euler Two-Phase Model for Circulating Fluidised Bed: High Resolution Simulation, Formulation and a Priori Analyses," Int. J. Multiphase Flow, **55**, pp. 43–63.
[103] Peirano, E., Delloume, V., Johnsson, F., Leckner, B., and Simonin, O., 2002, "Numerical Simulation of the Fluid Dynamics of a Freely Bubbling Fluidized Bed: Influence of the Air Supply System," Powder Technol., **122**(1), pp. 69–82.
[104] Cheung, S. C., Yeoh, G. H., Qi, F. S., and Tu, J. Y., 2012, "Classification of Bubbles in Vertical Gas-Liquid Flow: Part 2 - a Model Evaluation," Int. J. Multiphase Flow, **39**, pp. 135–147.
[105] Zeng, Z. X., and Zhou, L. X., 2006, "A Two-Scale Second-Order Moment Particle Turbulence Model and Simulation of Dense Gas-Particle Flows in a Riser," Powder Technol., **162**(1), pp. 27–32.
[106] Moreau, M., Simonin, O., and Bédat, B., 2010, "Development of Gas-Particle Euler-Euler LES Approach: A Priori Analysis of Particle Sub-Grid Models in Homogeneous Isotropic Turbulence," Flow, Turbul. Combust., **84**(2), pp. 295–324.
[107] Masi, E., Simonin, O., Riber, E., Sierra, P., and Gicquel, L. Y., 2014, "Development of an Algebraic-Closure-Based Moment Method for Unsteady Eulerian Simulations of Particle-Laden Turbulent Flows in Very Dilute Regime," Int. J. Multiphase Flow, **58**, pp. 257–278.
[108] Kartushinsky, A., Tisler, S., Oliveira, J. L., and van der Geld, C. W., 2016, "Eulerian-Eulerian Modelling of Particle-Laden Two," phase flow,". Powder Technol., **301**, pp. 999–1007.
[109] Chen, X., and Wang, J., 2014, "A Comparison of Two-Fluid Model, Dense Discrete Particle Model and CFD-DEM Method for Modeling Impinging Gas-Solid Flows," Powder Technol., **254**, pp. 94–102.
[110] Meyer, C. J., and Deglon, D. A., 2011, "Particle Collision modeling - A Review," Miner. Eng., **24**(8), pp. 719–730.
[111] Davis, R., Serayssol, J. M., and Hinch, E., 1986, "The Elastohydrodynamic Collision of Two Spheres," J. Fluid Mech., **163**, pp. 479–497.
[112] Maw, N., Barber, J. R., and Fawcett, J. N., 1976, "The Oblique Impact of Elastic Spheres," Wear, **38**(1), pp. 101–114.
[113] Yamamoto, Y., Potthoff, M., Tanaka, T., Kajishima, T., and Tsuji, Y., 2001, "Large-Eddy Simulation of Turbulent Gas-Particle Flow in a Vertical Channel: Effect of Considering Inter-Particle Collisions," J. Fluid Mech., **442**, pp. 303–334.
[114] Barnocky, G., and Davis, R. H., 1988, "Elastohydrodynamic Collision and Rebound of Spheres: Experimental Verification," Phys. Fluids, **31**(6), p. 1324.
[115] Gondret, P., Lance, M., and Petit, L., 2002, "Bouncing Motion of Spherical Particles in Fluids," Phys. Fluids, **14**(2), pp. 643–652.
[116] Joseph, G. G., Zenit, R., Hunt, M. L., and Rosenwinkel, A. M., 2001, "Particle-Wall Collisions in a Viscous Fluid," J. Fluid Mech., **433**, pp. 329–346.
[117] Joseph, G. G., and Hunt, M. L., 2004, "Oblique Particle-Wall Collisions in a Liquid," J. Fluid Mech., **510**(510), pp. 71–93.
[118] Yang, F. L., and Hunt, M. L., 2006, "Dynamics of Particle-Particle Collisions in a Viscous Liquid," Phys. Fluids, **18**(12), p. 121506.
[119] Kempe, T., and Fröhlich, J., 2012, "Collision Modelling for the Interface-Resolved Simulation of Spherical Particles in Viscous Fluids," J. Fluid Mech., **709**, pp. 445–489.
[120] Brändle de Motta, J. C., Breugem, W. P., Gazanion, B., Estivalezes, J. L., Vincent, S., and Climent, E., 2013, "Numerical Modelling of Finite-Size Particle Collisions in a Viscous Fluid," Phys. Fluids, **25**(8), p. 083302.
[121] Qian, J., and Law, C., 1997, "Regimes of Coalescence and Separation in Droplet Collision," J. Fluid Mech., **331**, pp. 59–80.
[122] Pan, K.-L., Law, C. K., and Zhou, B., 2008, "Experimental and Mechanistic Description of Merging and Bouncing in Head-on Binary Droplet Collision," J. Appl. Phys., **103**(6), p. 064901.
[123] Jia, X., Yang, J.-C., Zhang, J., and Ni, M.-J., 2019, "An Experimental Investigation on the Collision Outcomes of Binary Liquid Metal Droplets," Int. J. Multiphase Flow, **116**, pp. 80–90.
[124] Chen, X., Ma, D., Khare, P., and Yang, V., 2011, "Energy and Mass Transfer During Binary Droplet Collision," AIAA Paper No. 2011–771.
[125] Ganti, H., Khare, P., and Bravo, L., 2020, "Binary Collision of CMAS Droplets - Part i: Equal Sized Droplets," J. Mater. Res., **35**(17), pp. 2260–2274.
[126] Ganti, H., Khare, P., and Bravo, L., 2020, "Binary Collision of CMAS Droplets - Part ii: Unequal Sized Droplets," J. Mater. Res., **35**(17), pp. 2275–2287.
[127] Sommerfeld, M., and Kuschel, M., 2016, "Modelling Droplet Collision Outcomes for Different Substances and Viscosities," Exp. Fluids, **57**(12), p. 187.
[128] Gotaas, C., Havelka, P., Jakobsen, H. A., Svendsen, H. F., Hase, M., Roth, N., and Weigand, B., 2007, "Effect of Viscosity on Droplet-Droplet Collision Outcome: Experimental Study and Numerical Comparison," Phys. Fluids, **19**(10), p. 102106.
[129] Nasr, H., Ahmadi, G., and McLaughlin, J. B., 2009, "A DNS Study of Effects of Particleparticle Collisions and Two-Way Coupling on Particle Deposition and Phasic Fluctuations," J. Fluid Mech., **640**, pp. 507–536.
[130] Haddadi, H., Shojaei-Zadeh, S., and Morris, J. F., 2016, "Lattice-Boltzmann Simulation of Inertial Particle-Laden Flow Around an Obstacle," Phys. Rev. Fluids, **1**(2), pp. 1–17.
[131] Troiano, M., Solimene, R., Salatino, P., and Montagnaro, F., 2016, "Multiphase Flow Patterns in Entrained-Flow Slagging Gasifiers: Physical Modelling of Particle-Wall Impact at Near-Ambient Conditions," Fuel Process. Technol., **141**, pp. 106–116.
[132] Johnson, P. L., Bassenne, M., and Moin, P., 2020, "Turbophoresis of Small Inertial Particles: Theoretical Considerations and Application to Wall-Modelled Large-Eddy Simulations," J. Fluid Mech., **883**, pp. 1–38.
[133] Afkhami, M., Hassanpour, A., Fairweather, M., and Njobuenwu, D. O., 2015, "Fully Coupled LES-DEM of Particle Interaction and Agglomeration in a Turbulent Channel Flow," Comput. Chem. Eng., **78**, pp. 24–38.
[134] Sommerfeld, M., 2001, "Validation of a Stochastic Lagrangian Modelling Approach for Inter-Particle Collisions in Homogeneous Isotropic Turbulence," Int. J. Multiphase Flow, **27**(10), pp. 1829–1858.
[135] Hoomans, B. P. B., Kuipers, J. A., Briels, W. J., and Swaaij, W. P. M. V. A. N., 1996, "Discrete Particle Simulation of Bubble and Slug Formation in a 2D Gas-Fluidised Bed: A Hard-Sphere Approach," Chem. Eng. Sci., **51**(1), pp. 99–118.
[136] Chen, M., Kontomaris, K., and McLaughlin, J. B., 1999, "Direct Numerical Simulation of Droplet Collisions in a Turbulent Channel Flow. Part I: Collision Algorithm," Int. J. Multiphase Flow, **24**(7), pp. 1079–1103.
[137] Li, Y., McLaughlin, J. B., Kontomaris, K., and Portela, L., 2001, "Numerical Simulation of Particle-Laden Turbulent Channel Flow," Phys. Fluids, **13**(10), pp. 2957–2967.
[138] Fede, P., and Simonin, O., 2006, "Numerical Study of the Subgrid Fluid Turbulence Effects on the Statistics of Heavy Colliding Particles," Phys. Fluids, **18**(4), p. 045103.
[139] Mallouppas, G., and van Wachem, B., 2013, "Large Eddy Simulations of Turbulent Particle-Laden Channel Flow," Int. J. Multiphase Flow, **54**, pp. 65–75.
[140] Cundall, P. A., and Strack, O., 1979, "A Discrete Numerical Model for Granular Assemblies," Geotechnique, **29**(1), pp. 47–65.
[141] Luo, K., Wu, F., Qiu, K., Wang, Z., and Fan, J., 2015, "Effects of Preferential Concentration on Collision and Erosion Between Solid Particles and Tube Bank in a Duct Flow," Int. J. Heat Mass Transfer, **83**, pp. 372–381.
[142] Luo, K., Tan, J., Wang, Z., and Fan, J., 2015, "Particle-Resolved Direct Numerical Simulation of Gas-Solid Dynamics in Experimental Fluidized Beds," AICHE J., **61**(3), pp. 857–866.
[143] Costa, P., Boersma, B. J., Westerweel, J., and Breugem, W. P., 2015, "Collision Model for Fully Resolved Simulations of Flows Laden With Finite-Size Particles," Phys. Rev. E - Stat., Nonlinear, Soft Mat. Phys., **92**(5), pp. 1–14.
[144] Deen, N. G., Van Sint Annaland, M., Van der Hoef, M. A., and Kuipers, J. A., 2007, "Review of Discrete Particle Modeling of Fluidized Beds," Chem. Eng. Sci., **62**(1–2), pp. 28–44.
[145] Wiesner, V. L., Vempati, U. K., and Bansal, N. P., 2016, "High Temperature Viscosity of Calcium-Magnesium-Aluminosilicate Glass From Synthetic Sand," Scr. Mater., **124**, pp. 189–192.
[146] Yarin, A., 2006, "Drop Impact Dynamics: Splashing, Spreading, Receding, Bouncing…," Annu. Rev. Fluid Mech., **38**(1), pp. 159–192.
[147] Moreira, A. L. N., Moita, A. S., and Panão, M. R., 2010, "Advances and Challenges in Explaining Fuel Spray Impingement: How Much of Single Droplet Impact Research is Useful?," Prog. Energy Combust. Sci., **36**(5), pp. 554–580.
[148] Josserand, C., and Thoroddsen, S., 2016, "Drop Impact on a Solid Surface," Annu. Rev. Fluid Mech., **48**(1), pp. 365–391.
[149] Liang, G., and Mudawar, I., 2017, "Review of Drop Impact on Heated Walls," Int. J. Heat Mass Transfer, **106**, pp. 103–126.
[150] de Gennes, P. G., 1985, "Wetting: Statics and Dynamics," Rev. Mod. Phys., **57**(3), pp. 827–863.
[151] Rioboo, R., 2001, "Impact de Gouttes Sur Surfaces Solides et Seches," These de doctorat, Paris 6, Jan.
[152] Xu, L., 2007, "Liquid Drop Splashing on Smooth, Rough, and Textured Surfaces," Phys. Rev. E, **75**(5), p. 056316.
[153] Gao, M., Kong, P., Zhang, L.-X., and Liu, J.-N., 2017, "An Experimental Investigation of Sessile Droplets Evaporation on Hydrophilic and Hydrophobic Heating Surface With Constant Heat Flux," Int. Commun. Heat Mass Transfer, **88**, pp. 262–268.
[154] Yun, S., and Lim, G., 2014, "Ellipsoidal Drop Impact on a Solid Surface for Rebound Suppression," J. Fluid Mech., **752**, pp. 266–281.
[155] Pumphrey, H. C., and Elmore, P. A., 1990, "The Entrainment of Bubbles by Drop Impacts," J. Fluid Mech., **220**, pp. 539–567.
[156] Chandra, S., and Avedisian, C. T., 1991, "On the Collision of a Droplet With a Solid Surface," Proc. R. Soc. London. Ser. A: Math. Phys. Sci., **432**(1884), pp. 13–41.
[157] de Ruiter, J., Mugele, F., and van den Ende, D., 2015, "Air Cushioning in Droplet Impact. I. Dynamics of Thin Films Studied by Dual Wavelength Reflection Interference Microscopy," Phys. Fluids, **27**(1), p. 012104.
[158] Kolinski, J. M., Mahadevan, L., and Rubinstein, S. M., 2014, "Drops Can Bounce From Perfectly Hydrophilic Surfaces," EPL (Europhys. Lett.), **108**(2), p. 24001.
[159] Rioboo, R., Marengo, M., and Tropea, C., 2002, "Time Evolution of Liquid Drop Impact Onto Solid, Dry Surfaces," Exp. Fluids, **33**(1), pp. 112–124.
[160] Yarin, A. L., and Weiss, D. A., 1995, "Impact of Drops on Solid Surfaces: Self-Similar Capillary Waves, and Splashing as a New Type of Kinematic Discontinuity," J. Fluid Mech., **283**, pp. 141–173.
[161] Roisman, I. V., Horvat, K., and Tropea, C., 2006, "Spray Impact: Rim Transverse Instability Initiating Fingering and Splash, and Description of a Secondary Spray," Phys. Fluids, **18**(10), p. 102104.
[162] Mao, T., Kuhn, D. C. S., and Tran, H., 1997, "Spread and Rebound of Liquid Droplets Upon Impact on Flat Surfaces," AIChE J., **43**(9), pp. 2169–2179.
[163] Moita, A. S., and Moreira, A. L. N., 2007, "Drop Impacts Onto Cold and Heated Rigid Surfaces: Morphological Comparisons, Disintegration Limits and Secondary Atomization," Int. J. Heat Fluid Flow, **28**(4), pp. 735–752.

[164] Driscoll, M. M., Stevens, C. S., and Nagel, S. R., 2010, "Thin Film Formation During Splashing of Viscous Liquids," Phys. Rev. E, **82**(3), p. 036302.
[165] Xu, L., Zhang, W. W., and Nagel, S. R., 2005, "Drop Splashing on a Dry Smooth Surface," Phys. Rev. Lett., **94**(18), p. 184505.
[166] Vander Wal, R. L., Berger, G. M., and Mozes, S. D., 2006, "The Combined Influence of a Rough Surface and Thin Fluid Film Upon the Splashing Threshold and Splash Dynamics of a Droplet Impacting Onto Them," Exp. Fluids, **40**(1), pp. 23–32.
[167] Tropea, C., and Marengo, M., 1999, "The Impact of Drops on Walls Films," Multiphase Sci. Technol., **11**(1), pp. 19–36.
[168] Cossali, G. E., Coghe, A., and Marengo, M., 1997, "The Impact of a Single Drop on a Wetted Solid Surface," Exp. Fluids, **22**(6), pp. 463–472.
[169] Liang, G., Shen, S., Guo, Y., and Zhang, J., 2016, "Boiling From Liquid Drops Impact on a Heated Wall," Int. J. Heat Mass Transfer, **100**, pp. 48–57.
[170] Makino, K., and Michiyopshi, I., 1979, "Effects of the Initial Size of Water Droplet on Its Evaporation on Heated Surfaces," Int. J. Heat Mass Transfer, **22**(6), pp. 979–981.
[171] Nishio, S., and Hirata, M., 1978, "Direct Contact Phenomenon Between a Liquid Droplet and High Temperature Solid Surface," 6th International Heat Transfer Conference, Toronto, ON, Canada, Aug. 7–11, pp. 245–250.
[172] Celata, G. P., Cumo, M., Mariani, A., and Zummo, G., 2006, "Visualization of the Impact of Water Drops on a Hot Surface: Effect of Drop Velocity and Surface Inclination," Heat Mass Transfer, **42**(10), pp. 885–890.
[173] Bernardin, J. D., and Mudawar, I., 2004, "A Leidenfrost Point Model for Impinging Droplets and Sprays," ASME J. Heat Transfer, **126**(2), pp. 272–278.
[174] Rafaï, S., Bonn, D., and Boudaoud, A., 2004, "Spreading of non-Newtonian Fluids on Hydrophilic Surfaces," J. Fluid Mech., **513**, pp. 77–85.
[175] Bartolo, D., Boudaoud, A., Narcy, G., and Bonn, D., 2007, "Dynamics of Non-Newtonian Droplets," Phys. Rev. Lett., **99**(17), p. 174502.
[176] Moon, J. H., Kim, D. Y., and Lee, S. H., 2014, "Spreading and Receding Characteristics of a non-Newtonian Droplet Impinging on a Heated Surface," Exp. Therm. Fluid Sci., **57**, pp. 94–101.
[177] Bergeron, V., Bonn, D., Martin, J. Y., and Vovelle, L., 2000, "Controlling Droplet Deposition With Polymer Additives," Nature, **405**(6788), pp. 772–775.
[178] Zang, D., Zhang, W., Song, J., Chen, Z., Zhang, Y., Geng, X., and Chen, F., 2014, "Rejuvenated Bouncing of non-Newtonian Droplet Via Nanoparticle Enwrapping," Appl. Phys. Lett., **105**(23), p. 231603.
[179] Han, Z., Xu, Z., and Trigui, N., 2000, "Spray/Wall Interaction Models for Multidimensional Engine Simulation," Int. J. Engine Res., **1**(1), pp. 127–146.
[180] Cossali, G., Marengo, M., and Santini, M., 2004, "Drop Array Impacts on Heated Surfaces: Secondary Atomization Characteristics," 19th Annual Meeting of ILASS, Nottingham, UK, 06-08/09/2004, ILASS Europe, pp. 1–8.
[181] Barnes, H., Hardalupas, Y., Taylor, A., Wilkins, J., et alet al 1999, "An Investigation of the Interaction Between Two Adjacent Impinging Droplets," Proceedings of the 15th International Conference on Liquid Atomisation and Spray Systems (ILASS), Toulouse, pp. 1–7.
[182] Moreira, A., and Panao, M. O., 2011, "Spray-Wall Impact," Handbook of Atomization and Sprays, Springer Science and Business Media, LLC, Boston, MA, pp. 441–455.
[183] Chaussonet, G., Bravo, L., Flatau, A., Koch, R., and Bauer, H.-J., 2020, "Smoothed Particle Hydrodynamics Simulation of High Velocity Impact Dynamics of Molten Sand Particles," Energies, **13**(19), p. 5134.
[184] Shikhmurzaev, Y. D., 1997, "Moving Contact Lines in Liquid/Liquid/Solid Systems," J. Fluid Mech., **334**, pp. 211–249.
[185] Haley, P. J., and Miksis, M. J., 1991, "The Effect of the Contact Line on Droplet Spreading," J. Fluid Mech., **223**(1), pp. 57–81.
[186] Bussmann, M., Mostaghimi, J., and Chandra, S., 1999, "On a Three-Dimensional Volume Tracking Model of Droplet Impact," Phys. Fluids, **11**(6), pp. 1406–1417.
[187] Bussmann, M., Chandra, S., and Mostaghimi, J., 2000, "Modeling the Splash of a Droplet Impacting a Solid Surface," Phys. Fluids, **12**(12), pp. 3121–3132.
[188] Mehdi-Nejad, V., Mostaghimi, J., and Chandra, S., 2003, "Air Bubble Entrapment Under an Impacting Droplet," Phys. Fluids, **15**(1), pp. 173–183.
[189] Šikalo, Š., Wilhelm, H.-D., Roisman, I. V., Jakirlić, S., and Tropea, C., 2005, "Dynamic Contact Angle of Spreading Droplets: Experiments and Simulations," Phys. Fluids, **17**(6), p. 062103.
[190] Šikalo, Š., Tropea, C., and Ganić, E. N., 2005, "Impact of Droplets Onto Inclined Surfaces," J. Colloid Interface Sci., **286**(2), pp. 661–669.
[191] Nikolopoulos, N., Theodorakakos, A., and Bergeles, G., 2005, "Normal Impingement of a Droplet Onto a Wall Film: A Numerical Investigation," Int. J. Heat Fluid Flow, **26**(1), pp. 119–132.
[192] Shetabivash, H., Ommi, F., and Heidarinejad, G., 2014, "Numerical Analysis of Droplet Impact Onto Liquid Film," Phys. Fluids, **26**(1), p. 012102.
[193] Li, R., Ninokata, H., and Mori, M., 2011, "A Numerical Study of Impact Force Caused by Liquid Droplet Impingement Onto a Rigid Wall," Prog. Nucl. Energy, **53**(7), pp. 881–885.
[194] Strotos, G., Gavaises, M., Theodorakakos, A., and Bergeles, G., 2008, "Numerical Investigation of the Cooling Effectiveness of a Droplet Impinging on a Heated Surface," Int. J. Heat Mass Transfer, **51**(19–20), pp. 4728–4742.
[195] Kim, D., Ivey, C., Frank, H., and Bravo, L., 2020, "An Efficient High-Resolution Volume-of-Fluid Method With Low Numerical Diffusion on Unstructured Grids," J. Comput. Phys., epub.
[196] Sethian, J. A., 1996, "A Fast Marching Level Set Method for Monotonically Advancing Fronts," Proc. Natl. Acad. Sci., **93**(4), pp. 1591–1595.
[197] Spelt, P. D. M., 2005, "A Level-Set Approach for Simulations of Flows With Multiple Moving Contact Lines With Hysteresis," J. Comput. Phys., **207**(2), pp. 389–404.
[198] Caviezel, D., Narayanan, C., and Lakehal, D., 2008, "Adherence and Bouncing of Liquid Droplets Impacting on Dry Surfaces," Microfluid. Nanofluid., **5**(4), pp. 469–478.
[199] Yokoi, K., 2011, "Numerical Studies of Droplet Splashing on a Dry Surface: Triggering a Splash With the Dynamic Contact Angle," Soft Matter, **7**(11), pp. 5120–5123.
[200] Patil, N. D., Gada, V. H., Sharma, A., and Bhardwaj, R., 2016, "On Dual-Grid Level-Set Method for Contact Line Modeling During Impact of a Droplet on Hydrophobic and Superhydrophobic Surfaces," Int. J. Multiphase Flow, **81**, pp. 54–66.
[201] Shahmohammadi Beni, M., Zhao, J., and Yu, K. N., 2018, "Investigation of Droplet Behaviors for Spray Cooling Using Level Set Method," Ann. Nucl. Energy, **113**, pp. 162–170.
[202] Yokoi, K., 2008, "A Numerical Method for Free-Surface Flows and Its Application to Droplet Impact on a Thin Liquid Layer," J. Sci. Comput., **35**(2–3), pp. 372–396.
[203] Selvam, R. P., Lin, L., and Ponnappan, R., 2006, "Direct Simulation of Spray Cooling: Effect of Vapor Bubble Growth and Liquid Droplet Impact on Heat Transfer," Int. J. Heat Mass Transfer, **49**(23–24), pp. 4265–4278.
[204] Ding, H., and Spelt, P. D. M., 2007, "Inertial Effects in Droplet Spreading: A Comparison Between Diffuse-Interface and Level-Set Simulations," J. Fluid Mech., **576**, pp. 287–296.
[205] Selvam, R. P., Bhaskara, S., Balda, J. C., Barlow, F., and Elshabini, A., 2005, "Computer Modeling of Liquid Droplet Impact on Heat Transfer During Spray Cooling," pp. 179–188.
[206] Chatzikyriakou, D., Walker, S. P., Hewitt, G. F., Narayanan, C., and Lakehal, D., 2009, "Comparison of Measured and Modelled Droplet–Hot Wall Interactions," Appl. Therm. Eng., **29**(7), pp. 1398–1405.
[207] Pournaderi, P., and Pishevar, A. R., 2012, "A Numerical Investigation of Droplet Impact on a Heated Wall in the Film Boiling Regime," Heat Mass Transfer, **48**(9), pp. 1525–1538.
[208] Choi, M., Son, G., and Shim, W., 2017, "Numerical Simulation of Droplet Impact and Evaporation on a Porous Surface," Int. Commun. Heat Mass Transfer, **80**, pp. 18–29.
[209] Sussman, M., and Puckett, E. G., 2000, "A Coupled Level Set and Volume-of-Fluid Method for Computing 3D and Axisymmetric Incompressible Two-Phase Flows," J. Comput. Phys., **162**(2), pp. 301–337.
[210] Guo, Y., Wei, L., Liang, G., and Shen, S., 2014, "Simulation of Droplet Impact on Liquid Film With CLSVOF," Int. Commun. Heat Mass Transfer, **53**, pp. 26–33.
[211] Liang, G., Mu, X., Guo, Y., and Shen, S., 2016, "Flow and Heat Transfer During a Single Drop Impact on a Liquid Film," Numer. Heat Transfer, Part B: Fundam., **69**(6), pp. 575–582.
[212] Hong, W., and Wang, Y., 2017, "A Coupled Level Set and Volume-of-Fluid Simulation for Heat Transfer of the Double Droplet Impact on a Spherical Liquid Film," Numer. Heat Transfer, Part B: Fundam., **71**(4), pp. 359–371.
[213] Li, D., Duan, X., Zheng, Z., and Liu, Y., 2018, "Dynamics and Heat Transfer of a Hollow Droplet Impact on a Wetted Solid Surface," Int. J. Heat Mass Transfer, **122**, pp. 1014–1023.
[214] Shan, X., and Chen, H., 1993, "Lattice Boltzmann Model for Simulating Flows With Multiple Phases and Components," Phys. Rev. E, **47**(3), pp. 1815–1819.
[215] Swift, M. R., Orlandini, E., Osborn, W. R., and Yeomans, J. M., 1996, "Lattice Boltzmann Simulations of Liquid-Gas and Binary Fluid Systems," Phys. Rev. E, **54**(5), pp. 5041–5052.
[216] He, X., Chen, S., and Zhang, R., 1999, "A Lattice Boltzmann Scheme for Incompressible Multiphase Flow and Its Application in Simulation of Rayleigh–Taylor Instability," J. Comput. Phys., **152**(2), pp. 642–663.
[217] Chen, L., Kang, Q., Mu, Y., He, Y.-L., and Tao, W.-Q., 2014, "A Critical Review of the Pseudopotential Multiphase Lattice Boltzmann Model: Methods and Applications," Int. J. Heat Mass Transfer, **76**, pp. 210–236.
[218] Liang, H., Li, Y., Chen, J., and Xu, J., 2019, "Axisymmetric Lattice Boltzmann Model for Multiphase Flows With Large Density Ratio," Int. J. Heat Mass Transfer, **130**, pp. 1189–1205.
[219] Mukherjee, S., and Abraham, J., 2007, "Investigations of Drop Impact on Dry Walls With a lattice-Boltzmann Model," J. Colloid Interface Sci., **312**(2), pp. 341–354.
[220] Hao, L., and Cheng, P., 2009, "Lattice Boltzmann Simulations of Liquid Droplet Dynamic Behavior on a Hydrophobic Surface of a Gas Flow Channel," J. Power Sources, **190**(2), pp. 435–446.
[221] Gupta, A., and Kumar, R., 2010, "Droplet Impingement and Breakup on a Dry Surface," Comput. Fluids, **39**(9), pp. 1696–1703.
[222] Shen, S., Bi, F., and Guo, Y., 2012, "Simulation of Droplets Impact on Curved Surfaces With Lattice Boltzmann Method," Int. J. Heat Mass Transfer, **55**(23–24), pp. 6938–6943.
[223] Zhang, D., Papadikis, K., and Gu, S., 2014, "Three-Dimensional Multi-Relaxation Time lattice-Boltzmann Model for the Drop Impact on a Dry Surface at Large Density Ratio," Int. J. Multiphase Flow, **64**, pp. 11–18.
[224] Raman, K. A., Jaiman, R. K., Lee, T.-S., and Low, H.-T., 2016, "Lattice Boltzmann Simulations of Droplet Impact Onto Surfaces With Varying Wettabilities," Int. J. Heat Mass Transfer, **95**, pp. 336–354.
[225] Raman, K., Jaiman, R., Lee, T., and Low, H., 2015, "On the Dynamics of Crown Structure in Simultaneous Two Droplets Impact Onto Stationary and Moving Liquid Film," Comput. Fluids, **107**, pp. 285–300.
[226] Taghilou, M., and Rahimian, M. H., 2014, "Lattice Boltzmann Model for Thermal Behavior of a Droplet on the Solid Surface," Int. J. Therm. Sci., **86**, pp. 1–11.

[227] Shadloo, M. S., Oger, G., and Le Touzé, D., 2016, "Smoothed Particle Hydrodynamics Method for Fluid Flows, Towards Industrial Applications: Motivations, Current State, and Challenges," Comput. Fluids, **136**, pp. 11–34.
[228] Brackbill, J. U., Kothe, D. B., and Zemach, C., 1992, "A Continuum Method for Modeling Surface Tension," J. Comput. Phys., **100**(2), pp. 335–354.
[229] Adami, S., Hu, X. Y., and Adams, N. A., 2010, "A New Surface-Tension Formulation for Multi-Phase SPH Using a Reproducing Divergence Approximation," J. Comput. Phys., **229**(13), pp. 5011–5021.
[230] Barcarolo, D. A., Le Touzé, D., Oger, G., and de Vuyst, F., 2014, "Adaptive Particle Refinement and Derefinement Applied to the Smoothed Particle Hydrodynamics Method," J. Comput. Phys., **273**, pp. 640–657.
[231] Li, D., Bai, L., Li, L., and Zhao, M., 2014, "SPH Modeling of Droplet Impact on Solid Boundary," Trans. Tianjin Univ., **20**(2), pp. 112–117.
[232] Shigorina, E., Kordilla, J., and Tartakovsky, A. M., 2017, "Smoothed Particle Hydrodynamics Study of the Roughness Effect on Contact Angle and Droplet Flow," Phys. Rev. E, **96**(3), p. 033115.
[233] Xu, X., Ouyang, J., Jiang, T., and Li, Q., 2014, "Numerical Analysis of the Impact of Two Droplets With a Liquid Film Using an Incompressible SPH Method," J. Eng. Math., **85**(1), pp. 35–53.
[234] Ma, T., Zhang, F., Liu, H., and Yao, M., 2017, "Modeling of Droplet/Wall Interaction Based on SPH Method," Int. J. Heat Mass Transfer, **105**, pp. 296–304.
[235] Yang, X., Dai, L., and Kong, S.-C., 2017, "Simulation of Liquid Drop Impact on Dry and Wet Surfaces Using SPH Method," Proc. Combust. Inst., **36**(2), pp. 2393–2399.
[236] Yang, X., and Kong, S.-C., 2018, "3D Simulation of Drop Impact on Dry Surface Using SPH Method," Int. J. Comput. Methods, **15**(3), p. 1850011.
[237] Ray, M., Yang, X., Kong, S., Bravo, L., and Kweon, C., 2016, "High Fidelity Simulation of Drop Collision and Vapor-Liquid Equilibrium of Van Der Waals Fluids," Proc. Combust. Inst., **36**, pp. 2385–2392.
[238] Yang, X., Ray, M., Kong, S.-C., and Kweon, C.-B. M., 2019, "SPH Simulation of Fuel Drop Impact on Heated Surfaces," Proc. Combust. Inst., **37**(3), pp. 3279–3286.
[239] Jiang, T., Ouyang, J., Yang, B., and Ren, J., 2010, "The SPH Method for Simulating a Viscoelastic Drop Impact and Spreading on an Inclined Plate," Comput. Mech., **45**(6), pp. 573–583.
[240] Xu, X., Ouyang, J., Jiang, T., and Li, Q., 2012, "Numerical Simulation of 3D-Unsteady Viscoelastic Free Surface Flows by Improved Smoothed Particle Hydrodynamics Method," J. Non-Newtonian Fluid Mech., **177–178**, pp. 109–120.
[241] Mirjalili, S., Jain, S. S., and Dodd, M., 2017, "Interface-Capturing Methods for Two-Phase Flows: An Overview and Recent Developments," Cent. Turbul. Res. Annu. Res. Briefs, **2017**, pp. 117–135.
[242] Ding, H., Spelt, P. D., and Shu, C., 2007, "Diffuse Interface Model for Incompressible Two-Phase Flows With Large Density Ratios," J. Comput. Phys., **226**(2), pp. 2078–2095.
[243] Mirjalili, S., Ivey, C. B., and Mani, A., 2016, "Cost and Accuracy Comparison Between the Diffuse Interface Method and the Geometric Volume of Fluid Method for Simulating Two-Phase Flows," APS Division of Fluid Dynamics Meeting Abstracts, American Physical Society 69th Annual Division of Fluid Dynamics Annual Meeting, Portland, OR, Nov. 20–22, pp. R29–008.
[244] Mirjalili, S., and Mani, A., 2021, "Consistent, Energy-Conserving Momentum Transport for Simulations of Two-Phase Flows Using the Phase Field Equations," J. Comput. Phys., **426**, p. 109918.
[245] Zhang, Q., Qian, T.-Z., and Wang, X.-P., 2016, "Phase Field Simulation of a Droplet Impacting a Solid Surface," Phys. Fluids, **28**(2), p. 022103.
[246] Shen, M., Li, B. Q., Yang, Q., Bai, Y., Wang, Y., Zhu, S., Zhao, B., Li, T., and Hu, Y., 2019, "A Modified Phase-Field Three-Dimensional Model for Droplet Impact With Solidification," Int. J. Multiphase Flow, **116**, pp. 51–66.
[247] Ahmadi-Befrui, B., Uchil, N., Gosman, A. D., and Issa, R. I., 1996, "Modeling and Simulation of Thin Liquid Films Formed by Spray-Wall Interaction," SAE Paper No. 960627.
[248] Bai, C., and Gosman, A. D., 1995, "Development of Methodology for Spray Impingement Simulation," SAE Paper No. 950283.
[249] Stanton, D. W., and Rutland, C. J., 1996, "Modeling Fuel Film Formation and Wall Interaction in Diesel Engines," SAE Paper No. 960628.
[250] O'Rourke, P., and Amsden, A. A., 1996, "A Particle Numerical Model for Wall Film Dynamics in Port-Injected Engines," SAE Paper No. 961961.
[251] O'Rourke, P. J., and Amsden, A. A., 2000, "A Spray/Wall Interaction Submodel for the KIVA-3 Wall Film Model," SAE Paper No. 2000-01-0271.
[252] Zhang, Y., Jia, M., Liu, H., Xie, M., Wang, T., and Zhou, L., 2014, "Development of a New Spray/Wall Interaction Model for Diesel Spray Under PCCI-Engine Relevant Conditions," Atomization Sprays, **24**(1), pp. 41–80.
[253] Ma, T., Feng, L., Wang, H., Liu, H., and Yao, M., 2017, "A Numerical Study of Spray/Wall Impingement Based on Droplet Impact Phenomenon," Int. J. Heat Mass Transfer, **112**, pp. 401–412.
[254] Chaussonnet, G., 2014, "Modeling of Liquid Film and Breakup Phenomena in Large-Eddy Simulations of Aeroengines Fueled by Airblast Atomizers," Ph.D. thesis, Institut National Polytechnique, Toulouse, France.
[255] Milanez, M., and Naterer, G. F., 2005, "Eulerian Cross-Phase Diffusive Effects on Impinging Droplets and Phase Change Heat Transfer," Int. Commun. Heat Mass Transfer, **32**(3–4), pp. 286–295.
[256] Honsek, R., Habashi, W. G., and Aubé, M. S., 2008, "Eulerian Modeling of in-Flight Icing Due to Supercooled Large Droplets," J. Aircr., **45**(4), pp. 1290–1296.
[257] Bilodeau, D. R., Habashi, W. G., Fossati, M., and Baruzzi, G. S., 2015, "Eulerian Modeling of Supercooled Large Droplet Splashing and Bouncing," J. Aircr., **52**(5), pp. 1611–1624.
[258] Mundo, C., Sommerfeld, M., and Tropea, C., 1995, "Droplet-Wall Collisions: Experimental Studies of the Deformation and Breakup Process," Int. J. Multiphase Flow, **21**(2), pp. 151–173.
[259] Rosa, N. G., Villedieu, P., Dewitte, J., and Lavergne, G., 2006, "A New Droplet-Wall Interaction Model," Proceedings of the 10th International Conference on Liquid Atomization and Spray Systems, pp. 29–32. Tokyo, Japan, Vol. 27.
[260] Staat, H. J. J., Tran, T., Geerdink, B., Riboux, G., Sun, C., Gordillo, J. M., and Lohse, D., 2015, "Phase Diagram for Droplet Impact on Superheated Surfaces," J. Fluid Mech., **779**, p. R3.
[261] Wachters, L. H. J., and Westerling, N. A. J., 1966, "The Heat Transfer From a Hot Wall to Impinging Water Drops in the Spheroidal State," Chem. Eng. Sci., **21**(11), pp. 1047–1056.
[262] Wang, A.-B., Chen, C.-C., and Hwang, W.-C., 2002, "On Some New Aspects of Splashing Impact of Drop-Liquid Surface Interactions," *Drop-Surface Interactions*, M. Rein, ed., CISM International Centre for Mechanical Sciences, Springer, Vienna, Austria, pp. 303–306.
[263] Chen, R.-H., Chiu, S.-L., and Lin, T.-H., 2007, "On the Collision Behaviors of a Diesel Drop Impinging on a Hot Surface," Exp. Therm. Fluid Sci., **32**(2), pp. 587–595.
[264] Pan, K. L., and Law, C. K., 2007, "Dynamics of Droplet–Film Collision," J. Fluid Mech., **587**, pp. 1–22.
[265] Madejski, J., 1976, "Solidification of Droplets on a Cold Surface," Int. J. Heat Mass Transfer, **19**(9), pp. 1009–1013.
[266] Yang, W. J., 1975, "Theory on Vaporization and Combustion of Liquid Drops of Pure Substances and Binary Mixtures on Heated Surfaces," Instiute of Space and Aeronautical Science, University of Tokyo, Report No. 535, pp. 423–455.
[267] Pasandideh-Fard, M., Qiao, Y. M., Chandra, S., and Mostaghimi, J., 1996, "Capillary Effects During Droplet Impact on a Solid Surface," Phys. Fluids, **8**(3), pp. 650–659.
[268] Vadillo, D. C., Soucemarianadin, A., Delattre, C., and Roux, D. C. D., 2009, "Dynamic Contact Angle Effects Onto the Maximum Drop Impact Spreading on Solid Surfaces," Phys. Fluids, **21**(12), p. 122002.
[269] Roisman, I. V., 2009, "Inertia Dominated Drop Collisions. II. An Analytical Solution of the Navier–Stokes Equations for a Spreading Viscous Film," Phys. Fluids, **21**(5), p. 052104.
[270] Scheller, B. L., and Bousfield, D. W., 1995, "Newtonian Drop Impact With a Solid Surface," AIChE J., **41**(6), pp. 1357–1367.
[271] Seo, J., Lee, J. S., Kim, H. Y., and Yoon, S. S., 2015, "Empirical Model for the Maximum Spreading Diameter of Low-Viscosity Droplets on a Dry Wall," Exp. Therm. Fluid Sci., **61**, pp. 121–129.
[272] Mundo, C., Sommerfeld, M., and Tropea, C., 1998, "On the Modeling of Liquid Sprays Impinging on Surfaces," Atomization Sprays, **8**(6), pp. 625–652.
[273] Samenfink, W., Elsäßer, A., Dullenkopf, K., and Wittig, S., 1999, "Droplet Interaction With Shear-Driven Liquid Films: Analysis of Deposition and Secondary Droplet Characteristics," Int. J. Heat Fluid Flow, **20**(5), pp. 462–469.
[274] Senda, J., and Fujimoto, H. G., 1999, "Multidimensional Modeling of Impinging Sprays on the Wall in Diesel Engines," ASME Appl. Mech. Rev., **52**(4), pp. 119–138.
[275] Bai, C. X., Rusche, H., and Gosman, A. D., 2002, "Modeling of Gasoline Spray Impingement," Atomization Sprays, **12**(1–3), pp. 1–3.
[276] Kuhnke, D., 2004, "Spray/wall interaction modelling by dimensionless data analysis,". Ph.D. thesis, Techn. Univ., Darmstadt, Germany.
[277] Kalantari, D., and Tropea, C., 2007, "Spray Impact Onto Flat and Rigid Walls: Empirical Characterization and Modelling," Int. J. Multiphase Flow, **33**(5), pp. 525–544.
[278] Eckhause, J. E., and Reitz, R. D., 1995, "Modeling Heat Transfer to Impinging Fuel Spray in Direct-Injection Engines," Atomization Sprays, **5**(2), pp. 213–242.
[279] Rybicki, J. R., and Mudawar, I., 2006, "Single-Phase and Two-Phase Cooling Characteristics of Upward-Facing and Downward-Facing Sprays," Int. J. Heat Mass Transfer, **49**(1–2), pp. 5–16.
[280] Arcoumanis, C., and Chang, J. C., 1993, "Heat Transfer Between a Heated Plate and an Impinging Transient Diesel Spray," Exp. Fluids, **16**(2), pp. 105–119.
[281] Panão, M. R. O., and Moreira, A. L. N., 2007, "Interpreting the Influence of Fuel Spray Impact on Mixture Preparation for HCCI Combustion With Port-Fuel Injection," Proc. Combust. Inst., **31**(2), pp. 2205–2213.
[282] Tabakoff, W., Hamed, A., and Murugan, D. M., 1996, "Effect of Target Materials on the Particle Restitution Characteristics for Turbomachinery Application," J. Propuls. Power, **12**(2), pp. 260–266.
[283] Walsh, W. S., Thole, K. A., and Joe, C., 2006, "Effects of Sand Ingestion on the Blockage of Film-Cooling Holes," ASME Paper No. GT2006-90067.
[284] Zagnoli, D., Prenter, R., Ameri, A., and Bons, J. P., 2015, "Numerical Study of Deposition in a Full Turbine Stage Using Steady and Unsteady Methods," ASME Paper No. GT2015-43613.
[285] Ghoshal, A., Walock, M. J., Murugan, M., Hofmeister-Mock, C., Bravo, L., Pepi, M., Nieto, A., Wright, A., Luo, J., Jain, N., Flatau, A., and Frehenbacher, L., 2019, "Governing Parameters Influencing CMAS Adhesion and Infiltration Into Environmental/Thermal Barrier Coatings in Gas Turbine Engines," ASME Paper No. GT2019-92000.
[286] Bravo, L., Jain, N., Khare, P., Murugan, M., Ghoshal, A., and Flatau, A., 2020, "Physical Aspects of CMAS Particle Dynamics and Deposition in Gas Turbine Engines," J. Mater. Res., **35**, pp. 2249–2259.

[287] Hamed, A., and Kuhn, T. P., 1995, "Effects of Variational Particle Restitution Characteristics on Turbomachinery Erosion," ASME J. Eng. Gas Turbines Power, **117**(3), pp. 432–440.
[288] Hamed, A., Jun, Y. D., and Yeuan, J. J., 1995, "Particle Dynamics Simulations in Inlet Separator With an Experimentally Based Bounce Model," J. Propuls. Power, **11**(2), pp. 230–235.
[289] Brach, R. M., and Dunn, P. F., 1992, "A Mathematical Model of the Impact and Adhesion of Microspheres," Aerosol Sci. Technol., **16**(1), pp. 51–64.
[290] Lawrence, M., Casaday, B., Lageman, D., Bons, J., and Whitaker, S., 2013, "Computational Modeling of High Temperature Deposition in Gas Turbine Engines With Experimental Validation," AIAA Paper No. AIAA 2013-1112.
[291] Barker, B. J., 2010, "Simulation of Coal Ash Deposition on Modern Turbine Nozzle Guide Vanes," M.S. thesis, The Ohio State University, Columbus, OH.
[292] Ai, W., and Fletcher, T. H., 2012, "Computational Analysis of Conjugate Heat Transfer and Particulate Deposition on a High Pressure Turbine Vane," ASME J. Turbomach, **134**(4), p. 041020.
[293] Sreedharan, S. S., and Tafti, D. K., 2010, "Composition Dependent Model for the Prediction of Syngas Ash Deposition With Application to a Leading Edge Turbine Vane," ASME Paper No. GT2010-23655.
[294] Giordano, D., Russell, J. K., and Dingwell, D. B., 2008, "Viscosity of Magmatic Liquids: A Model," Earth Planet. Sci. Lett., **271**(1–4), pp. 123–134.
[295] Fluegel, A., 2007, "Glass Viscosity Calculation Based on a Global Statistical Modelling Approach," Glass Technol., **48**(1), p. 18.
[296] Bale, C. W., Bélisle, E., Chartrand, P., Decterov, S. A., Eriksson, G., Hack, K., Jung, I. H., Kang, Y. B., Melançon, J., Pelton, A. D., Robelin, C., and Petersen, S., 2009, "FactSage Thermochemical Software and Databases — Recent Developments," Calphad, **33**(2), pp. 295–311.
[297] N'dala, I., Cambier, F., Anseau, M. R., and Urbain, G., 1984, "Viscosity of Liquid Feldspars. Part I: Viscosity Measurements," Trans. J. Br. Ceram. Soc., **83**, pp. 108–112.
[298] Senior, C. L., and Srinivasachar, S., 1995, "Viscosity of Ash Particles in Combustion Systems for Prediction of Particle Sticking," Energy Fuels, **9**(2), pp. 277–283.
[299] Singh, S., and Tafti, D. K., 2016, "Prediction of Sand Transport and Deposition in a Two-Pass Internal Cooling Duct," ASME J. Eng. Gas Turbines Power, **138**(7), p. 72606.
[300] Singh, S., and Tafti, D., 2015, "Particle Deposition Model for Particulate Flows at High Temperatures in Gas Turbine Components," Int. J. Heat Fluid Flow, **52**, pp. 72–83.
[301] Jackson, R. L., and Green, I., 2005, "A Finite Element Study of Elasto-Plastic Hemispherical Contact," ASME J. Tribol., **127**(2), pp. 343–354.
[302] Webb, J., Casaday, B., Barker, B., Bons, J. P., Gledhill, A. D., and Padture, N. P., 2013, "Coal Ash Deposition on Nozzle Guide Vanes—Part I: Experimental Characteristics of Four Coal Ash Types," ASME J. Turbomach, **135**(2), pp. 021033–1–021033-9.
[303] Yu, K., and Tafti, D., 2016, "Impact Model for Micrometer-Sized Sand Particles," Powder Technol., **294**, pp. 11–21.
[304] Bons, J. P., Prenter, R., and Whitaker, S., 2016, "A Simple Physics-Based Model for Particle Rebound and Deposition in Turbomachinery," ASME J. Turbomach., **139**(8), p. 084009.
[305] Barker, B., Hsu, K., Varney, B., Boulanger, A., Hutchinson, J., and Ng, W. F., 2017, "An Experiment-Based Sticking Model for Heated Sand," ASME Paper No. GT2017-64421.
[306] Gislason, S. R., Hassenkam, T., Nedel, S., Bovet, N., Eiriksdottir, E. S., Alfredsson, H. A., Hem, C. P., Balogh, Z. I., Dideriksen, K., Oskarsson, N., Sigfusson, B., Larsen, G., and Stipp, S. L. S., 2011, "Characterization of Eyjafjallajökull Volcanic Ash Particles and a Protocol for Rapid Risk Assessment," PNAS, **108**(18), pp. 7307–7312.
[307] Taylor, H. E., and Lichte, F. E., 1980, "Chemical Composition of Mount St. Helens Volcanic Ash," Geophys. Res. Lett., **7**(11), pp. 949–952.
[308] Power Technologies Inc., 2012, "Arizona Test Dust MSDS," Power Technologies Inc., Arden Hills, MN, accessed May 26, 2021, https://www.powdertechnologyinc.com/msds/arizona-test-dust/
[309] Wood, C. A., Slater, S. L., Zonneveldt, M., Thornton, J., Armstrong, N., and Antoniou, R. A., 2017, "Characterisation of Dirt, Dust and Volcanic Ash: A Study on the Potential for Gas Turbine Engine Degradation, Dst-Group-tr-3367," Tech. rep., Aerospace Division, Defence Science Technology Group, Australian Government Department of Defense.
[310] Levi, C. G., Hutchinson, J. W., Vidal-Sétif, M.-H., and Johnson, C. A., 2012, "Environmental Degradation of Thermal-Barrier Coatings by Molten Deposits," MRS Bull., **37**(10), pp. 932–941.
[311] Braue, W., 2009, "Environmental Stability of the YSZ Layer and the YSZ/TGO Interface of an in-Service EB-PVD Coated High-Pressure Turbine Blade," J Mater Sci, **44**(7), pp. 1664–1675.
[312] Mechnich, P., and Braue, W., 2015, "Solid-State CMAS Corrosion of an EB-PVD YSZ Coated Turbine Blade: Zr4+ Partitioning and Phase Evolution," J. Am. Ceram. Soc., **98**(1), pp. 296–302.
[313] Zaleski, E. M., Ensslen, C., and Levi, C. G., 2015, "Melting and Crystallization of Silicate Systems Relevant to Thermal Barrier Coating Damage," J. Am. Ceram. Soc., **98**(5), pp. 1642–1649.
[314] Schön, J., 2011, *Physical Properties of Rocks: A Workbook*, Elsevier, The Netherlands.
[315] Munro, R. G., 2002, "Elastic Moduli Data for Polycrystalline Oxide Ceramics," NIST Interagency/Internal Report (NISTIR 6853), National Institute of Standards and Technology, Gaithersburg, MD, accessed July 14, 2021, https://nvlpubs.nist.gov/nistpubs/Legacy/IR/nistir6853.pdf
[316] Chicot, D., Mendoza, J., Zaoui, A., Louis, G., Lepingle, V., Roudet, F., and Lesage, J., 2011, "Mechanical Properties of Magnetite (Fe_3O_4), Hematite (α-Fe_2O_3) and Goethite (α-FeO·OH) by Instrumented Indentation and Molecular Dynamics Analysis," Mater. Chem. Phys., **129**(3), pp. 862–870.
[317] Collaboration: Authors and Editors of the Volumes III/17B-22A-41B, 1999, "Calcium Oxide (CaO) Young's, Shear and Bulk Modulus, Poisson's Ratio," *II-VI and I-VII Compounds; Semimagnetic Compounds*, O. Madelung, U. Rössler, and M. Schulz, eds., 41B, Springer-Verlag, Berlin/Heidelberg, pp. 1–2.
[318] Pabst, W., and Gregorová, E., 2013, "Elastic Properties of Silica Polymorphs – A Review," Ceram. Silikaty, **53**, pp. 167–184.
[319] Lakshtanov, D. L., Sinogeikin, S. V., and Bass, J. D., 2006, "High-Temperature Phase Transitions and Elasticity of Silica Polymorphs," Phys Chem Miner., **34**(1), pp. 11–22.
[320] Lorenz, J., Haas, J. L., Clynne, M. A., Schafer, C. M., Potter, R. W., Schafer, C. M., Tomkins, R. P. T., Shakoor, A., Hume, H. R., Yang, J. M., Li, H. H., and Matula, R. A., 1981, "Physical Properties Data for Rock Salt," accessed May 26, 2021, https://digital.library.unt.edu/ark:/67531/metadc13196/
[321] Rao, A. S. M., Narender, K., Rao, K. G. K., and Krishna, N. G., 2013, "Thermophysical Properties of NaCl, NaBr and NaF by γ-Ray Attenuation Technique," JMP, **4**(2), pp. 208–214.
[322] Meille, S., and Garboczi, E. J., 2001, "Linear Elastic Properties of 2D and 3D Models of Porous Materials Made From Elongated Objects," Modell. Simul. Mater. Sci. Eng., **9**(5), pp. 371–390.
[323] Singh, S., Tafti, D., Reagle, C., Delimont, J., Ng, W., and Ekkad, S., 2014, "Sand Transport in a Two Pass Internal Cooling Duct With Rib Turbulators," Int. J. Heat Fluid Flow, **46**, pp. 158–167.
[324] Richardson, J. H., and Sallee, G. P., and Smakula, F., 1979, "Causes of High Pressure Compressor Deterioration in Service," AIAA Paper No. 6.1979-1234.
[325] Lundgreen, R., Sacco, C., Prenter, R., and Bons, J. P., 2016, "Temperature Effects on Nozzle Guide Vane Deposition in a New Turbine Cascade Rig," ASME Paper No. GT2016-57560.
[326] Laycock, R., and Fletcher, T. H., 2015, "Independent Effects of Surface and Gas Temperature on Coal Fly Ash Deposition in Gas Turbines at Temperatures Up to 1400°C," ASME J. Eng. Gas Turbines Power, **138**(2), p. 021402.
[327] Crosby, J. M., Lewis, S., Bons, J. P., Ai, W. G., and Fletcher, T. H., 2008, "Effects of Temperature and Particle Size on Deposition in Land Based Turbines," ASME J. Eng. Gas Turbines Power, **130**(5), p. 051503.
[328] Reagle, C. J., Delimont, J. M., Ng, W. F., and Ekkad, S. V., 2013, "Study of Microparticle Rebound Characteristics Under High Temperature Conditions," ASME Paper No. GT2013-95083.
[329] Bons, J. P., Blunt, R., and Whitaker, S., 2015, "A Comparison of Techniques for Particle Rebound Measurement in Gas Turbine Applications," ASME Paper No. GT2015-43766.
[330] Whitaker, S. M., and Bons, J. P., 2015, "Evaluation of Elastic-Plastic Rebound Properties of Coal Fly Ash Particles for Use in a Universal Turbine Deposition Model," ASME Paper No. GT2015-43765.
[331] Sacco, C., Bowen, C., Lundgreen, R., Bons, J. P., Ruggiero, E., Allen, J., and Bailey, J., 2017, "Dynamic Similarity in Turbine Deposition Testing and the Role of Pressure," ASME Paper No. GTP-17-1475.
[332] Kim, J., Dunn, M. G., Baran, A. J., Wade, D. P., and Tremba, E. L., 1993, "Deposition of Volcanic Materials in the Hot Sections of Two Gas Turbine Engines," ASME J. Eng. Gas Turbines Power, **115**(3), pp. 641–651.
[333] Schneider, O., Dohmen, H. J., Benra, F.-K., and Brillert, D., 2009, "Investigations of Dust Separation in the Internal Cooling Air System of Gas Turbines," ASME Paper No. GT2003-38293.
[334] Vetere, F., Behrens, H., Holtz, F., Vilardo, G., and Ventura, G., 2010, "Viscosity of Crystal-Bearing Melts and Its Implication for Magma Ascent," J. Mineralogical Petrological Sci., **105**(3), pp. 151–163.
[335] Brunton, S. L., Noack, B. R., and Koumoutsakos, P., 2020, "Machine Learning for Fluid Mechanics," Annu. Rev. Fluid Mech., **52**(1), pp. 477–508.
[336] Ganti, H., and Khare, P., 2020, "Data-Driven Surrogate Modeling of Multiphase Flows Using Machine Learning Techniques," Comput. Fluids, **211**, p. 104626.
[337] Ganti, H., Kamin, M., and Khare, P., 2020, "Design Space Exploration of Turbulent Multiphase Flows Using Machine Learning-Based Surrogate Model," Energies, **13**(17), p. 4565.
[338] Zhu, Y., and Zabaras, N., 2018, "Bayesian Deep Convolutional Encoder–Decoder Networks for Surrogate Modeling and Uncertainty Quantification," J. Comput. Phys., **366**, pp. 415–447.
[339] Wang, X., Yeh, S.-T., Chang, Y.-H., and Yang, V., 2018, "A High-Fidelity Design Methodology Using Les-Based Simulation and Pod-Based Emulation: A Case Study of Swirl Injectors," Chin. J. Aeronautics, **31**(9), pp. 1855–1869.
[340] Lye, K. O., Mishra, S., and Ray, D., 2020, "Deep Learning Observables in Computational Fluid Dynamics," J. Comput. Phys., **410**, p. 109339.
[341] Raissi, M., and Karniadakis, G. E., 2018, "Hidden Physics Models: Machine Learning of Nonlinear Partial Differential Equations," J. Comput. Phys., **357**, pp. 125–141.
[342] Raissi, M., Perdikaris, P., and Karniadakis, G. E., 2019, "Physics-Informed Neural Networks: A Deep Learning Framework for Solving Forward and Inverse Problems Involving Nonlinear Partial Differential Equations," J. Comput. Phys., **378**, pp. 686–707.
[343] Yang, L., Meng, X., and Karniadakis, G. E., 2021, "B-Pinns: Bayesian Physics-Informed Neural Networks for Forward and Inverse Pde Problems With Noisy Data," J. Comput. Phys., **425**, p. 109913.

[344] Zhu, Y., Zabaras, N., Koutsourelakis, P.-S., and Perdikaris, P., 2019, "Physics-Constrained Deep Learning for High-Dimensional Surrogate Modeling and Uncertainty Quantification Without Labeled Data," J. Comput. Phys., **394**, pp. 56–81.
[345] Sen, B. A., and Menon, S., 2010, "Linear Eddy Mixing Based Tabulation and Artificial Neural Networks for Large Eddy Simulations of Turbulent Flames," Combust. Flame, **157**(1), pp. 62–74.
[346] Owoyele, O., Kundu, P., Ameen, M. M., Echekki, T., and Som, S., 2020, "Application of Deep Artificial Neural Networks to Multi-Dimensional Flamelet Libraries and Spray Flames," Int. J. Engine Res., **21**(1), pp. 151–168.
[347] Bhalla, S., Yao, M., Hickey, J.-P., and Crowley, M., 2020, "Compact Representation of a Multi-Dimensional Combustion Manifold Using Deep Neural Networks," *Machine Learning and Knowledge Discovery in Databases*, U. Brefeld, E. Fromont, A. Hotho, A. Knobbe, M. Maathuis, and C. Robardet, eds., Springer International Publishing, Berlin, pp. 602–617.
[348] Pawar, S., San, O., Rasheed, A., and Vedula, P., 2020, "A Priori Analysis on Deep Learning of Subgrid-Scale Parameterizations for Kraichnan Turbulence," Theor. Comput. Fluid Dyn., **34**(4), pp. 429–455.
[349] Wang, Z., Luo, K., Li, D., Tan, J., and Fan, J., 2018, "Investigations of Data-Driven Closure for Subgrid-Scale Stress in Large-Eddy Simulation," Phys. Fluids, **30**(12), p. 125101.
[350] Yao, S., Wang, B., Kronenburg, A., and Stein, O. T., 2020, "Modeling of Sub-Grid Conditional Mixing Statistics in Turbulent Sprays Using Machine Learning Methods," Phys. Fluids, **32**(11), p. 115124.
[351] Xie, C., Yuan, Z., and Wang, J., 2020, "Artificial Neural Network-Based Nonlinear Algebraic Models for Large Eddy Simulation of Turbulence," Phys. Fluids, **32**(11), p. 115101.
[352] Hasslberger, J., Engelmann, L., Kempf, A., and Klein, M., 2021, "Robust Dynamic Adaptation of the Smagorinsky Model Based on a Sub-Grid Activity Sensor," Phys. Fluids, **33**(1), p. 015117.
[353] Nikolaou, Z., Chrysostomou, C., Minamoto, Y., and Vervisch, L., 2021, "Evaluation of a Neural Network-Based Closure for the Unresolved Stresses in Turbulent Premixed v-Flames," Flow, Turbul. Combust., **106**(2), pp. 331–356.
[354] Zhu, L., Zhang, W., Sun, X., Liu, Y., and Yuan, X., 2021, "Turbulence Closure for High Reynolds Number Airfoil Flows by Deep Neural Networks," Aerosp. Sci. Technol., **110**, p. 106452.
[355] Siddani, B., Balachandar, S., Moore, W. C., Yang, Y., and Fang, R., 2020, "Machine Learning for Physics-Informed Generation of Dispersed Multiphase Flow Using Generative Adversarial Networks," arXiv e-Prints, May, p. arXiv:2005.05363.
[356] Tropea, C., and Roisman, I. V., 2000, "Modeling of Spray Impact on Solid Surfaces," Atomization Sprays, **10**(3–5), pp. 387–408.
[357] Santini, M., Cossali, G., and Marengo, M., 2005, "Single-Drop Empirical Models for Spray Impact on Solid Walls: A Review," Atomization Sprays, **15**(6), pp. 699–736.
[358] Khare, P., and Yang, V., 2015, "Newtonian and Non-Newtonian Liquid Droplet Breakup: Child Droplet Statistics," 13th International Conference on Liquid Atomization and Spray Systems, ICLASS 2015, Tainan, Taiwan, Aug. 23–27.
[359] Khare, P., 2014, "Breakup of liquid droplets,". Ph.D. thesis, Georgia Institute of Technology, Atlanta, GA.
[360] Laval, J., Dubrulle, B., and Nazarenko, S., 2001, "Nonlocality and Intermittency in Three Dimensional Turbulence," Phys. Fluids, **13**(7), pp. 1995–868.
[361] Egolk, P. W., and Hutter, K., 2013, "Nonlinear," Nonlocal Fractional Turbulence, Springer Nature, Switzerland, Vol. 86, pp. 835–868.
[362] Germano, M., Piomelli, U., Moin, P., and Cabot, W. H., 1991, "A Dynamic Subgrid-Scale Eddy Viscosity Model," Phys. Fluids, **3**(7), pp. 835–868.
[363] Samiee, M., Akhavan-Safaei, A., and Zayernouri, M., 2020, "A Fractional Subgrid Scale Model for Turbulent Flows: Theoretical Formulation and a-Priori Study," Phys. Fluids, **32**(5), pp. 055102–868.
[364] Mehta, P. P., Pang, G., Fangying, S., and Karniadakis, G. E., 2019, "Discovering a Universal Variable-Order Fractional Model for Turbulent Couette Flow Using Physics-Informed Nueral Network," Fractional Calculus Appl. Anal., **22**(6), pp. 1675–1688.
[365] Mao, Z., Li, Z., and Karniadakis, G. E., 2019, "Nonlocal Flocking Dynamics: Learning the Fractional Order of Pdes From Particle Simulations," Commun. Appl. Math. Computation, **1**(4), pp. 597–619.
[366] Leoni, D., Patricio, C., Zaki, T. A., Karniadakis, G. E., and Meneveau, C., 2020, "Two-Point Stress-Strain Rate Correlation Structure and Non-Local Eddy Viscosity in Turbulent Flows," J. Fluid Mech., **1**, epub.
[367] Chen, W., 2006, "A Speculative Study of 2/3-Order Fractional Laplacian Modeling of Turbulence: Some Thoughts and Conjectures," Chaos, **16**(2), pp. 023126–868.
[368] Song, F., and Karniadakis, G., 2018, "A Universal Fractional Model of Wall-Turbulence," Phys. Fluids, **16**(2), pp. 835–868.
[369] Liang, B., and Mahadevan, S., 2011, "Error and Uncertainty Quantification and Sensitivity Analysis in Mechanics," Int. J. Uncertainty Quantif., **1**(2), pp. 147–161.
[370] Sudret, B., 2008, "Global Sensitivity Analysis Using Polynomial Chaos Expansions," Reliab. Eng. Syst. Saf., **93**(2), pp. 964–979.
[371] Hoffman, F., and Hammonds, J., 1994, "Propagation of Uncertainty in Risk Assessments: The Need to Distinguish Between Uncertainty Due to Lack of Knowledge and Uncertainty Due to Variability," Risk Anal., **14**(5), pp. 707–712.
[372] Jakeman, J., Eldred, M., and Xiu, D., 2010, "Numerical Approach for Quantification of Epistemic Uncertainty," J. Comput. Phys., **229**(12), pp. 4648–4663.
[373] Enderle, B., Rauch, B., Grimm, F., Eckel, G., and Aigner, M., 2020, "Non-Intrusive Uncertainty Quantification in the Simulation of Turbulent Spray Combustion Using Polynomial Chaos Expansion: A Case Study," Combust. Flame, **213**, pp. 26–38.
[374] Le Maître, O., and Knio, O. M., 2010, "Spectral Methods for Uncertainty Quantification: With Applications to Computational Fluid Dynamics," Springer Ser. Sci. Comput., **14**(2), pp. 707–712.
[375] Fishman, G. S., 1996, "Monte Carlo: Concepts, Algorithms, and Applications," Springer-Verlag, New York.
[376] Bravo, L., Murugan, M., Ghoshal, A., Simon, S., Koneru, R., Jain, N., Khare, P., and Flatau, A., 2021, "Uncertainty Quantification in Large Eddy Simulation of CMAS Attack and Deposition in Gas Turbine Engines," AIAA Paper No. 2021–0766.
[377] Turnquist, B., and Owkes, M., 2019, "Multiuq: An Intrusive Uncertainty Quantification Tool for Gas-Liquid Multiphase Flows," J. Comput. Phys., **399**(15), p. 108951.
[378] Roy, C., and Oberkampf, W., 2011, "A Comprehensive Framework for Verification, Validation, and Uncertainty Quantification in Scientific Computing," Comput. Methods Appl. Mech. Eng., **200**(25–28), pp. 2131–2144.
[379] Mishra, A. A., and Iaccarino, G., 2019, "Theoretical Analysis of Tensor Perturbations for Uncertainty Quantification of Reynolds Averaged and Subgrid Scale Closures," Phys. Fluids, **31**(7), p. 075101.
[380] Nieto, A., Agrawal, R., Bravo, L., Hofmeister-Mock, C., Pepi, M., and Ghoshal, A., 2019, "Calcia-Magnesia-Alumina-Silicate (CMAS) Attack Mechanisms and Roadmap Towards Sandphobic Thermal and Environmental Barrier Coatings," Int. Mater. Rev., **399**(15), pp. 1–42.